SELF-PROPULSION AND MIXING OF MICRODROPLETS THROUGH SURFACE TENSION GRADIENT

by

Vi-Vie Ng

UNIVERSITY OF CANTERBURY
Te Whare Wānanga o Waitaha
CHRISTCHURCH NEW ZEALAND
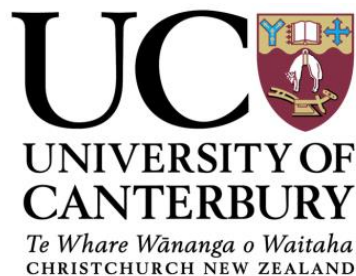
A thesis submitted in partial fulfilment of the requirements for the

Degree of Doctor of Philosophy in Mechanical Engineering at the

University of Canterbury.

2017

Acknowledgments

Abstract

The topic researched for this thesis pertains to the transport and mixing of liquids in the micro-scale. With microfluidic applications in mind, the aim of this research is to further understand and investigate the role of surface tension gradient in the behavior of liquid droplets and slugs. Various platforms that offer differing air-liquid interface exposure, as well as the influence of gravity, have been studied in this research. First, the work pertaining to the uphill climb of a water droplet due to the presence of an adjacent volatile droplet is presented. The experimental results from this novel method of propulsion were confirmed through numerical simulations that accounted for two-phase flows and the transport of diluted species. Second, the mixing of two miscible liquid droplets, of which one is varied by concentration, was investigated. The results provide a clear contrast between the mixing rates resulting from two systems: one with the influence of surface tension gradient, and the other with only molecular diffusion. The numerical simulations carried out confirmed that mixing rate is improved when a surface tension gradient is present. Third, the actuation of droplets in a partially-enclosed setup known as a Hele-Shaw cell was investigated. Sandwiched in between two parallel plates, the actuation of a water droplet was observed upon the introduction of a volatile droplet adjacent to it. The Marangoni and dissipative forces were estimated through both analytical and numerical approaches, where close agreement was found. Lastly, a numerical model was developed to estimate the resistive force for a water slug in a capillary tube. Compared to the first three works investigated, the setup for the capillary tube is different in that it is fully-enclosed. In the numerical approach, the experimental parameters previously published by our group were used and a range of body force values were incorporated to estimate the forces. As a result, numerical results for Marangoni force that agrees well with analytical values were obtained. A second dimensionless model built allowed for the study of mixing time through altering only the Reynolds and Peclet number. The work undertaken for this research has shown the feasibility of liquid self-propulsion in various setups. Additional parametric studies

performed serve as a valuable contribution to this thesis. The numerical models built enable the understanding of the effects of parameters that are otherwise difficult to achieve experimentally. The works presented in this thesis, both experimental and numerical, provide insight into droplet actuation or coalescence through surface tension gradient, which could serve as a basis for future work in the similar context.

Deputy Vice-Chancellor's Office
Postgraduate Office

Co-Authorship Form

This form is to accompany the submission of any thesis that contains research reported in co-authored work that has been published, accepted for publication, or submitted for publication. A copy of this form should be included for each co-authored work that is included in the thesis. Completed forms should be included at the front (after the thesis abstract) of each copy of the thesis submitted for examination and library deposit.

Please indicate the chapter/section/pages of this thesis that are extracted from co-authored work and provide details of the publication or submission from the extract comes:

  1) Chapter 3 is extracted from:
     Ng, V.-V., Sellier, M., Nock, V., 2016. Marangoni-induced actuation of miscible liquid droplets on an incline. Int. J. Multiph. Flow 82, 27–34.

  2) Chapter 4 is extracted from:
     Ng, V.-V., Sellier, M., Nock, V. Marangoni-Improved Mixing in a Two-Droplet System. European J. of Mechanics/B Fluids (*submitted for publication*)

  3) Chapter 5 is extracted from:
     Ng, V.-V., Sellier, M., Nock, V. Sandwiched Droplet Actuated by Marangoni Force in a Hele-Shaw Cell. Acta Mechanica (*submitted for publication*)

Please detail the nature and extent (%) of contribution by the candidate:
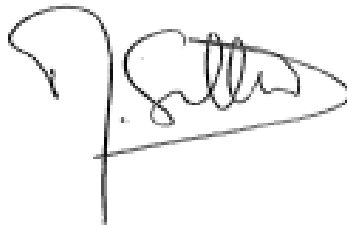
The content of the work is based on ideas jointly formulated by the supervision team and the student. The work has been performed by the student under the supervisory team guidance. Publications have been written by the PhD student and edited by the supervisory team.

Certification by Co-authors:

If there is more than one co-author then a single co-author can sign on behalf of all

The undersigned certifies that:

- The above statement correctly reflects the nature and extent of the PhD candidate's contribution to this co-authored work
- In cases where the candidate was the lead author of the co-authored work he or she wrote the text

Name: *Mathieu Sellier* Signature: Date: *13/04/2017*

The following papers, based on sections of this thesis, have been published, accepted or submitted for publication, or in preparation for submission:

1. Ng, V.-V., Sellier, M., Nock, V., 2016. Marangoni-induced actuation of miscible liquid droplets on an incline. Int. J. Multiph. Flow 82, 27–34.

2. Ng, V.-V., Sellier, M., Nock, V. Marangoni-Improved Mixing in a Two-Droplet System. European J. of Mechanics/B Fluids (*submitted for publication*)

3. Ng, V.-V., Sellier, M., Nock, V. Sandwiched Droplet Actuated by Marangoni Force in a Hele-Shaw Cell. Acta Mechanica (*accepted for publication*)

4. Ng, V.-V., Sellier. Numerical Model for Slug Mixing in a Capillary Tube and Taylor Dispersion Prediction. *(in preparation)*

The work described in this thesis has also been presented at the following conferences:

1. Oral presentation: Engineering Surface Traces for Self-Propulsion of Droplets, *Fluids in New Zealand (FiNZ),* University of Canterbury, Christchurch, New Zealand, January 28-30, 2015

2. Oral presentation: Engineering Surface Traces for Self-Propulsion of Droplets, *AMN-7 Advanced Materials & Nanotechnology,* Nelson, New Zealand, February 8-12, 2015

3. Oral presentation: Coalescence and Diffusion Behavior in a Surfactant-Laden Droplet, *Nanolab Users Meeting,* University of Canterbury, Christchurch, New Zealand, May 20, 2015

4. Oral presentation: Impact of Surface Tension Gradient on Diffusion, *Thesis-in-Three Competition*, Mechanical Engineering Department, University of Canterbury, Christchurch, New Zealand, July 30, 2015

5. Oral presentation: Marangoni-Improved Mixing in a Two-Droplet System, *Nanolab Users Meeting,* University of Canterbury, Christchurch, New Zealand, June 15, 2016

6. Oral presentation: Fluid Actuation in an Enclosed Device, *Thesis-in-Three Competition*, Mechanical Engineering Department, University of Canterbury, Christchurch, New Zealand, August 18, 2016

7. Oral presentation: Sandwiched Droplet Actuated by Marangoni Force in a Hele-Shaw Cell, *Fluids in New Zealand (FiNZ),* University of Canterbury, Christchurch, New Zealand, February 9-10, 2017, **"Best Student Talk in Session"**

8. Oral presentation: Droplet Actuation in a Hele-Shaw Cell, *Nanolab Users Meeting,* University of Canterbury, Christchurch, New Zealand, May 17, 2017

AMN7
Advanced Materials & Nanotechnology
February 8-12, 2015 | Nelson, New Zealand

CERTIFICATE

This letter confirms that

Miss Vivienne Ng
University of Canterbury

attended the conference for Advanced Materials and Nanotechnology (AMN-7)

held in Nelson | New Zealand | 08-12 February 2015

and presented a paper (Oral - Contributed) with the title:

"Engineering Surface Traces for Self-Propulsion of Droplets"

Shane Telfer,
Conference Chair

College of Engineering

Department of Mechanical Engineering
Tel: +64 3 354 2987, Fax: + 64 364 2078

Assoc. Prof Mark Jermy
mark.jermy@canterbury.ac.nz

22nd February 2017

Re: Best Student Talk in Session, Fluids in New Zealand, 9-10 February 2017

To: Vi Ng

Dear Vi,
Thank you for your contribution to the meeting. Your talk, titled "Sandwiched Droplet Actuated by Marangoni Force in a Hele-Shaw Cell" was judged the best student talk in its session.

It was a pleasure to see you at the meeting, and I thank you for your contribution.

Kind regards,

Mark Jermy   Patrick Geoghegan

Organizing committee, FiNZ 2017

Contents

List of Figures

List of Tables

1 Introduction

"Science does not know its debt to imagination." – Ralph Waldo Emerson

1.1 Overview of Research Topic

The research topic, which delves into the self-propulsion and mixing of liquids, can be applied in a wide range of areas, such as surface drying (Matar and Craster, 2001), pulmonary drug delivery (Grotberg, 1994), and oil recovery (Paterson, 1981), to name a few. However, the research work presented in this thesis is most suited to the area of microfluidics: a fluidic system that uses diminutive amounts of fluids (10^{-9} to 10^{-18} liters) within channels that are tens to hundreds of micrometers wide. The emergence of microfluidics is a direct result of the advent in microfabrication technologies, combined with the need for effective fluidic analyses. The applications of microfluidics are wide - one can only imagine what is to come from hereinafter. Currently, researchers have successfully integrated a complex process known as polymerase chain reaction (PCR) into microfluidics, which allows even a very small amount of DNA to be replicated into double-stranded DNA within a short time (Erickson and Li, 2004). Clearly, with these advanced devices, processes that once required constant human intervention can now be performed with minimal supervision. As a result, the speed at which analyses are performed is increased, in addition to greater throughput and cost-effectiveness. Although microfluidics are mostly used in biology, it has also been tapped in areas such as pollution monitoring (Holmes and Gawad, 2010), biohazard detection (Holmes and Gawad, 2010), and the development of smartphones (Castillo-León and Svendsen, 2014), among others.

At the most basic level, a microfluidic device must be able to perform one or all of the following fluidic functions: transporting, mixing and separating. This thesis delves into only the first two components. It is paramount to understand and improve these core fluidic functions before one can proceed to build better miniaturized systems: (a) lab-on-a-chip (LOC), which accomplishes a single or multiple lab processes, or (b) the more ambitious micro total analysis system (μTAS), which integrates the entire sequence of lab processes for chemical analyses (Manz et al., 1990).

According to the World Health Organization, microfluidics as a diagnostic device for developing countries should be ASSURED: affordable, sensitive, specific, user-friendly, rapid and robust, equipment-free and deliverable to end-users (Martinez et al., 2010). Although these attributes have been manifested in paper-based microfluidics, a few drawbacks still remain. One of them includes the fast evaporation of liquid samples from the open structure typical of paper-based microfluidics. While the scope of this research does not include the evaporation rate measurement of liquids per se, the different configurations investigated upon may be useful in analyzing or comparing evaporation rates for future work. The present research can be categorized in terms of three configurations (see Figure 1.1), named according to their air-liquid interface exposure:

   i.   Fully-exposed – as in "Chapter 3: Propulsion on an Incline" and "Chapter 4: Mixing Rate of Two Droplets"

   ii. Partially-enclosed – as in "Chapter 5: Droplet Actuation in a Hele-Shaw Cell"

   iii. Fully-enclosed – as in "Chapter 6: Liquid Slug in a Capillary Tube"
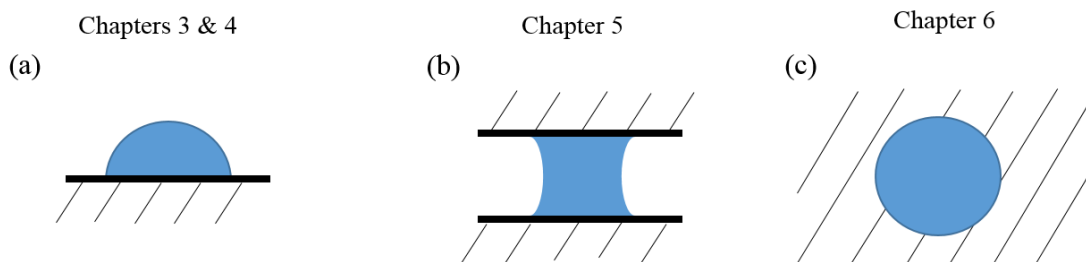
Figure 1.1 An illustration showing the progression of chapters according to droplet configuration: (a) fully-exposed, (b) partially-enclosed, and (c) fully-enclosed

The primary aim of this research is to investigate one of the very core functions of microfluidic devices, i.e. transporting and mixing of liquids, from the context of surface tension gradient. The flow generated as a result of surface tension gradient is also known as "Marangoni flow" (Berthier, 2008), where mass is transferred along an interface from a higher to a lower surface tension region.

1.2   Research Objectives

The three major research objectives of this thesis are:

1) To experimentally study the self-propulsion of micro-droplets from the context of surface tension gradient.

    To date, several methods on droplet propulsion have been reported: electrowetting on dielectrics (EWOD) (Cho et al., 2003; Pollack et al., 2000; Yi and Kim, 2006), opto-electrowetting (OEW) (Chuang et al., 2008; Park et al., 2010), thermocapillary actuation (Brochard, 1989; Choudhury and Tarafdar, 2014; Darhuber et al., 2003a; Ford and Nadim, 1994; Greenspan, 1978), wettability gradient, and surface acoustic waves (SAW) (Ding et al., 2013; Thallhammer and

Wixforth, 2013; Yeo and Friend, 2014). Research pertaining to the self-propulsion of two adjacent droplets due to surface tension gradient has been scarce, but not nonexistent (Karpitschka and Riegler, 2014; Sellier et al., 2011, 2013). The motivation behind this work is to investigate a potential alternative mechanism for droplet propulsion that could address some of the challenges inherent in the other approaches: the need for external power sources, unsustainable wettability gradient and complex microfabrication processes.

2) To investigate the influence of surface tension on the mixing rate of two micro-droplets.

The mixing of two liquids by molecular diffusion alone is a slow process. As such, our work aims to investigate the mixing rate of two liquid droplets through coalescence, with the presence of an air-liquid interface. This work will provide a contrast between mixing due to only molecular diffusion vs. overall mixing involving surface tension gradient or Marangoni flow.

3) To use numerical models to validate experimental and/or analytical results, and to perform parametric studies.

In this thesis, droplets in the micro-scale are to be studied for self-propulsion or mixing. To better understand the role of experimental parameters, some of which are a challenge to achieve experimentally, numerical simulations are to be carried out to closely mimic the experiments and their results. Henceforth, various parameters can be tested to study their influence on the results. The aim is to understand effects such as further miniaturization or the use of other liquids, made possible in a shorter amount of time through numerical simulations.

1.3   Thesis Outline

Chapter 1, *Introduction*, gives an overview of the research topic and highlights the major objectives of the research presented in this thesis.

Chapter 2, *Literature Review*, reviews the fundamental concepts and established work pertaining to the research topics discussed in this thesis.

Chapter 3, *Propulsion on an Incline*, presents the work pertaining to the uphill climb of a droplet due to a surface tension gradient.

Chapter 4, *Mixing Rate of Two Droplets*, presents the comparison of the mixing rate of two liquid droplets, with and without the effects of surface tension.

Chapter 5, *Droplet Actuation in a Hele-Shaw Cell*, reports the actuation of a droplet due to a surface tension gradient, in a semi-enclosed configuration.

Chapter 6, *Liquid Slug in Capillary Tube*, presents the numerical simulations to the experiment of a liquid slug traversing a capillary tube.

Chapter 7, *Conclusion*, highlights the main findings and contributions for each of the research work presented in this thesis.

Chapter 8, *Recommendations for Future Work*, proposes some ideas that could be further expanded based on the work presented in this thesis.

The research works are presented in chapters according to the order: fully-exposed to fully-enclosed configuration. The typical structure for each chapter of the work consists of:

    i.   Introduction

    ii.   Experimental methods

    iii.   Experimental results and discussion

    iv.   Analytical model (if applicable)

    v.   Analytical results and discussion (if applicable)

    vi.   Numerical model

    vii.   Numerical results and discussion

    viii.   Additional numerical results

    ix.   Conclusion

2 Literature Review

"Knowledge has to be improved, challenged, and increased constantly, or it vanishes."
– Peter Drucker

This chapter gives an introduction to the fundamental concepts as well as an overview of established work pertaining to the research topics discussed in this thesis. A more up-close background will be presented under the "Introduction" sub-section of the individual chapters for each topic.

2.1 Surface Tension

A liquid adopts the shape of its container. However, when we delve into smaller scales, such as droplets in the micro- or nano-scale, surface forces play a more prominent role than body forces. If we consider a water droplet resting on a solid surface, the water molecules in the bulk are attracted to all neighboring molecules, causing zero net force (Berthier, 2008). Molecules on the surface, or at the liquid/gas boundary, have half their interactions in the liquid, and the other half in gas. The interaction in gas is less due to the low densities in gas. Therefore, we will only consider interactions at the liquid at the liquid/gas boundary. Figure 2.1 shows a representation of the interactions.
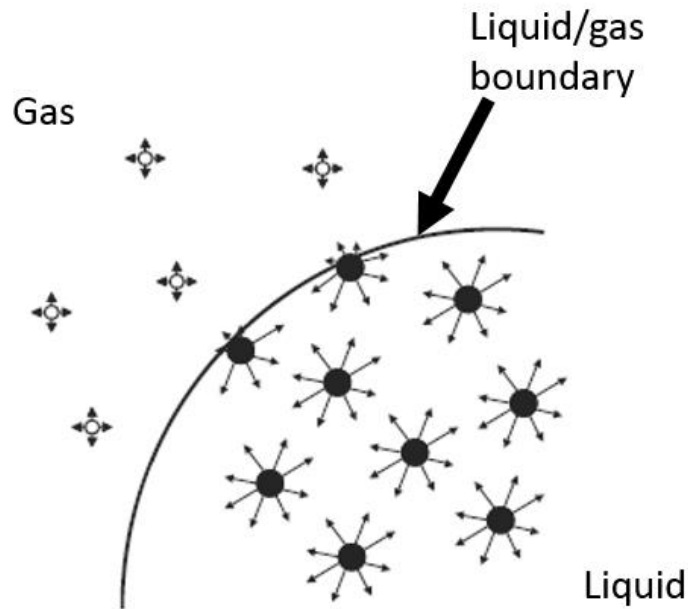
Figure 2.1: Molecular interactions in the liquid/gas phase [adapted from Berthier (2008)]

If U is the total cohesive energy per molecule in the liquid bulk, the total cohesive energy at the liquid/gas boundary can be approximated as $U/2$. Surface tension, measured in units of J/m^2, is a direct measure of the decreased energy. If A is the characteristic surface area of the molecule, we can approximate the surface tension as (Berthier, 2008)

$$\sigma \simeq \frac{U}{2A}.$$ (2.1)

This equation shows that surface tension is prominent when a liquid has high cohesive energy and small molecular dimensions. The shape of the liquid at the liquid/air interface is governed by Young's equation:

$$\sigma_{SG} - \sigma_{SL} - \sigma_{LG} \cos\theta_c = 0, \qquad (2.2)$$

where the contact angle, θ_c is determined by the surface energy at solid/gas interface, σ_{SG}, the surface energy at solid/liquid interface, σ_{SL}, and the surface energy at liquid/gas interface, σ_{LG}. A diagram of the relationship is shown in Figure 2.2.
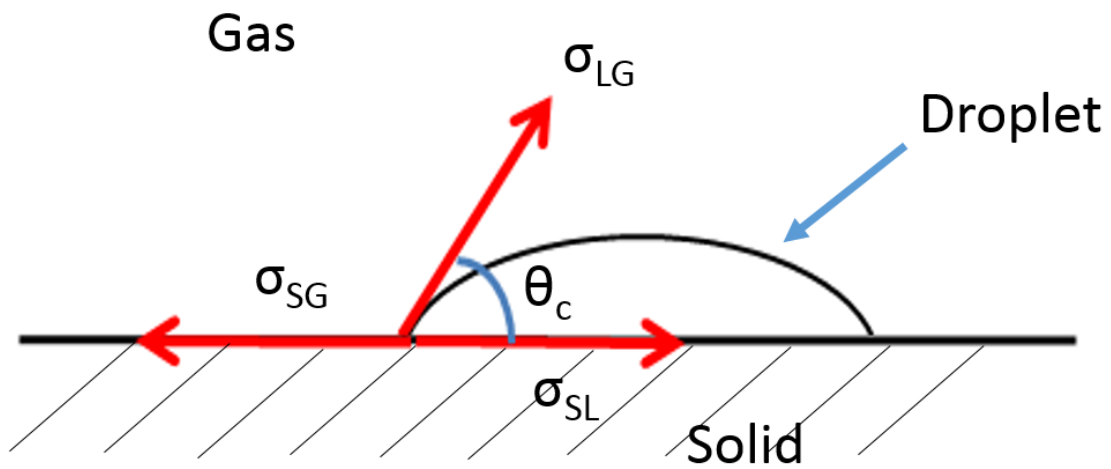
Figure 2.2: Diagram representing a droplet at equilibrium and the force balance at the contact line [adapted from Israelachvili (2011)]

2.2 Marangoni Effect

The Marangoni effect, named after Italian physicist Carlo Marangoni, describes the mass transfer along an interface due to a surface tension gradient. Since a surface with higher surface tension has a higher cohesive energy, a liquid is pulled from the region of lower surface tension to the region of higher surface tension when a surface tension gradient is present.

Surface tension gradients, σ can arise from a difference in temperature, T and concentration, c (Berthier and Silberzan, 2009):

$$\partial \sigma = \frac{\partial \sigma}{\partial T} dT + \frac{\partial \sigma}{\partial c} \partial c. \qquad (2.3)$$

The dependence of surface tension on temperature can be expressed as

$$\sigma = \sigma_o (1 + \alpha T), \qquad (2.4)$$

where $\alpha = -1/T_c$ and T_c is the critical temperature in Kelvin. In an example where a droplet is sitting on a heated substrate, the temperature of the liquid near the substrate is higher than that at the top of the droplet. As such, a temperature gradient occurs, resulting in Marangoni convection, which manifests as a recirculation flow within the droplet (Pradhan and Panigrahi, 2016).

A surface tension gradient due to concentration is often attributed to the role of surfactant. A surfactant reduces the surface tension of a liquid; thus, surfactant molecules occurring on the air-liquid interface of a droplet will move from the region of higher concentration to the region of lower concentration before reaching concentration equilibrium. Figure 2.3 illustrates this phenomenon.
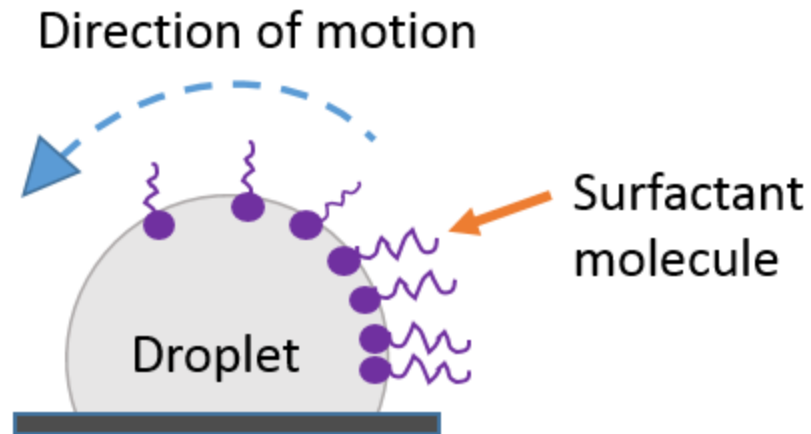
Figure 2.3: Illustration of surfactant molecules moving from region of higher concentration to region of lower concentration [adapted from Berthier (2008)]

2.3   Droplet Propulsion Methods

Microfluidics technology had found its way in applications since the 1970's. The earliest applications include silicon chip based chromatograph developed by Stanford University (Terry et al., 1979) and the ink-jet printer developed by IBM (Petersen, 1979). However, it was not until the 1990's that research into different droplet actuation mechanism had started (Manz et al., 1990). Since then, several droplet propulsion mechanisms have been studied:

(a)   Chemical treatment of substrate to induce wettability gradient (Brochard, 1989; Chaudhury and Whitesides, 1992; Greenspan, 1978),

(b)   Temperature gradient to induce surface tension difference (Darhuber et al., 2003a, 2003b; Ford and Nadim, 1994; Smith, 1995),

(c)   The use of surfactants to induce surface tension gradient (Dos Santos and Ondarçuhu, 1995; Yarin et al., 2002),

(d)   Electrowetting on dielectrics (EWOD) (Moon et al., 2002; Yeo and Chang, 2005),

(e)   Surface acoustics waves (SAW) produced by piezoelectric materials (Ding et al., 2013; Yeo and Friend, 2014),

(f)   Actuation due to vibrations at the substrate (Benilov, 2011; Benilov and Billingham, 2011; Benilov and Cummins, 2013; Brunet et al., 2007, 2009; John and Thiele, 2010; Thiele and John, 2010) , and

(g)   Self-propulsion due to surface tension gradient (Sellier et al., 2011, 2013, 2017).

Though each of these methods presents its own advantages, some of its drawbacks include:

(a)   Need for external power sources,

(b)   Unsustainable wettability gradient, and

(c)   Complex microfabrication processes.

One of the objectives of this research is to extend the study of self-propelling droplets by addressing each of these drawbacks. For some perspective, detailed below are some of the methods of droplet propulsion that have been investigated thus far:

(i)   Electrowetting on dielectrics (EWOD)

The propulsion of droplets through electrowetting on dielectrics (EWOD) relies upon the application of electric potential across pre-patterned electrodes (Cho et al., 2003; Pollack et al., 2000; Yi and Kim, 2006). The solid/liquid surface tension, σ_{SL}, as well as the contact angle of the droplet decreases when an electric potential is applied (Jones, 2002; Kang, 2002; Yoon, 2008). The manipulation of these parameters results in the actuation of droplets across the biased electrodes (Krogmann et al., 2008). The fabrication of an EWOD structure consists of typical cleanroom processes, such as photolithography, dry etching and/or wet etching. These processes are time-consuming

and the metals used to fabricate the electrodes, e.g. gold, chromium, copper, aluminum, can be cost-prohibitive.

Two configurations have been studied so far: (a) parallel plates, and (b) single-plate. The most obvious difference between the two configurations is that a droplet is encapsulated between two parallel substrates with patterned electrodes in a two-plate design, while a droplet rests on an open surface in a single-plate design (Choi et al., 2012). While a two-plate design has its ground and actuating electrodes on the top and bottom plates, respectively, a single-plate design houses both electrodes on the bottom plate. In both cases, the droplet sits directly on a hydrophobic surface on top of a dielectric layer. The dielectric layer acts as an electricity insulator so that hydrolysis from the water droplet can be prevented (Darhuber and Troian, 2005; Yoon, 2008). Figure 2.4 shows a diagram of the two configurations. Although the two-plate design is capable of performing more functions, such as dispensing, moving, splitting, and merging (Cho et al., 2003), the single-plate design is advantageous when a fluorescence signal is required. As reported by (Zeng et al., 2013), the luminescence of a fluorescence droplet on a single-plate design is several times larger than that of a two-plate design. In terms of the disadvantages concerning the EWOD system, (Yi and Kim, 2006) have reported challenges in further incorporating sensing functionalities without adversely affecting actuation.
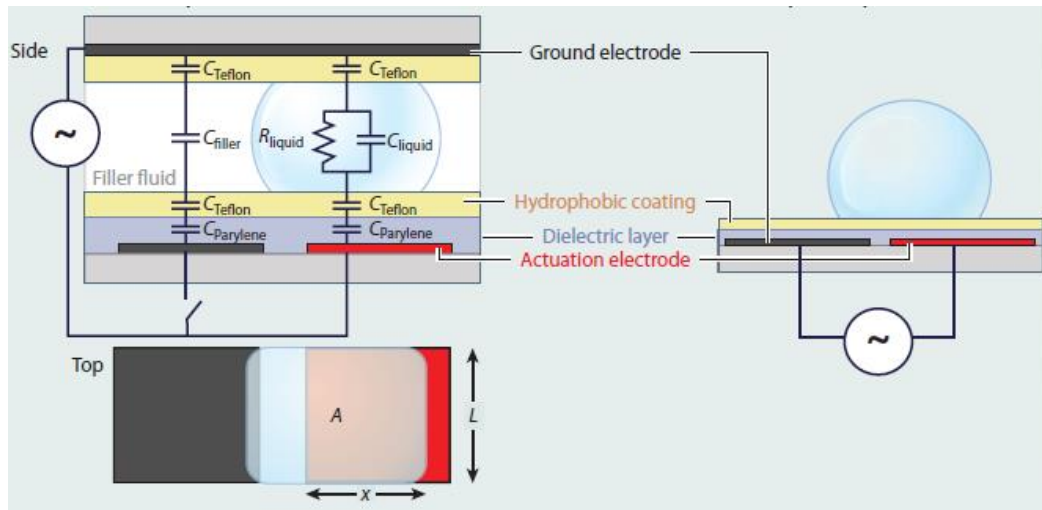
Figure 2.4: A two plate design (left) and a single-plate design (right) of the electrowetting on dielectrics (EWOD) configuration (Choi et al., 2012)

(ii) Optical forces

The method of using optical forces in manipulating droplet movements is also known as opto-electrowetting (OEW). As the name suggests, OEW is derived from the electrowetting method, with the addition of a photoconductive material beneath an array of electrodes (Chuang et al., 2008; Park et al., 2010). This method addresses the limitations that occur from the large number of electrodes used in the EWOD system. With a planar photoconductive layer, a droplet can be actuated in larger areas, as opposed to only on pre-defined areas imposed by electrodes. The reduction in contact angle, which governs droplet actuation, is achieved by altering the voltage drop across the substrate layers. This is attained by irradiating the photoconductive layer, which acts as a variable resistor in the circuit representation of the system (Krogmann et al., 2008). A schematic view of the OEW setup is shown in Figure 2.5. This method is advantageous in that a series of droplets in the picoliter range can be manipulated simultaneously (Chiou et al., 2008; Pei et al., 2010). Also, wiring issues that arise from a typical electrowetting system, which delimits complex microfluidic functions, is

14

mitigated through the OEW method (Chiou et al., 2003). Pei et al. (2010) has also reported the fabrication of a thin, 100-nm dielectric layer using atomic layer deposition (ALD), which resulted in reduced voltage and optical power necessary to drive high speed actuation of droplets.
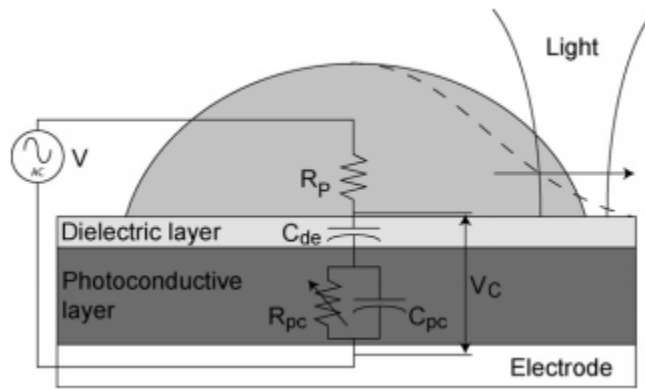
Figure 2.5: Equivalent circuit representation of the opto-electrowetting (OEW) setup (Krogmann et al., 2008)

(iii)   Magnetic forces

Droplet manipulation by magnetic forces, thus far, has been achieved through the use of a droplet containing superparamagnetic particles (Egatz-Gomez et al., 2006), or through synthesized ferrofluidic droplets (Bormashenko et al., 2008; Guo et al., 2006). In both works, the droplets were placed on top of a superhydrophobic surface along with a moving magnet bar underneath. Figure 2.6 shows a representation of the system. A superhydrophobic surface plays a paramount role in reducing the contact area of the liquid to the surface, which reduces the frictional force. This then allows the magnetic forces to be dominant, resulting in easier manipulation of the droplets. A variation of this system has been reported by Park et al. (2006), where amphiphilic silicon microparticles were incorporated in a water droplet surrounded by mineral oil. Based

upon local heating of the droplets, the movement of droplets can be controlled through the amount of microparticles, as well as the magnetization power.
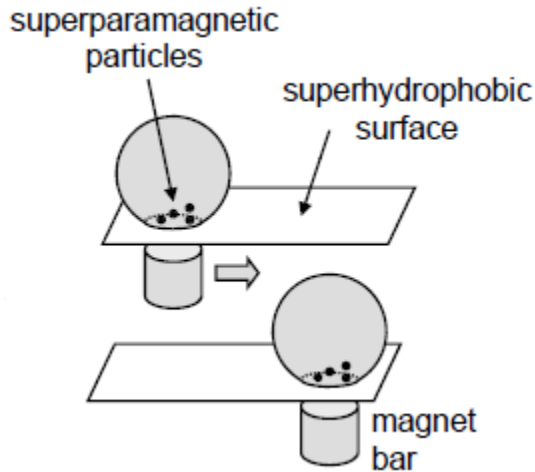
Figure 2.6: Representation of magnetically-driven droplet actuation (Egatz-Gomez et al., 2006)

(iv)   Thermocapillary force/ temperature gradient

Droplet actuation through thermocapillary force is based on the concept of droplet movement from a higher temperature region to a lower temperature region (Brochard, 1989; Chaudhury and Whitesides, 1992; Darhuber et al., 2003a, 2003b; Ford and Nadim, 1994; Gomba and Homsy, 2010; Greenspan, 1978). The solid/liquid surface tension, σ_{SL} in the lower temperature region is higher, resulting in a tangential surface force, which pulls the liquid towards the higher surface tension region.   Such temperature gradient can be achieved by varying the voltage applied in a series of pre-patterned electrodes (Darhuber et al., 2003b, 2010; Mao et al., 2013), as shown in Figure 2.7. Due to the open surface design of this system, the handling of droplets is made convenient. In addition, the low voltage required to drive temperature gradient

allows for the use of this concept in battery-powered applications (Darhuber et al., 2003a, 2003b).
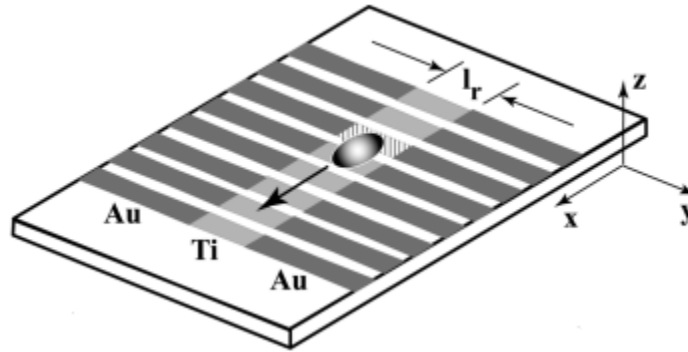
Figure 2.7: Droplet actuation through temperature gradient induced by an array of electrodes (Darhuber et al., 2003b)

(v)   Surface acoustic waves (SAW)

A surface acoustic wave (SAW) is an acoustic oscillation propagating at the surface of a solid (Thallhammer and Wixforth, 2013). Typically, an SAW device for droplet actuation consists of a piezoelectric substrate with interdigitated electrodes patterned on it (Ding et al., 2013; Yeo and Friend, 2014). When a radio-frequency (RF) signal is applied across the electrodes, the piezoelectric substrate underneath contracts and expands due to redistribution of charges (Dung Luong and Trung Nguyen, 2010). This in turn generates surface acoustic waves, which when in contact with a liquid droplet causes acoustic pressure gradient inside the droplet, resulting in an internal acoustic streaming – the basis in the actuation of the droplet (Guttenberg et al., 2005; Tan et al., 2007). A representation of a SAW-based device is presented in Figure 2.8.
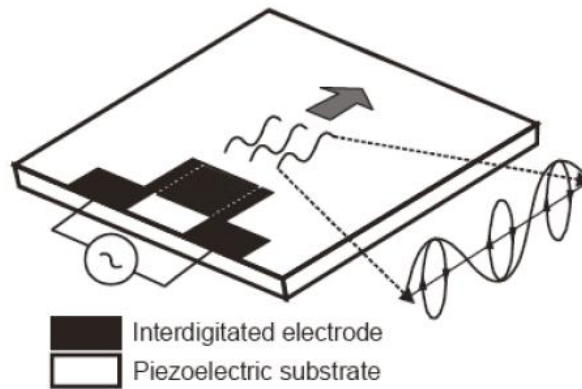
Figure 2.8: Representation of a surface acoustic wave (SAW) device (Dung Luong and Trung Nguyen, 2010)

(vi)   Wettability gradient

Droplet actuation through wettability gradient is based on the concept of droplet migration from a hydrophobic to a hydrophilic surface, depending on the resulting force at the contact line, as well as the contact angle of the liquid (Berthier, 2008; Halverson et al., 2008; Subramanian et al., 2005). A numerical simulation has been performed to confirm this phenomenon (Berthier, 2008). This mechanism has been further extended to demonstrate a droplet moving uphill (Chandesris et al., 2013; ElSherbini and Jacobi, 2004; Extrand and Kumagai, 1995; Vorobyev and Guo, 2010; Zhang and Han, 2007), as well as droplet moving up a step (Berthier, 2008). The gradient in wettability can be achieved through chemical treatment of a substrate. For example, grafting of octadecyltrichlorosilane on one half of a glass renders it hydrophobic, while keeping the other half hydrophilic by not exposing it (Chaudhury and Whitesides, 1992; Daniel and Chaudhury, 2002; Ondarcuhu and Veyssie, 1991).

2.4   Diffusion

Diffusion is commonly understood as the movement of molecules from a region of higher concentration to a region of lower concentration. Typically, it occurs within a single phase, i.e. when the surrounding medium is either air or liquid. In a liquid mixture, concentration has to be measured before diffusion can be analyzed. The most straightforward way is to relate the number of moles of substance, per unit volume. This is known as the molar concentration, which is defined by

$$C_i = \frac{n_i}{V},$$

(2.5)

where C_i is the molar concentration of substance i (mol/m^3), n_i is the number of moles of substance i, and V is the volume of the solution (m^3). Similarly, concentration can be expressed in terms of mass of substance i per volume of the solution, also known as mass concentration (kg/m^3).

If we consider an infinitely long channel pre-filled with water into which a dye is injected, the dye will spontaneously spread out to regions of the water where dye is not present. In other words, the dye diffuses from a region of higher concentration to a region of lower concentration, until a certain time when there is no net flux of dye across any section in the channel. Because of random molecular motions of the dye and water molecules, a uniform mixture of both liquids will be attained after a certain time. This is known as ordinary binary diffusion, which can be described using Fick's first law of diffusion, stated as

$$J = -D\frac{\partial C}{\partial x},$$

where D is the mass diffusion coefficient, with dimension L^2/t, C is the molar concentration of the diffusing dye, and the minus sign denotes movement from higher to lower concentration. This equation shows that the mass of dye moving across a unit area per unit time in the x-direction is proportional to the gradient of the dye concentration in that direction.

2.5 Liquid Diffusion Coefficient

In general, a liquid can diffuse in either air or another liquid. While liquid-liquid diffusion is straightforward, liquid-air diffusion actually refers to the diffusion of liquid 'vapor' in air, and is often characterized for volatile liquids such as alcohols.

2.5.1 Diffusion of Liquid Vapor in Air

To determine the diffusion coefficient of liquid vapors in air, mathematical equations derived from experimental data correlations have been carried out and reported since the 1930's. The experiments conducted were based on the pioneering work of Stefan (1890) where, in his proposed setup, a gas was flowed across the top of an open cylindrical structure containing the liquid under test. The diffusion coefficient of the liquid in gas was then determined based on the amount of liquid lost during the process. The following are a few examples of generalized equations pertaining to the diffusion of liquid vapor in air:

(i)   Arnold (1930) derived a formula that only relies on the intermolecular forces and the boiling temperatures of the substances under test:

$$D_{12} = \frac{0.00837\, T^{3/2} \left(\frac{1}{M_1} + \frac{1}{M_2}\right)^{1/2}}{P\left(V_1^{1/3} + V_2^{1/3}\right)^2 \left(1 + \frac{S_{12}}{T}\right)},$$
(2.7)

where S_{12}, Sutherland's constant, is a function of molal volume of the gases, $V_{1,2}$ and boiling temperature, T. $M_{1,2}$ represent the molecular weights of the gases and P the total pressure.

(ii)   Gilliland (1934) found that the original equation of Maxwell (1868) together with an empirical constant represented the experimental values more closely than the inclusion of Sutherland's constant, as proposed by Arnold (1930). The derived equation reads:

$$D_{12} = \frac{0.0043\, T^{3/2} \left(\frac{1}{M_1} + \frac{1}{M_2}\right)^{1/2}}{P\left(V_1^{1/3} + V_2^{1/3}\right)^2},$$
(2.8)

(iii)   Chapman and Cowling (1939) introduced the collision integral for the potential energy of attraction between two nonpolar gases, $\Omega(1,1)^*$ and the collision diameter, a. The collision integral is a function of energy-dependent transport cross section, in which the latter is related to the angle of deflection in a molecular collision; the collision diameter, σ is the distance separating the centers of the two colliding molecules. The resulting equation reads:

$$D_{12} = \frac{0.001858\, T^{3/2} \left(\frac{1}{M_1} + \frac{1}{M_2}\right)^{1/2}}{P a_{12}^2 \Omega(1,1)^*}, \tag{2.9}$$

where the arguments in $\Omega(1,1)^*$ represent a self-diffusion gas transport.

(iv)   Slattery and Bird (1958) proposed an equation which includes a constant, a, the reduced temperature, T_r, the critical temperature, T_c and critical pressure, P_c. The critical temperature and critical pressure are the maximum values at which the liquid-vapor boundary exists. The reduced temperature, T_r, is the actual temperature normalized by the critical temperature, $T/\ T_c$. The proposed equation reads:

$$D_{12} = \frac{a T_r^b (P_{c1} P_{c2})^{1/3} (T_{c1} T_{c2})^{5/12} \left(\frac{1}{M_1} + \frac{1}{M_2}\right)^{1/2}}{P}. \tag{2.10}$$

In addition, experimental work to determine the diffusion coefficient of liquid in gas has grown steadily following Stefan (1890). Among others, they include the diffusion coefficient measurement of

(i)   Hydrogen peroxide in air (McMurtrie and Keyes, 1948),

(ii)   Nitrobenzene, benzene and water in air (Lee and Wilke, 1954),

(iii)   147 organic compounds and other vapors in air (Lugg, 1968),

(iv)   Water in nonpolar gases (O'Connell et al., 1969), and

(v)   Liquid n-heptane, acetone and methylene chloride in air (Kwon et al., 2003)

2.5.2 Diffusion of Liquid in Liquid

The earliest reported methods of determining the diffusion coefficient of a liquid in another liquid include the diaphragm cell method (Gordon, 1945), as well as the Taylor dispersion method (Taylor, 1953). In contrast, the diaphragm cell method is slower and requires larger concentration gradients (Harris et al., 1993). As such, many have conducted liquid diffusion measurements using the Taylor dispersion method (Baldauf and Knapp, 1983; Lee and Li, 1991; Matthews and Akgerman, 1987; Pratt and Wakeham, 1974; Snijder et al., 1993; Tominaga and Matsumoto, 1990).

In principle, the Taylor dispersion method is based on the joint effects of convection and molecular diffusion (Taylor, 1953). Assuming laminar flow, a liquid is injected into a long horizontal tube (denoted *A* in Figure 2.9) containing another liquid in tube *B*. The diffusion coefficient can then be calculated by the relation (Pratt and Wakeham, 1974)

$$\tau^2 = \frac{R_0^2 t}{24 D_{AB}}, \tag{2.11}$$

where only values of the variance of Gaussian distribution in time, τ^2 and the radius of the tube, R_0 were necessary to obtain the diffusion coefficient, D_{AB}.
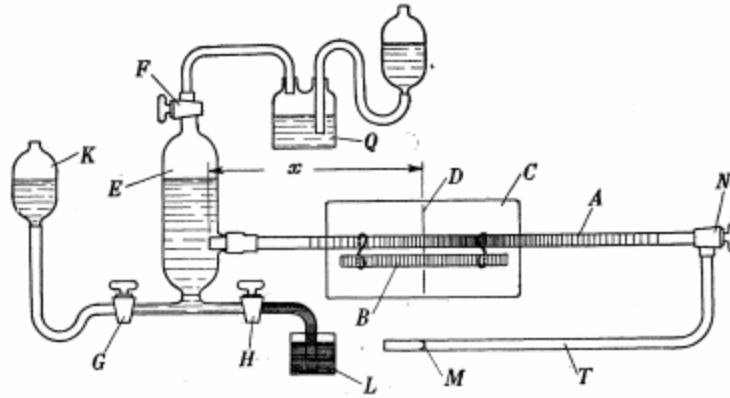
Figure 2.9: Diagram of the setup for measuring liquid diffusion coefficient using the Taylor dispersion method (Taylor, 1953). A is the pipe where liquid is injected into, B is the comparison tube, C is a ground-glass plate, D is the point where the two liquid colors are identical, E is a glass chamber which leads to glass taps F, G, H. K is a funnel filled with distilled water, L and Q are vessels to contain liquids, T is a second pipe in which the meniscus M can be observed, and N is a control valve.

Another method of determining liquid diffusion coefficient is through quasi-elastic scattering (QELS) measurements (Paradies, 1980; Streletzky and Phillies, 1995). In general, a light source is directed into the liquid under test, followed by the analysis of the scattered light imaged at an output. This method allows for the measurement of the hydrodynamic radius of the liquid, which enables the calculation of the diffusion coefficient through the Stokes-Einstein relation

$$D_{exp} = \frac{k_B T}{(6\pi n) R_H},$$
(2.12)

where n is the refractive index, k_B the Boltzmann constant, and R_H the hydrodynamic radius of the liquid.

(Ghi et al., 2002) investigated the use of pulsed-field gradient nuclear magnetic resonance (PFG-NMR) to measure the self-diffusion coefficient of water in a series of copolymers of 2-hydroxyethyl methacrylate (HEMA), and tetrahydrofurfuryl methacrylate (THFMA). In this method, a stimulated echo pulse sequence generated from a spectrometer operating at a proton NMR frequency was used to probe the mobility of the water in the copolymers. If molecules have moved in the direction of the applied magnetic field, a dephasing of the magnetization will occur, resulting in a spin echo attenuation., Ψ, which is the ratio of the amplitude of the spin echo in the presence of a gradient field to the amplitude of the spin echo in the absence of a gradient. The self-diffusion coefficient of a molecule can then be attained through an exponential fit to the Stejskal − Tanner equation:

$$\Psi = \exp(-q^2 D(\Delta - \delta/3), \tag{2.13}$$

where q is the generalized scattering vector, Δ the experimental diffusion time, and δ the width of the gradient pulse. According to Holz et al. (2000), the PFG-NMR method is today a routine method for determining self-diffusion coefficients of liquids. .

2.6 Mixing

The mixing of fluids has been studied since the 1950's by Robert S. Spencer and Ralph M. Wiley at the Dow Chemical Company, and by William D. Mohr and his co-workers at E. I. du Pont de Nemours & Company, Inc. They have found that the stretching and folding of fluids play a significant role in mixing (Ottino, 1989). Fast forward a few decades into the era of microfluidics advancement, and the topic of mixing remains

prevalent. This is evidenced by the considerable number of works addressing mixing enhancement, discussed below.

Though researchers have used the term 'chaotic mixing' in the context of enhanced mixing, it fundamentally refers to the stretching and folding of liquids. Stretching enhances diffusion through the exponential sharpening of concentration gradients, which also levels out non-uniformities. Folding decreases the distance between liquids of different compositions. The two mechanisms work together throughout the entire volume of the liquid to enhance mixing (Grigoriev et al., 2006).

An illustration of the stretching and folding process, also known as the baker's transformation, is shown in Figure 2.10. The term is named after the kneading process in baking, in which a prime example would be the separate but touching layers of dough and fat, successively being stretched and folded in order to create flaky puff pastry, which serves as a basis for making croissants, kouign-amanns, palmiers, cronuts, etc. According to Wiggins and Ottino (2004)) the baker's transformation is the best mixing transformation.
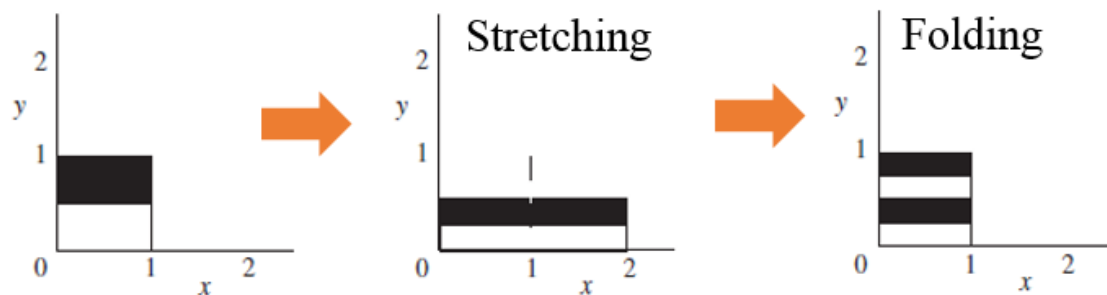
Figure 2.10: An illustration of the stretching and folding process [adapted from Wiggins and Ottino (2004))]

2.6.1　Methods for Enhanced Mixing in Microfluidics

Though microfluidic devices are advantageous due to their small channel scale, which consequently renders increased surface to volume ratio, a challenge still remains: effective mixing. The Reynolds number ($Re = \rho v / \eta$) for such devices is typically low, thus implying laminar flow, where mixing is achieved through molecular diffusion – an inherently slow process (Mengeaud et al., 2002). As such, the microfluidics community has researched into different variations of micromixers to achieve greater mixing.

In general, micromixers can be classified into two categories: active and passive. Active micromixers rely on external forces to generate electric fields, heat and acoustic waves to induce flows and to accelerate diffusion. Typical methods are as those used for droplet propulsion, outlined in Section 2.3. Although good mixing flows have been reported from using active micromixers, one challenge that remains is the choice of driving frequencies and phases, as well as the optimization of these mixers (Stone et al., 2004).

Passive micromixers rely on pressure-driven or electro-osmotic flows. One of the key attributes of passive micromixers is the channel configuration, in which it is designed to either increase the contact area and/or the contact time of the liquid species (Lee et al., 2011). To date, researchers have investigated several interesting designs and techniques to enhance mixing: wedge-shaped inlets (Buchegger et al., 2010), 90º rotation (Tofteberg et al., 2009), zig-zag channels (Mengeaud et al., 2002), 3-D serpentine structures (Neerincx et al., 2011) and T-/Y-mixers (Jain and Nandakumar, 2010), among others. Though mixing efficiencies of ~ 95% have been reported using a passive mixer (Tofteberg et al., 2009), the challenge in most, if not all, passive mixers

27

is the arduous microfabrication process involved. Figure 2.11 presents a few examples of passive micromixers.
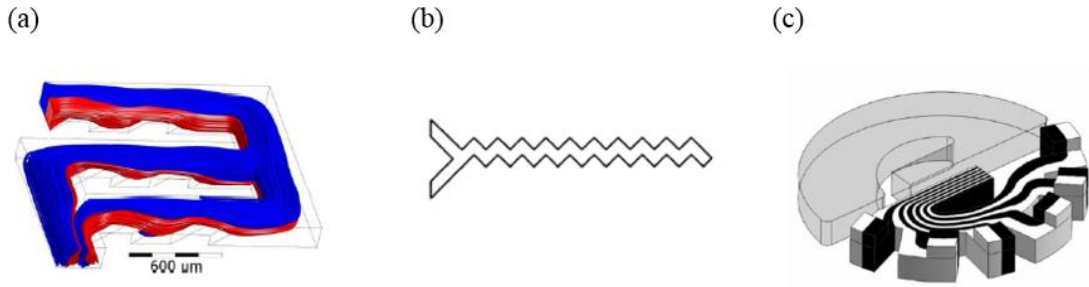
Figure 2.11: Passive micromixers: (a) 90° rotation (Tofteberg et al., 2009), (b) zig-zag channel (Mengeaud et al., 2002) and (c) 3-D serpentine structure (Neerincx et al., 2011)

2.6.2   Quantification of Mixing

To date, terms such as mixing coefficient (Li et al., 1984), degree of mixing (Stroock et al., 2002), uniformity of mixing (Xia et al., 2005), mixing efficiency (Tofteberg et al., 2009), mixing rate (Liu et al., 2010), as well as mixing index (Bansal and Sen, 2016), have been used to define how well two liquids mix. These terms signify the overall effect of molecular diffusion combined with advection or flow towards mixing. In its simplest form, the mixing of two liquids is expressed by (Krasnopolskaya et al., 1999)

$$\langle (D - \langle D \rangle)^2 \rangle,$$

(2.14)

where D represents the statistical density, and $\langle \; \rangle$ represents averaged value dependent on time as well as area. At equilibrium, or the fully-mixed state, this expression becomes 0, which implies that the density must equal the average density. A variation

of this equation was used by Stroock et al. (2002) to quantify the degree of mixing in a passive micromixer. The equation, which measures the standard deviation of intensity distribution, σ, reads

$$\sigma = \langle (I - \langle I \rangle)^2 \rangle^{1/2}, \qquad (2.15)$$

where I takes on the value between 0 and 1 to represent the grayscale values of a pixel, and $\langle \ \rangle$ is the average of all the pixels over the selected region of an image. Similarly, in the study of liquid mixing on a 3-D, X-shaped crossing channel chaotic micromixer, (Xia et al., 2005)) described the uniformity of mixing as

$$\sigma = \sqrt{\frac{1}{n} \sum_{i=1}^{n} (c_i - \bar{c})^2}, \qquad (2.16)$$

where σ represents the standard deviation of the solute concentration, n the number of sampled sections, c the concentration value between 0 to 1, and $\bar{c}$ the average value of concentration over a sampled region. This expression calculates the sum of the difference in concentration between each sampled section and the average concentration of the total sampled region.

From their mixing study of two coalescing droplets on a wettability gradient, Lai et al. (2010) used the micro-laser induced fluorescence technicque (micro-LIF) to visualize mixing and expressed the quality of mixing, or the mixing index, M_i within a liquid volume as

29

$$M_i = \frac{\int |C - C_\infty| dV}{\int |C_0 - C_\infty| dV}, \tag{2.17}$$

with C the time-dependent concentration of the fluorescently-labeled species, C_∞ the concentration of a fully-mixed droplet and C_0 the concentration of a fully un-mixed droplet. A mixing index of 0 and 1 represent a fully-unmixed and a fully-mixed fluid, respectively. The term mixing index was also used by Bansal and Sen (2016) to describe the mixing of two droplets on an EWOD device. Based on the frames, which comprise of individual time-lapse images extracted from the videos of their experiment, their equation for the mixing index at the kth frame reads

$$M.I.(k) = \frac{\emptyset_f - \emptyset_k}{\emptyset_f - \emptyset_i}, \tag{2.18}$$

where $\emptyset$ can represent either the mean or the standard deviation of hue distribution from image processing, f the final frame and i the initial frame. In their work, the frame in which droplets initially merge was chosen as the initial frame.

In a study of mixing in a 2-D annular wedge cavity, Krasnopolskaya et al. (1999) evaluated the quality of mixing using coarse-grain values of square density, intensity of segregation or entropy. Based on dividing the total cavity area into equally-sized boxes, where the presence of dye is represented by various gray scale intensities (between black and white), the following expression was derived

$$\langle D \rangle = \frac{1}{N_\delta} \sum_{n=1}^{N_\delta} D_n = \frac{S_b}{S}, \tag{2.19}$$

where $\langle D \rangle$ is the average mean density, N_δ the number of square boxes of side size δ, S_b the area of colored boxes and S the total cavity area.

In addition to the works mentioned in this section, a number of other works have also reported the mixing rate of two liquids and quantified them in similar ways. Another commonality among those works is the reliance on intensity analysis to examine mixing rate (Carroll and Hidrovo, 2013; Hessel et al., 2005; Muradoglu and Stone, 2005).

2.7 Hele-Shaw Cell

The Hele-Shaw cell was invented by Henry Selby Hele-Shaw in 1898. It is comprised of two parallel plates placed sufficiently close together (Figure 2.12) such that the flow from the liquid contained in between the plates is laminar.
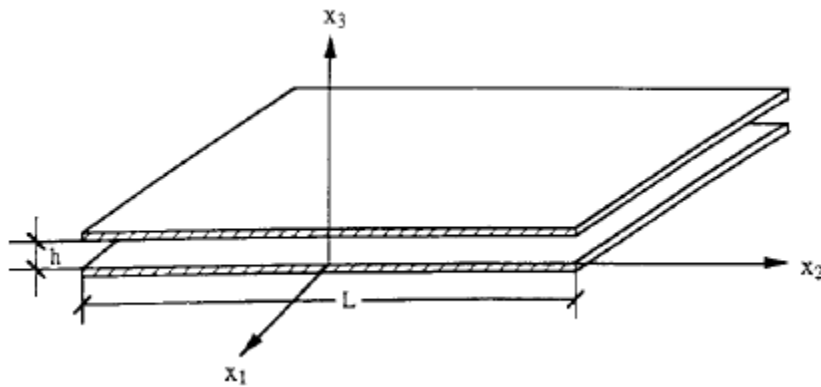
Figure 2.12: Illustration of a Hele-Shaw cell of length L, and height h, in rectangular coordinates (Usami et al., 1993)

The flow is assumed to be parabolic, with velocity the highest at the center (Figure 2.13).
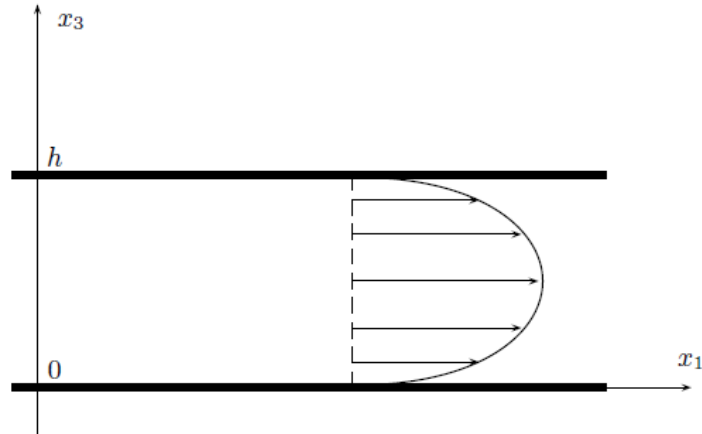
Figure 2.13: Cross-section of a Hele-Shaw flow in a Hele-Shaw cell of height h (Gustafsson and Vasil'ev, 2006)

Typically, the distance between the plates is much smaller compared to the characteristic length of the plates, i.e. $h \ll L$. Assuming that the Reynolds number of the flow is small, inertial effects can be neglected. Since flow is two-dimensional and parallel to the plates, the velocity normal to the flow is zero, i.e. $v_3 = 0$ (with reference to Figure 2.12). The velocity of the flow can therefore be expressed as

$$\vec{v} = \boldsymbol{e_1}v_1 + \boldsymbol{e_2}v_2, \tag{2.20}$$

where $\boldsymbol{e_1}$ and $\boldsymbol{e_2}$ represent unit vectors in the x_1 and x_2 directions, respectively. The solutions (Usami et al., 1993) to the Navier-Stokes equations consist of

$$v_1 = \frac{6}{h^2} x_3 (h - x_3) \bar{v}_1,$$

(2.21)

$$v_2 = \frac{6}{h^2} x_3 (h - x_3) \bar{v}_2,$$

(2.22)

$$v_2 = \frac{6}{h^2} x_3 (h - x_3) \bar{v}_2,$$

(2.23)

where $\bar{v}_1$ and $\bar{v}_2$ are the time-averaged mean velocities at any x_1 and x_2. Averaging across the vertical direction, the Navier-Stokes equations reduce to an expression that relates pressure to velocity:

$$\nabla p = -\frac{12\mu}{h^2} \vec{v},$$

(2.24)

where μ is the viscosity of the liquid.

2.8 Hele-Shaw Cell Applications

The Hele-Shaw cell has been used in a wide range of areas to study two-dimensional flows; from oil recovery (Paterson, 1981) to geological storage (Faisal et al., 2015) to biological modeling (Wei et al., 2003). The classical application of a Hele-Shaw cell involves the penetration of a less viscous liquid into a more viscous liquid that is pre-filled in the cell, resulting in the formation of fingers. Lewis (1950) had experimentally verified this phenomenon and theorized that when two fluids of different densities are accelerated in a direction normal to their interface, the surface between the two fluids becomes unstable, resulting in fingers. McLean and Saffman (1981) had mathematically shown that the width of the fingers increases with surface tension. The

prediction of the fingering phenomenon is useful especially in effective oil recovery. The study of instabilities in a Hele-Shaw cell has continued considerably, as evident from works that describe the problem using numerical and theoretical analyses (Choudhury and Tarafdar, 2014; Savina and Nepomnyashchy, 2015). The forces acting on a stationary droplet in a Hele-Shaw cell, resulting from surface tension gradient and an external flow, have been studied numerically by (Gallaire et al., 2014).

Usami et al. (1993) introduced a tapered channel design within two parallel plates to create a linear variation of fluid shear stress, to study the effects of flow on endothelial cells. In our circulatory system, the endothelial cell surface is subjected to various shearing stresses due to blood flow. Therefore, to model a system where various shear stresses can occur on different points, the tapered channel design was used. On a classical Hele-Shaw model, this could have been realized using several setups comprising of different gaps and flow rates, but it would not closely model the functional human circulatory system. Figure 2.14 (a) shows the tapered channel design, where the flow entrance is from the side of minimum width. The shear stress acting on the lower plate at a point (x_1, x_2) was calculated using the formula:

$$\tau_w = \frac{12\mu|A|}{h}r,$$

(2.25)

where A is a constant, and $r = \sqrt{x_1^2 + x_2^2}$. It was shown that shear stress was the highest at the flow entrance and decreases linearly from thereafter (see Figure 2.14 (b)).

(a)

x_2 (cm)

Flow entrance

(b)

τ_w (dyn/cm^2)
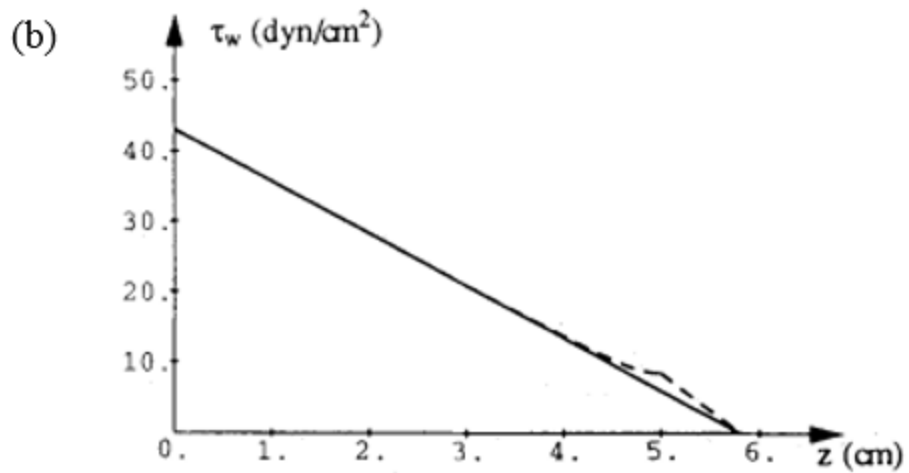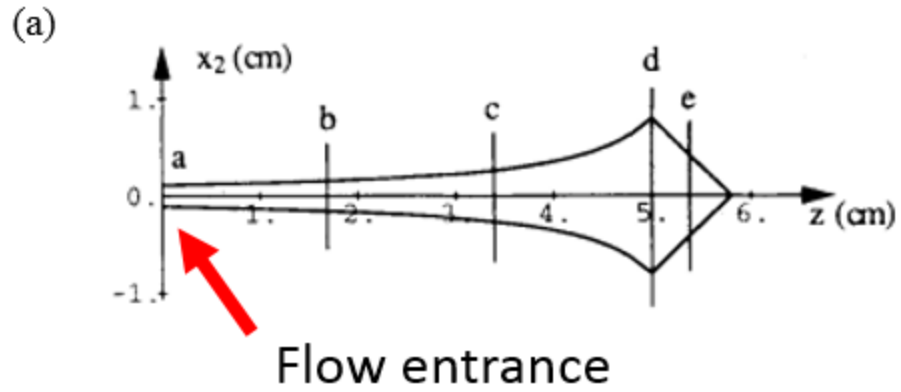
Figure 2.14 (a) An illustration of the tapered channel design, and (b) the shear stress along the center line of the channel (z-axis), shown by the solid line, and the shear stress along the wall of the channel, shown by the dashed line (adapted from Usami et al., 1993)

To model and test the adherence of platelets to fibrinogen, an important part in wound healing, the Hele-Shaw cell was coated with fibrinogen and placed into a chamber on an inverted microscope. A suspension of platelets was then infused into the chamber, followed by the introduction of a gas flow from the flow entrance to generate a range

of shear stress along the channel. The design has been shown to successfully trap more platelets at the downstream, wider end of the channel.

Plouffe et al. (2007) has then applied this design to show the adhesion of muscle cells, endothelial cells and fibroblasts. These cell types are jointly present in different types of tissues; therefore, the ability to capture and separate these cells are advantageous in the field of tissue engineering. Zeng and Weinbaum (1994) modeled the intercellular channel between vascular endothelial cells by using the Hele-Shaw setup, with discontinuities along the channel to account for tissues. Wei et al. (2003) studied the transport in and across capillary blood vessels using theoretical analysis of the Hele-Shaw setup. However, instead of a planar channel, they modeled the phenomenon using wavy-walled channel to closely mimic the configuration of cells, their nuclei and intercellular junctions. Zouache et al. (2015) have mathematically analyzed the blood flow within the thin layer adjacent to the outer retina by using the Hele-Shaw flow approximation, although the geometry studied was an isosceles triangle.

In microfluidics, Shen et al. (2014) studied the behavior of droplets confined in a Hele-Shaw cell, as well as the influence of the side walls. Their work suggests the possibility of self-assembly, mixing or transport of droplets under controlled conditions. Amselem et al. (2015) further showed that a fluorinated oil droplet suspended in a glycerol-water mixture within a Hele-Shaw cell can be broken into two droplets when the surrounding liquid is flowed beyond a critical velocity, from a fixed side opening of the cell.

In studying CO_2 geological storage, Faisal et al. (2015) used a water-saturated Hele-Shaw cell to determine the transfer of CO_2 through density-driven convection, as well as the fingers that resulted from the process. The Hele-Shaw setup can potentially be

used as a means to drain liquid from a narrow gap until a desired thickness to produce thin film photovoltaic cells (Dhanabalan et al., 2001; Sullivan et al., 2014).

3 Propulsion on an Incline

"After climbing a great hill, one only finds that there are many more hills to climb." -
Nelson Mandela

This chapter presents the investigation of droplet self-propulsion up an incline, confined on a polydimethylsiloxane (PDMS) trace rendered hydrophilic through combined oxygen plasma and polyvinylpyrrolidone (PVP) treatment. The effects of substrate angle on the distance traveled, along with the threshold value for when gravitational force overcomes Marangoni force, are discussed. A numerical simulation has been developed, where the governing equations are solved using (*COMSOL Multiphysics*, 2015). The numerical simulation, made dimensionless, allows for the prediction of distance traveled and droplet morphology when key parameters in a physical experiment are varied. The work presented in this chapter has been successfully published in the *International Journal of Multiphase Flow* (Ng et al., 2016).

3.1 Introduction

Self-propulsion of droplets may facilitate automated synthesis and analysis of small liquid samples in lab-on-a-chip applications. Various techniques of droplet self-propulsion have been studied: (a) chemical treatment of substrates to induce wettability gradients (Greenspan, 1978; Brochard, 1989; Chaudhury and Whitesides, 1992), (b) temperature gradients to induce surface tension differences (Ford and Nadim, 1994; Smith, 1995; Darhuber et al., 2003a), (c) the use of surfactants to induce surface tension gradients (Dos Santos and Ondarçuhu, 1995; Yarin et al., 2002), (d) electrowetting on

dielectrics (EWOD) (Moon et al., 2002; Yeo and Chang, 2005) and (e) surface acoustics waves (SAW) produced by piezoelectric (Ding et al., 2013; Yeo and Friend, 2014). Though each of these methods presents its own advantages, some of its drawbacks include: (a) the need for external power sources, (b) unsustainable wettability gradients, and (c) complex microfabrication processes. Building upon previous work by our group (Sellier et al., 2011, 2013), we further explore the feasibility of droplet translation up an incline surface through coalescence-induced self-propulsion.

To date, several works pertaining to the motion of micro-sized droplets moving uphill have been published. By exposing silicon with the vapor of decyltrichlorosilane to create a surface energy gradient, Chaudhury and Whitesides (1992) showed a droplet moving uphill on a 15° inclined surface. Bain et al. (1994) and Chandesris et al. (2013) fabricated grooves with a wettability gradient to induce motion, on a glass and a silicon surface, respectively. Vorobyev and Guo (2010) demonstrated a droplet moving vertically on a superwicking glass by means of grooves created using laser beams. Using microwave-plasma enhanced chemical vapor deposition (MPECVD) to create a superhydrophobic thin film on glass, Wu et al. (2006) showed a water droplet moving up a 17° incline after the substrate was charged with static electricity. Based on high chemical gradient, Yao et al. (2012) showed that a hydrofluoric acid droplet propels itself by etching the silicon substrate underneath on inclines of 15°, 45°, and 90°. In addition to wettability gradients, Zhang and Han (2007) included shape-gradients in their cleaved mica substrate and showed uphill movement up to an angle of 15°.

The work presented in this thesis is different in that complex and time-consuming microfabrication processes such as photolithography, etching, etc. are not involved. Also, most reported works on droplet moving uphill were done on rigid surfaces such as silicon wafers (Chaudhury and Whitesides, 1992; Wu et al., 2006; Yao et al., 2012),

glass (Vorobyev and Guo, 2010), and mica (Zhang and Han, 2007). Our choice of using a flexible elastomer that is polydimethylsiloxane (PDMS) offers several advantages: Since it is liquid before being heat-cured, it can be poured onto designed molds to create substrates with custom surface features down to the nanometer range, if required. The thickness of PDMS substrates can be easily controlled by adjusting the volume of pre-polymer cast or by spin-coating the pre-polymer onto other materials. PDMS is transparent at optical wavelengths (240 nm – 1100 nm), which eases the inspection of the contents in droplets on the surface, both visually and under a microscope. It has low auto-fluorescence (Piruska et al., 2005), which facilitates biochemical assays involving fluorescence signals. Furthermore, its nontoxicity and biocompatibility make it suitable for lab-on-a-chip applications pertaining to biological entities such as cells and microorganisms (Kim et al., 2011). Also, it is inexpensive compared to silicon. Our choice of material and mechanism in guiding a droplet along a hydrophilic trace is well-suited for various digital microfluidics applications (Nock et al., 2013).

In comparison to previous works, which rely on surface energy gradients engineered either onto a substrate, or between a droplet and the underlying substrate, our work proposes the introduction of a surface energy gradient through liquid-vapor phase interaction, as well as from the direct mixing of two miscible liquids on a substrate.

3.2 Experimental Methods

This section describes the fabrication of the PDMS substrates as well as the experimental methods used to analyze the movement of droplets on the substrates inclined at various angles.

The PDMS substrates were prepared by casting (Xia et al., 2005). In brief, PDMS pre-polymer was first prepared by mixing the base and curing agents (Sylgard 184, Dow Corning) at 10:1 w/w ratio, followed by degassing of the mixture in a desiccator until no air bubbles were visible. The liquid pre-polymer was then poured into single-well polystyrene (PS) cell culture trays (Thermo Scientific) to yield flat PDMS substrates of approximately 5 mm thickness. PS culture trays were used since PDMS does not adhere to PS due to a different chemistry, which in turn facilitates peel-off. Degassing was performed to eliminate any bubbles present in the liquid PDMS. Subsequent curing was carried out on a hotplate for 6 h at 80 °C. The PDMS substrates were left to cool at room temperature for 24 h before being carefully peeled out of the PS tray.

To ensure surface planarity, only the side that was in contact with the PS tray was used for the experiments. This side takes on the surface roughness of the PS tray, which has an RMS value of ~ 6 nm (Zeiger et al., 2013). Because of the observed symmetry upon droplet deposition on this surface, we may assume that our substrate did not significantly impact our experiments. Prior to use, the substrates were stored sandwiched between clean polyethylene (PE) sheets.

Hydrophilic traces measuring 1 mm-wide were created on the cured PDMS substrates using cut-out PE strips. These strips were used to protect the native PDMS surface underneath from subsequent plasma exposure. To ensure good adherence, the back of a pair of tweezers was used in a gliding motion to manually attach the PE strips onto the PDMS substrate. The entire assembly was then loaded into a barrel plasma etcher (Emitech K1050X, Quorum) for O_2 plasma exposure lasting 3 minutes at 30 W RF power. Immediately after plasma exposure the PDMS was then treated with polyvinylpyrrolidone (PVP) (Sigma-Aldrich) according to the procedures reported by Hemmilä et al. (2012). The treated substrates were kept in a controlled environment where also prior preparations and subsequent experiments were performed: 21 °C +/-

1 $^{\circ}$C and 50% humidity. Individual rectangular PDMS pieces measuring 2×4 cm, with a 1 mm-wide, now with a hydrophilic trace in the middle, were cut from the treated PDMS substrates. These rectangular pieces were set on a piece of glass attached in perpendicular to an adjustable triangle compass. Figure 3.1 shows the experimental setup. Propulsion experiments were then carried out at angles 0° to 24°, with increments of 4°.

For each experiment a distilled water droplet of volume 1 µl was first deposited onto the trace using an electronic multi-channel micropipette (0.2-10 µl Picus, Biohit). This was followed by the deposition of a 1 µl EtOH droplet adjacent to the water droplet. The experiment was simultaneously recorded using a high-speed digital camera (MQ013MG-E2, Ximea) connected to a PC via USB-3 interface. Recorded images were analyzed using the Image Processing toolbox in Matlab (R2013b, Mathworks).
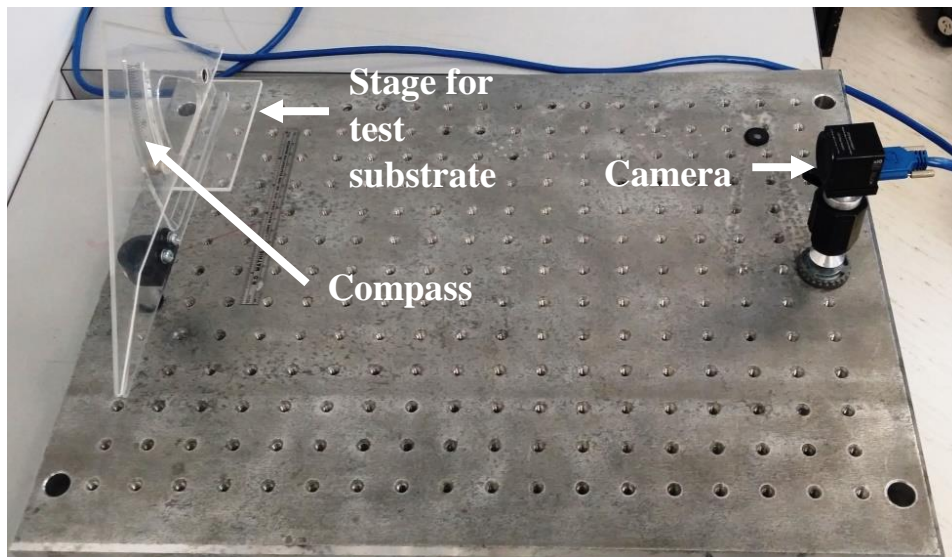
Figure 3.1: Setup of the experiment showing the triangle compass with attached substrate stage and digital camera used for observation of droplet translation. Lens are not attached

The side-view depicting droplet translation up an incline is shown in Figure 3.2. The overlaid images analyzed using Image J 1.49 (Rasband, 1997) show the green droplet as the starting position, and the red droplet as the final position. To further aid observation, the insets show close-ups of the droplets. Subsequent measurements of propulsion distance from the selected images were carried out using Image J.
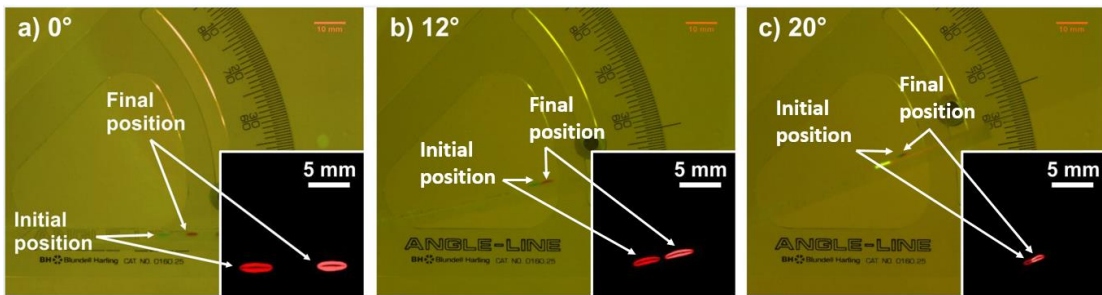
Figure 3.2: Overlaid still photographs of droplet translation at (a) 0°, (b) 12°, and (c) 20° showing both initial and final position of the water droplets. Insets show false-color close-ups used for translation analysis

3.3   Experimental Results and Discussion

This section discusses the results from finding the optimized conditions for the experiment, as well as the experimental results of the self-propelling droplet, which will be compared against the numerical results.

Because of the short-lived hydrophilicity of a plasma-enhanced trace, which we have observed experimentally and was also reported by Hemmilä et al. (2012), we investigated the use of PVP-treatment, as mentioned in the previous section. PDMS comprises of $Si-CH_3$ groups, which turn into $Si-OH$ (silanol) groups when it is exposed to oxygen plasma. Following that, with PVP-treatment, the hydroxyl (OH) groups of

the surface-activated PDMS become hydrogen-bonded to PVP. Using a goniometer (KSV Instruments), we found that the PVP-treated surface exhibited a more sustained hydrophilicity. As shown in Figure 3.3, the contact angle of a sessile water droplet measured on a PVP-treated surface remained at 27° for the first 10 days, while the contact angle measured on the plasma-enhanced surface started higher at 70° and increased by 20° on day-10. Hemmilä et al. (2012) reported lower contact angle values, ranging from $16^o - 22^o$ during the first seven days. Nevertheless, compared to using only plasma-treatment, we achieved very much lower contact angle values when PVP-treatment was incorporated. The plasma-enhanced surface continues to show increased contact angle as days progressed, with the highest recorded at 114° on day-14, while the contact angle for the PVP-treated surface increased to only 36°. In comparison, the highest contact angle over the course of six months reported by Hemmila et al. (2012) was ~ 22°, possibly due to better storage.
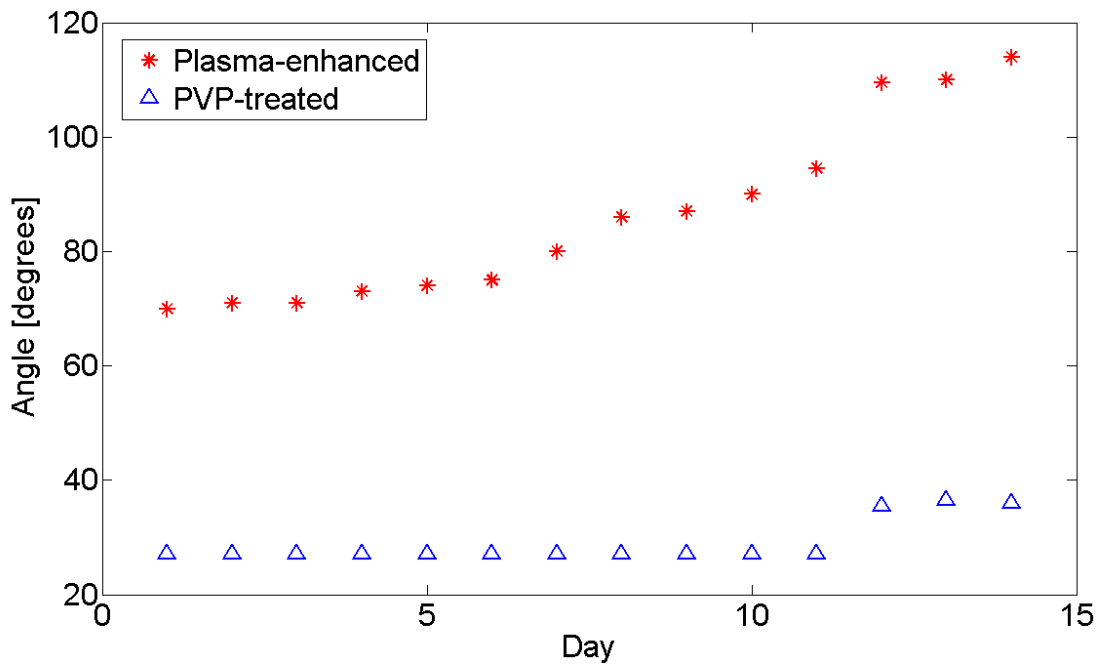
Figure 3.3: Contact angle measurements of sessile water droplets on plasma-enhanced and PVP-treated PDMS surfaces

Besides process optimization of the hydrophilic trace, the effect of droplet volume on propulsion distance was studied. On a 1 mm-wide PVP-treated trace, propulsion of equal volumes of water and EtOH ranging from 0.2 – 2.1 μl was tested on a horizontal plane. Our results showed that propulsion distance increases as volume increases from 0.2 μl to 1.0 μl, as shown in Figure 3.4. The plateaus could be due to slight experimental or measurement errors. Beyond 1.0 μl, the propulsion distance decreased erratically. We believe that this could be attributed to the overflow of the larger droplet outside the bounds of the hydrophilic trace, as observed experimentally. Seemann et al. (2005) reported a similar phenomenon, where they observed an overspill of the droplet outside the contact lines as the droplet volume is increased. Because of the increased footprint, the surface area becomes larger, hence an increased viscous resistance.
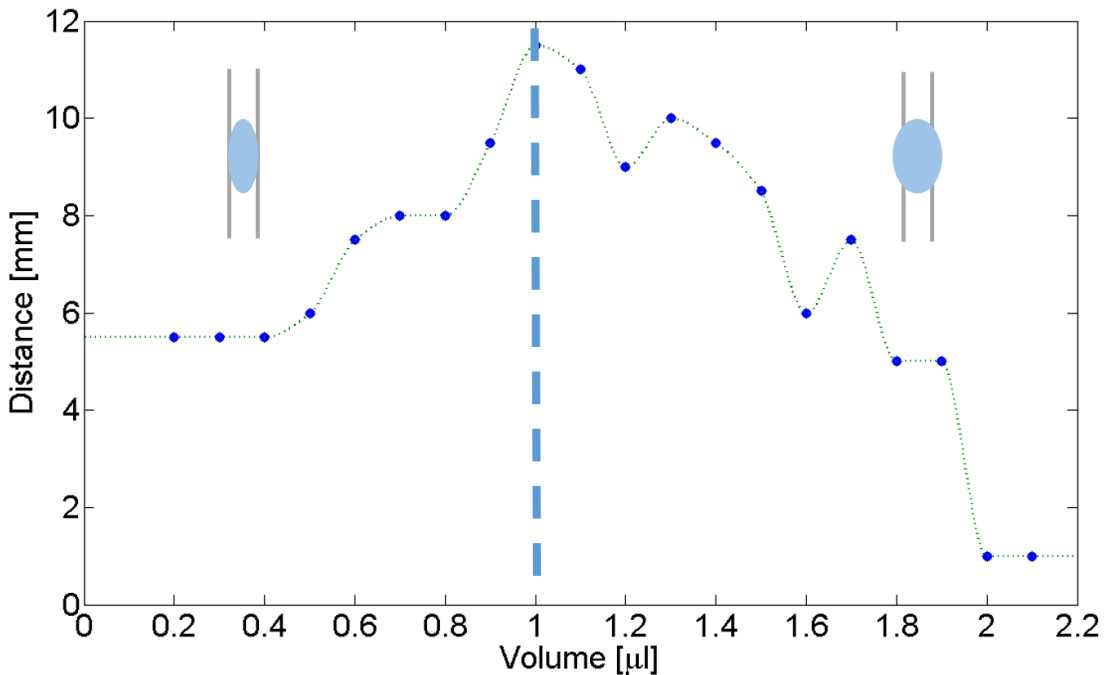
Figure 3.4: Plot of propulsion distance using various droplet volumes on a 1 mm-wide trace, on a horizontal plane. Dashed line represents the maximum volume for the containment of droplet within the trace

Based on the optimized parameters for the fabrication of the hydrophilic trace as well as the optimum droplet volume for maximum propulsion, we proceeded with the experiment of propulsion on an incline. We found that the source for propulsion was the EtOH vapor dissolving in the water droplet. This is based on our observation that the water droplet self-propels when the EtOH droplet held on the tip of the pipette was brought close to it, i.e. without needing the EtOH droplet to be deposited onto the substrate. This method can be used to continually guide a water droplet. However, for our experiments, we hypothesize that a small amount of EtOH mixes with the water droplet. Our results showed the highest translation of ~ 10 mm at both 0° and 4°. Subsequent translations at 4° increments showed a linear downward trend, with zero translation at 24°. The experiment for each angle was repeated four times. By taking the average of the traveled distances on the same substrate, the standard deviation for every angle tested was computed. Following that, the error bar for each measurement was obtained, as shown in Figure 3.5.
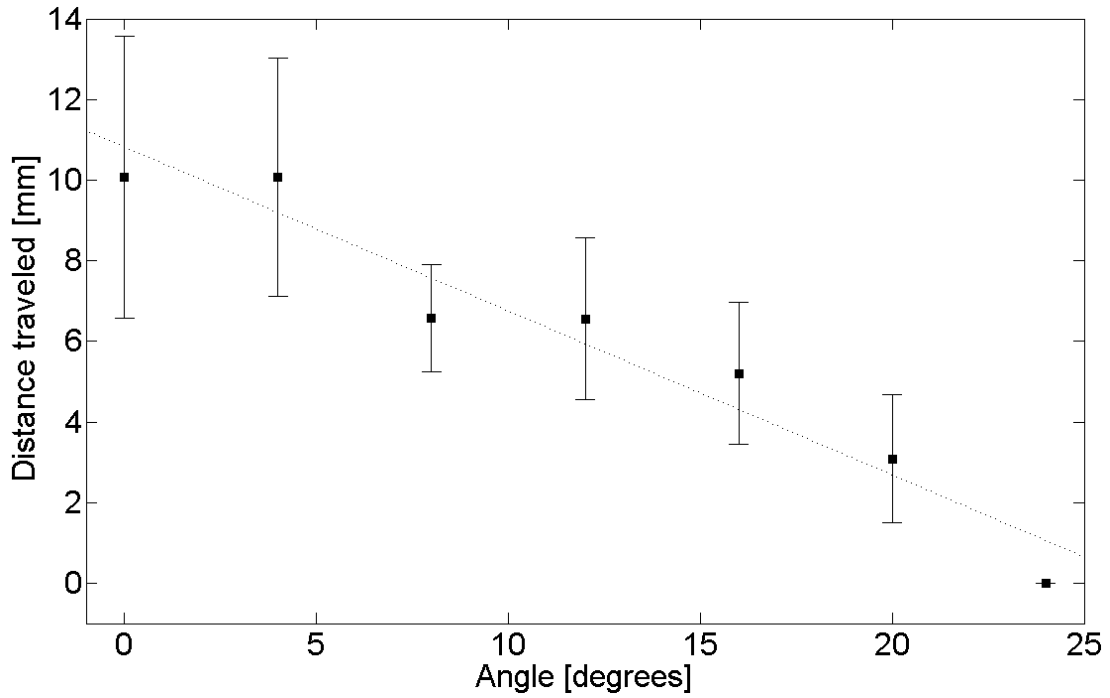
Figure 3.5: Plot of distance a water droplet translates on the PDMS substrate for angles starting from 0° to 24°, with increments of 4°

3.4 Numerical Model

This section discusses the geometry of the droplet, as well as the governing equations used to derive a set of partial differential equations solved using the commercial Finite Element package COMSOL 5.2.

Our simulation begins with defining a parabolic droplet with height h_o, and characteristic radius R_o, resting on an inclined plane at an angle α, as shown in Figure 3.6(a). The direction of flow is constrained to the x-direction only, on a hydrophilic trace of width w, as illustrated in Figure 3.6(b). The system studied consists of a droplet

47

of water, which is actuated by a droplet of ethanol (EtOH). A video of the resulting phenomenon can be viewed at: https://youtu.be/zsznQP6GVwA
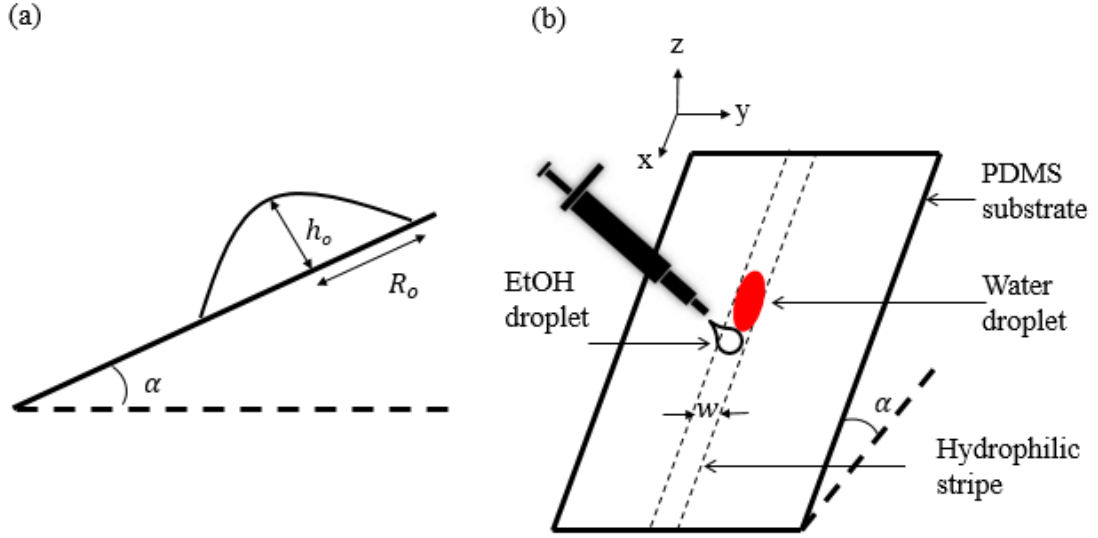
Figure 3.6: An illustration of (a) a water droplet of height h_o and radius R_o, resting on an incline of angle α, and (b) a schematic of the EtOH droplet deposited adjacent to the water droplet resting on an incline

In simulating the behavior of droplet flow on an inclined homogeneous or heterogeneous surface, we invoke a set of governing equations as follows (Darhuber et al., 2003a; Sellier et al., 2011):

$$\frac{\partial h}{\partial t} = -\frac{\partial q_x}{\partial x},$$
(3.1)

$$q_x = -\frac{h^3}{3\mu}\left(\frac{\partial p}{\partial x} - \rho g \sin \alpha\right) + \frac{\tau h^2}{2\mu},$$
(3.2)

$$p = -\sigma \left(\frac{\partial^2 h}{\partial x^2} + \frac{\partial^2 h}{\partial y^2} \right) - \Pi, \tag{3.3}$$

$$\frac{\partial ch}{\partial t} = -\frac{\partial}{\partial x}(cq_x) + D\frac{\partial}{\partial x}\left(h\frac{\partial c}{\partial x} \right), \tag{3.4}$$

where $h(x, y, t)$ is the droplet thickness normal to the substrate, q_x is the discharge, $p(x, y, t)$ is the pressure, γ is the surface tension, μ is the dynamic viscosity, $c(x, y, t)$ is the local concentration of EtOH and D is the diffusivity constant. For a uni-directional flow in the x-direction, the conservation of mass equation reduces to Eq. (3.1). The discharge expressed in Eq. (3.2) incorporates a pressure gradient, and a surface tension gradient represented by τ. Eq. (3.3) accounts for the balance of normal stresses at the small slope interface (Darhuber et al., 2003a) with a disjoining pressure term, Π, incorporated to remove the contact line singularity. Eq. (3.4) describes the conservation of the EtOH in the system. We further define the dependent variables in the governing equations as follows:

$$\Pi(h, h^*) = B\left[\left(\frac{h^*}{h} \right)^n - \left(\frac{h^*}{h} \right)^m \right], \tag{3.5}$$

$$h(x, y, t) = h_c(x, t)\left(1 - \frac{4y^2}{w^2} \right), \tag{3.6}$$

$$c = \frac{h_1}{h}, \tag{3.7}$$

$$\tau = -\frac{\partial \sigma}{\partial c} \cdot \frac{\partial c}{\partial x}, \tag{3.8}$$

for which the disjoining pressure term in Eq. (3.5) is a function of the precursor film of thickness h^*; a height h represented by both a centerline height, h_c and a width, w as expressed in Eq. (3.6), and a constant $B = \gamma(n-1)(m-1)(1-\cos\theta_0)/h^*(n-m)$, where $(n,m) = (3,2)$ are the exponents of the interaction potential, and θ_0 the equilibrium contact angle. The precursor thin film, h^* is introduced to remove the stress singularity occurring in problems with a moving contact line. According to Darhuber et al. (2003), if the width of the stripe is much smaller than the capillary length of the droplet, i.e. $w \ll l_c$, the droplet adopts a parabolic profile, resulting in an expression for droplet thickness as in Eq. (3.6). This assumption is valid for our case, since a trace width of 1 mm and a water capillary length of 2.7 mm results in a $w/l_c = 0.37$. A fictitious EtOH height h_1, introduced in Eq. (3.7), is to be substituted for the surface tension expression in Eq. (3.8). Using these derivations and integrating Eq. (3.2) and Eq. (3.3) over the width of the stripe, i.e. from $-w/2$ to $w/2$, we obtain an expression for the discharge as

$$Q_x = -\frac{h_c^3}{3\mu}w\left(\frac{\partial p}{\partial x} - \rho g \sin\alpha\right) - \frac{1}{\mu}\frac{\partial\sigma}{\partial c}\frac{4w}{15}\left(h_c\frac{\partial h_1}{\partial x} - h_1\frac{\partial h_c}{\partial x}\right), \tag{3.9}$$

and an expression for capillary pressure as

$$p = -\sigma\left(\frac{128}{315}\frac{\partial^2 h_c}{\partial x^2} - \frac{128}{35w^2}h_c\right) - B\left[\left(\frac{h^*}{h_c}\right)^2 - \frac{2}{3}\left(\frac{h^*}{h_c}\right)^3\right]. \tag{3.10}$$

Similarly, Eq. (3.4) can now be written as

$$\frac{2w}{3}\frac{\partial h_1}{\partial t} = -\frac{\partial}{\partial x}\left(\frac{h_1}{h_c}Q_x\right) + D\frac{2w}{3}\frac{\partial}{\partial x}\left(\frac{\partial h_1}{\partial x} - \frac{h_1}{h_c}\frac{\partial h_c}{\partial x}\right). \tag{3.11}$$

The derivations leading to Eq. (3.9), Eq. (3.10) and Eq. (3.11) are outlined in Appendix A. By substituting these variables:

$$\tilde{h}_c = \frac{h_c}{h_0}, \tilde{h}_1 = \frac{h_1}{h_0}, \tilde{h}^* = \frac{h^*}{h_0}, \tilde{x} = \frac{x}{l_0}, \tilde{p} = \frac{p}{p_0}, \tilde{c} = \frac{c}{c_0}, \tilde{t} = \frac{t}{t_0} \text{ and } \tilde{\sigma} = \frac{\sigma}{\sigma_0}, \tag{3.12}$$

along with the scales $P_0 = \frac{\sigma_0 h_0}{l_0^2}$, $T_0 = \frac{3\mu l_0^2}{P_0 h_0^2}$, and $\varepsilon = \frac{h_0}{l_0}$ we obtain the following dimensionless governing equations:

$$\frac{2}{3}\frac{\partial \tilde{h}_c}{\partial \tilde{t}} + \frac{\partial}{\partial \tilde{x}}\left\{-\tilde{h}_c^3\left(\frac{\partial \tilde{p}}{\partial \tilde{x}} - \frac{16}{35}\frac{B_0 \sin \alpha}{\varepsilon}\right) + \Sigma\left(\tilde{h}_c\frac{\partial \tilde{h}_1}{\partial \tilde{x}} - \tilde{h}_1\frac{\partial \tilde{h}_c}{\partial \tilde{x}}\right)\right\} = 0, \tag{3.13}$$

$$\tilde{p} + \frac{128}{315}\tilde{\sigma}\frac{\partial^2 \tilde{h}_c}{\partial \tilde{x}^2} - \frac{128}{35}\frac{l_0^2}{w^2}\tilde{\sigma}\tilde{h}_c = -B\frac{l_0^2}{h_0\sigma_0}\left[\left(\frac{\tilde{h}^*}{\tilde{h}_c}\right)^n - \frac{2}{3}\left(\frac{\tilde{h}^*}{\tilde{h}_c}\right)^m\right], \tag{3.14}$$

$$\frac{2}{3}\frac{\partial \tilde{h}_1}{\partial \tilde{t}} + \frac{\partial}{\partial \tilde{x}}\left\{-\tilde{h}_c^2\tilde{h}_1\left(\frac{\partial \tilde{p}}{\partial \tilde{x}} - \frac{16}{35}\frac{B_0 \sin \alpha}{\varepsilon}\right) + \Sigma\left(\tilde{h}_1\frac{\partial \tilde{h}_1}{\partial \tilde{x}} - \frac{\tilde{h}_1^2}{\tilde{h}_c}\frac{\partial \tilde{h}_c}{\partial \tilde{x}}\right)\right.$$
$$\left. - d\left(\frac{\partial \tilde{h}_1}{\partial \tilde{x}} - \frac{\tilde{h}_1}{\tilde{h}_c}\frac{\partial \tilde{h}_c}{\partial \tilde{x}}\right)\right\} = 0, \tag{3.15}$$

where $B_0 = \frac{\rho g l_0^2}{\sigma_0}$ represents the Bond number, $\Sigma = -\frac{\partial \tilde{\sigma}}{\partial \tilde{c}} \frac{4}{5} \frac{1}{c_0 \varepsilon^2}$ and $d = \frac{2D\mu}{h_0 \sigma_0 \varepsilon^2}$. These equations were then implemented and solved in COMSOL. The governing equations were first expressed in their weak form and the solution approximated by a trial function using quadratic Lagrange shape functions. COMSOL then uses the Galerkin method, whereby the test functions correspond to the shape functions to generate a system of algebraic equations, which can then be solved to generate the numerical solution. We found in our case that a mesh resolution of 5,000 elements was sufficient to generate a mesh independent solution. Note that we assumed Dirichlet boundary conditions at both ends, where h_c is set to h^* at both ends of the domain, and h_1 is set to 0 at the left-hand boundary and h_c at the right-hand boundary, leading to a concentration of 0 and 1, respectively. Natural boundary conditions apply for the pressure. The input parameters included: $\mu = 0.001$ Pa·s, $\rho = 1000$ kg/m^3, $g = 9.8$ m/s^2, $D = 3 \times 10^{-6}$ m^2/s, and $h^* = 0.02$. Also, for $V = 1$ μl, $w = 1$ mm, $\theta_o = 35^\circ$, we find $h_o = 0.5$ mm, and $l_o = 2R_o = 3.8$ mm. The derived expression for surface tension gradient, Σ, is represented as $\sigma = \sigma_e + (\sigma_w - \sigma_e)(1 - c)$ in the numerical model, where c takes on values between 0 to 1, and is initially given by a step function. Here, σ_e and σ_w represent the surface tensions of EtOH and water, with values 0.022 N/m and 0.072 N/m, respectively.

3.5 Numerical Results and Discussion

Considering the initial coalescence of the two droplets, only a small portion of the EtOH droplet actually interacted with the water droplet. This portion is *a-priori* unknown, but is visibly small. To capture this initial condition, we set the EtOH concentration, $c = 1$ past a distance X_c and $c = 0$ everywhere else. In other words: $h = h_1$ for $X > X_c$ and $h_1 = 0$ otherwise. Figure 3.7 shows the initial profiles of the water and EtOH droplets.
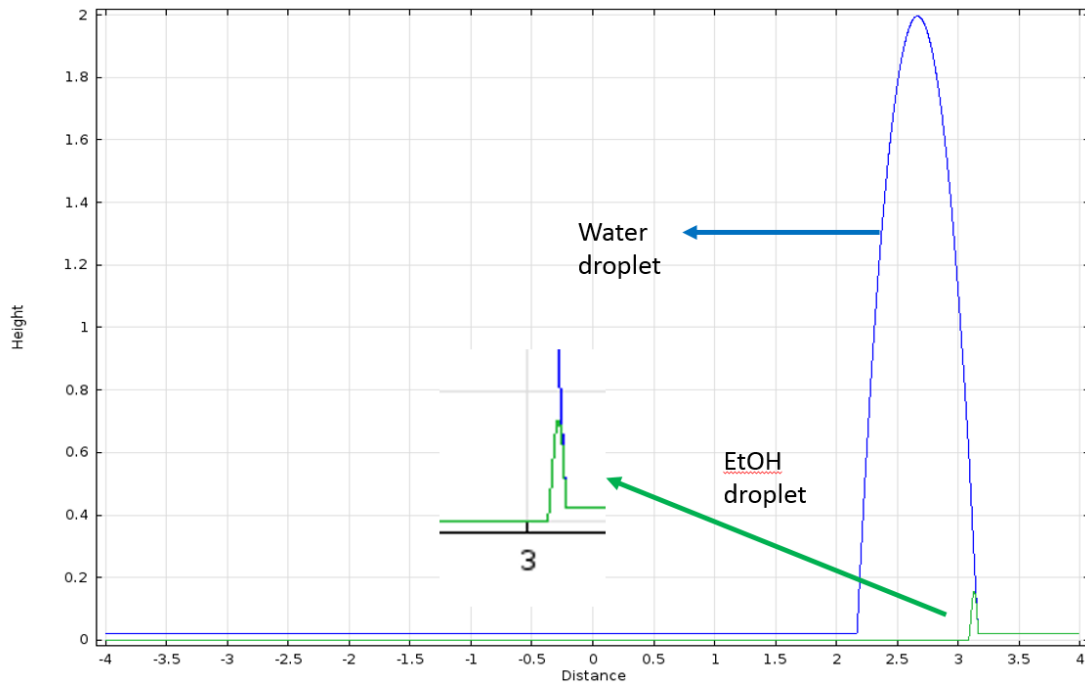
Figure 3.7: Initial profiles of the water and EtOH droplets for numerical simulation

The choice $X_c = 94\%$ of the initial droplet radius gave the best match to experimental results. Figure 3.8 compares the numerical and experimental results for a substrate inclination angle of 10°. For $X_c = 94\%$, the trend predicted by the numerical simulation is shown to be in good agreement with experimental results although the simulation appears to slightly over-predict the initial droplet velocity. The sensitivity of the numerical simulation to the parameter X_c is also illustrated on Figure 3.8 where it can be seen that the smaller X_c corresponding to a larger amount of EtOH in the droplet lead to a larger distance traveled and a larger initial velocity.

53
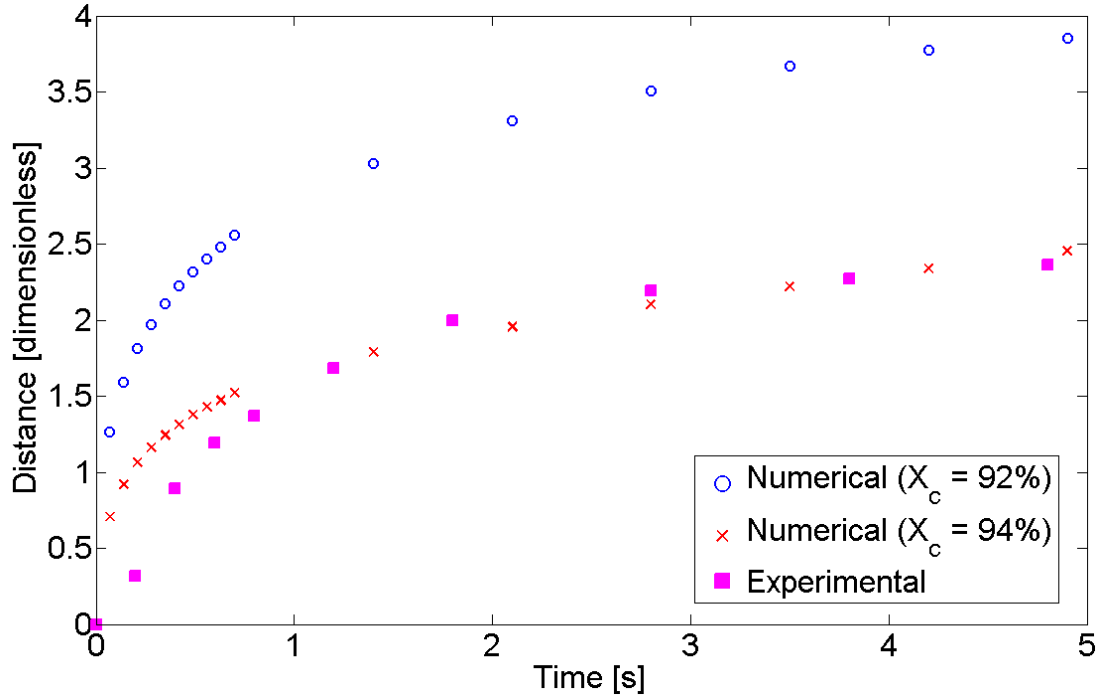
Figure 3.8: Comparison of the distance traveled measured experimentally and computed numerically. The *y*-axis shows the distance traveled normalized by the initial droplet length

To determine the distances traveled from our simulation, we analyzed the centers of gravity, X_{cg} through

$$X_{cg} = \frac{\int_0^L \int_{\frac{-w}{2}}^{\frac{w}{2}} (h - h^*) x \, dy \, dx}{\int_0^L \int_{\frac{-w}{2}}^{\frac{w}{2}} (h - h^*) \, dy \, dx}. \tag{3.16}$$

Figure 3.9 shows how the difference between the position of the center of gravity computed numerically and the total distance traveled measured experimentally (see Figure 3.5) varies with time. For all but the steepest inclined surface (24° inclination), the numerical results are seen to tend towards 0, indicating that the numerical results tend towards the experimental ones. Because the numerical simulation does not include

54

the effect of contact angle hysteresis, which would in practice generate an additional force resisting the motion, the numerical results are seen to overshoot slightly the experimentally observed distance traveled. This is particularly obvious for the flat surface (0° inclination), for which contact angle hysteresis would be the only resistive force beside viscous dissipation. For the most inclined surface of 24° inclination, the simulation still predicts the motion of the droplet, whereas the droplet could not be actuated experimentally. We attribute this difference again to hysteresis, which is not included in the numerical simulation.
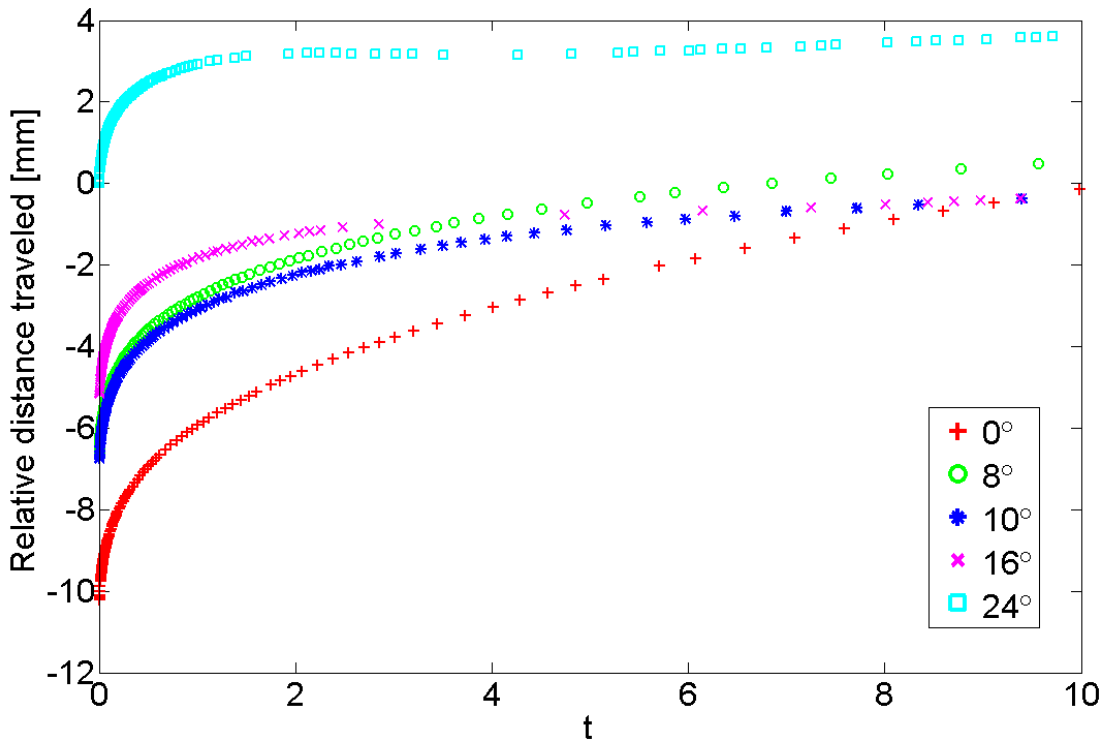
Figure 3.9: Traveled distance computed numerically relative to the measured one as per Figure 3.5

3.6   Additional Numerical Results

Our numerical simulations were able to predict the distance traveled using various trace widths, droplet volumes and droplet contact angles. The derivation for droplet volume in terms of trace width, droplet height and droplet length, as well as the derivation of contact angle in terms droplet height and droplet length are detailed in Appendix B. Simulations were performed by varying those parameters and the X_{cg} function was used to yield non-dimensional center of gravity values as a function of time, as shown in Figure 3.10.
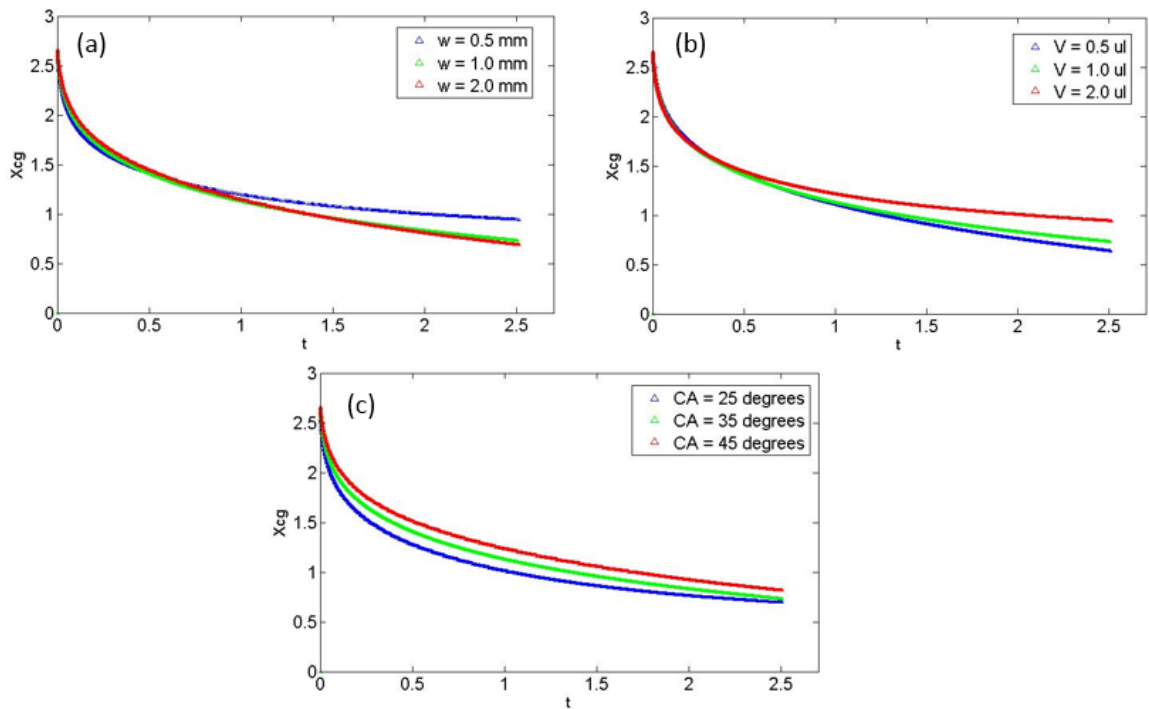
Figure 3.10: Center of gravity analysis for distance traveled until $t = 2.5$ s at 8° incline through varying (a) trace width, (b) droplet volume, and (c) contact angle

The distance traveled decreases as trace width decreases, as shown in Figure 3.10(a). As droplet volume is decreased, however, the distance traveled increased, as shown in Figure 3.10(b). All else equal, when the trace width is smaller or when the droplet volume is larger, we may assume that the droplet becomes more elongated within a trace. This may give rise to additional capillary stresses that may have exceeded Marangoni stress, hence the likeliness of not being displaced very far. It also suggests that a longer slug has a smaller Marangoni effect, hence a smaller driving force, resulting in a smaller distance traveled. We have experimentally shown that, on a horizontal plane, propulsion distance increases when volume increases from 0.5 µl to 1.0 µl (see Figure 3.4). However, according to our simulations, which was performed by specifying an 8° incline, we found that propulsion distance starts to decrease beyond 0.5 µl.

Figure 3.10(c) shows that a droplet with a lower contact angle, or a droplet on a more hydrophilic surface, travels further. A vectorial representation of two droplets of equal volume with contact angles $\theta_1 < \theta_2$, as shown in Figure 3.11, may aid in understanding this phenomenon. Assuming a surface tension gradient occurring in both droplets, the respective advancing and receding contact angles will differ. The net force for droplet 1 is $df^1 = df_a^1 - df_r^1$; similarly, the net force for droplet 2 is $df^2 = df_a^2 - df_r^2$. The driving force for droplet 1 is larger, since $df^1 > df^2$. Therefore, a droplet with a smaller contact angle travels further.
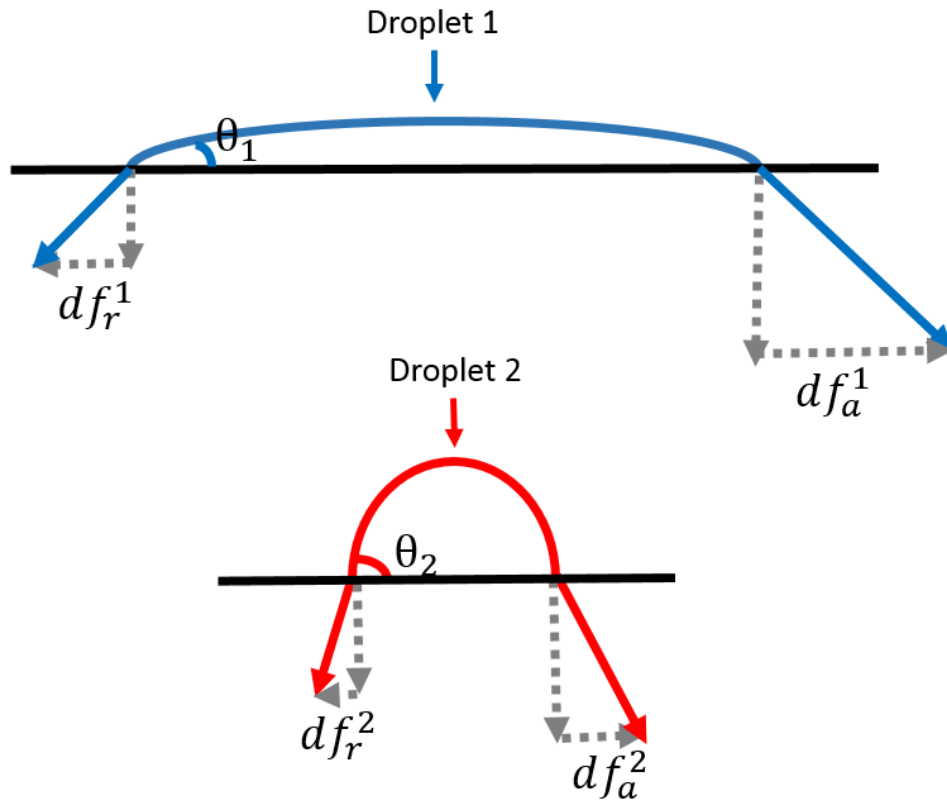
Figure 3.11: A diagram representing the effect of surface tension gradient on the forces acting on two droplets of differing contact angles, with $\theta_1 < \theta_2$

Figure 3.12 shows the dimensionless simulation results of not only the distance traveled, but also the droplet morphology as time progresses. The latter is advantageous especially when it is difficult to determine droplet height from image processing; for example, when small volumes are used. The height of a water droplet in a smaller trace width is lower than that in a larger trace width, as shown in Figure 3.12(a). The final length, however, is larger. This is simply a consequence of mass conservation in a narrower trace. Figure 3.12(b) shows that a 2.0 µl droplet, which is more elongated, travels less than a 0.5 µl droplet. Figure 3.12(c) shows that a droplet with a higher contact angle has a higher centerline height and travels less compared to a droplet with a lower contact angle.
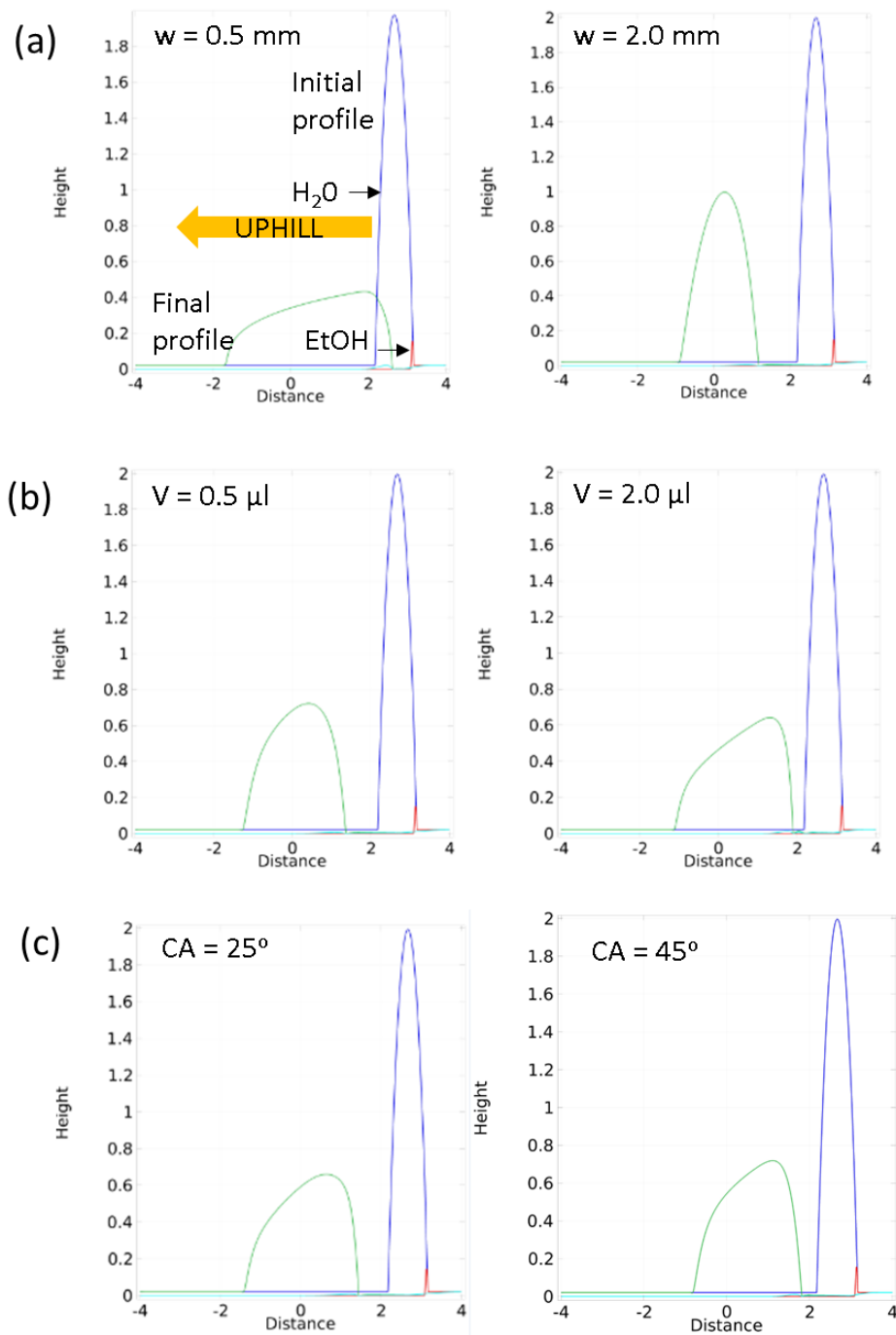
Figure 3.12: Dimensionless COMSOL simulation results for 4º incline and $t = 5.5$ s from varying (a) trace width, (b) droplet volume, and (c) contact angle. Uphill translation is represented by droplet movement from right to left

3.7 Conclusions

We have successfully shown the self-propulsion of a 1 µl droplet up an incline on a hydrophilic stripe fabricated on a piece of flat PDMS that has undergone oxygen plasma and PVP treatment. The distances traveled by the droplet as a function of angle of incline ranging from 0° to 24° were measured. We found that the distance traveled followed a linearly decreasing trend as angle was increased, before reaching zero at 24°.

Although our mechanism has been shown feasible, the use of a volatile liquid that is EtOH might not be suitable for biological applications, as alcohol kills cells. Based on our investigation, we may conclude that propulsion occurs when two droplets are:

i.   Miscible with each other

ii.   Forms a low contact angle when deposited on a substrate

Therefore, other substances that meet the requirements above can be used instead of EtOH if biological products were involved. A potential alternative would be to use two droplets of differing polypylene glycol (PG) concentrations on a treated surface such as corona-discharge-cleaned glass side, piranha-treated glass, flamed glass, and so on. This technique has resulted in the propulsion of two droplets, much like what we have shown, as reported by Cira et al. (2015).

Numerical solutions generated in COMSOL, which included capillary forces confined within a narrow stripe, as well as gravitational force, validated our experimental observations. Our studies suggest that gravitational pull and contact angle hysteresis overcomes Marangoni force at $\sim 24^o$, hence the sliding of the droplet downhill.

In summary, we have demonstrated a feasible method to move a droplet up an incline through self-propulsion, and developed a numerical simulation that allows for the understanding of the underlying physical principles and the prediction of distance traveled and droplet morphology through varying key experimental variables: trace width, droplet volume and contact angle.

4 Mixing Rate of Two Droplets

"It doesn't matter how beautiful your theory is, it doesn't matter how smart you are. If it doesn't agree with experiment, it's wrong." – Richard Feynman

The study of how surface tension gradients affect the mixing of liquids is beneficial in understanding applications that involve an air-liquid interface. This chapter presents the investigation of the mixing of a yellow food color (Tartrazine) droplet in an ethanol (EtOH) droplet. Though studies of droplet coalescence and mixing on a plane have been carried out, the effects of the air-liquid interface and the resulting non-uniform surface tension distribution were not well understood. In order to fill the knowledge gap, the impact of surface tension gradient, or Marangoni stress on the mixing of two droplets is studied and presented in this chapter.

Using yellow food color as the mixing material in water, we first evaluate how the mixing rate obtained from our proposed two-droplet system differs from the mixing rate that would occur if molecular diffusion alone was present. Second, we assess the impact of surface tension gradient through studying the mixing of Tartrazine in various EtOH concentrations. Our experimental results were compared against the numerical results obtained through a mathematical model built using COMSOL. The work presented in this chapter is currently under review by *European Journal of Mechanics/B Fluids*.

4.1 Introduction

Because of the continued interest in microfluidic systems, which play a major role in lab-on-a-chip applications, droplets have been studied for their ability to transport, collide, and mix with other droplets (Carroll and Hidrovo, 2013; Grigoriev et al., 2006; Lai et al., 2010; Muradoglu and Stone, 2005; Tanthapanichakoon et al., 2006). Laboratory tests that once required bigger samples and multiple-step processes involving constant human intervention, can now be simplified by manipulating small-volume droplets in a miniature device. One of the key parameters that govern the success of such applications is the mixing of droplets. This has direct implication on the reaction time of reagent under testing (Hessel et al., 2005; Lee et al., 2011; Stone et al., 2004).

To date, the most commonly reported methods of determining liquid diffusion coefficients include the Taylor dispersion method (Harris et al., 1993; Pratt and Wakeham, 1974; Taylor, 1953; Tominaga and Matsumoto, 1990), light scattering (Corti and Degiorgio, 1975; Paradies, 1980; Streletzky and Phillies, 1995), and pulsed-field gradient nuclear magnetic resonance (PFG-NMR) (Brown et al., 1989; Ghi et al., 2002; Holz et al., 2000). Though these methods provide a fundamental understanding of how a diffusion coefficient can be determined, none have investigated how the mixing rate is affected when an air-liquid interface is present.

Other works that study droplets in an air-liquid interface have been carried out, but most have only delved into the coalescence morphology of the interacting droplets. For example, through growing droplets from condensation to yield coalescence, Andrieu et al. (2002) found that the droplets merge into a spherical cap or a less elongated droplet. Sellier and Trelluyer (2009) performed a numerical simulation that showed two

droplets merging and finally becoming a spherical cap, confirming their empirical observations. Also, based on top view geometrical analysis, they showed that the radius of the neck region increases when the sum of the two droplets' radii decreases, culminating in coalescence. Eddi et al. (2013) showed two droplets brought together slowly with a needle to induce coalescence exhibited a neck height growth proportional to $t^{2/3}$ for contact angles less than 90°. At 90°, the height growth transitions to $t^{1/2}$. A more involved study was carried out by Karpitschka and Riegler (2014), where the group posited that whether two different but miscible droplets would coalesce or remain in a temporary non-coalescing state depends on the surface tension gradient, $\Delta\gamma$ and the average adjoining contact angle, $\bar{\theta}_a$. Fast and delayed coalescence of droplets with varying concentrations have been characterized by Borcia et al. (2011). A secondary droplet that formed after coalescence has been reported by Borcia and Bestehorn (2013), as a result of a surface tension gradient that exceeded a critical value. Numerical studies on the coalescence morphology of two identical droplets, and two droplets with different surface tensions have also been carried out Borcia and Bestehorn (2014).

The most recent characterization of the mixing of two droplets performed in the presence of an air-liquid interface was performed by Yeh et al. (2014). Their comprehensive results of chemical reaction and mixing using a two-droplet system show the formation of fingers when a NaOH droplet mixes with a phenolphthalein droplet. This phenomenon was attributed to thermal instabilities between the chemicals.

In our study, we investigate the mixing rate from the stand point of surface tension arising from the presence of an air-liquid interface. In addition, the effect of surface tension gradients arising from two different, but miscible liquids, is investigated.

Through experimental findings and numerical simulations, we provide an insight into the factors that affect the mixing of two liquid droplets.

4.2   Experimental Methods

This section details the materials, as well as the hardware setup used to conduct the experiments. To study the mixing rate, an ethanol (EtOH) droplet was coalesced with a droplet of yellow food color (Tartrazine E102, Hansells, New Zealand), used as received. The main ingredient in the food color is water. The EtOH solutions, prepared by diluting with deionized water, ranged from 0 - 90% by volume. Using a micropipette (0.2-10 µl Picus, Biohit), a 1 µl EtOH droplet was first deposited on a piece of planar polyethylene (PE) sheet, proceeded by the deposition of a 1 µl Tartrazine droplet slightly touching the EtOH droplet, in order to induce coalescence. The experiment was recorded at 500 frames per second using a setup consisting of a high-speed camera (PHOTRON Fastcam SA5), a high intensity light, and a recording software (PHOTRON Fastcam Viewer). The setup is shown in Figure 4.1.
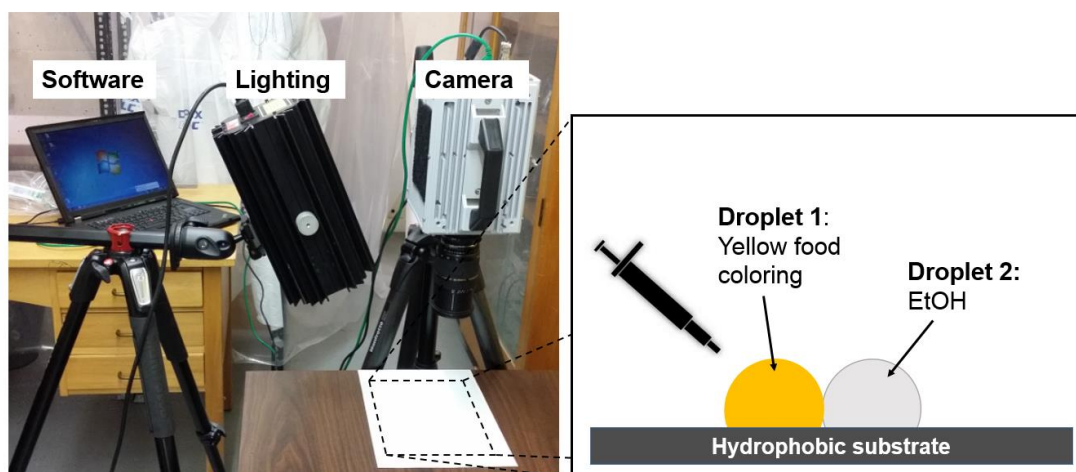
Figure 4.1: Setup consisting of a high-speed camera, a high intensity light, and a recording software, for the mixing experiment of two droplets on a hydrophobic substrate

Three runs were performed for every EtOH concentration tested. Judicious visual assessment of the individual frames were carried out to determine the time points at which the droplet starts coalescing, and the instant when the droplet stops mixing. According to the frames selected, we determined the area mixed through two methods: (a) by measuring the mixed area, and (b) by extracting a line profile from the mixed region. The difference in the area mixed and the line profiles were analyzed using the software packages ImageJ (Rasband, 1997) and Gwyddion (Nečas and Klapetek, 2012), respectively. The mixing time was determined as the time elapsed between the two frames selected, and was obtained through subtraction of the times recorded at both frames.

4.3 Experimental Results and Discussion

Using a goniometer (KSV Instruments), the measured contact angle of a 1 μl Tartrazine droplet on a PE sheet was 75°. This value is comparable to the measured contact angle of a distilled water droplet on PE: 73°.
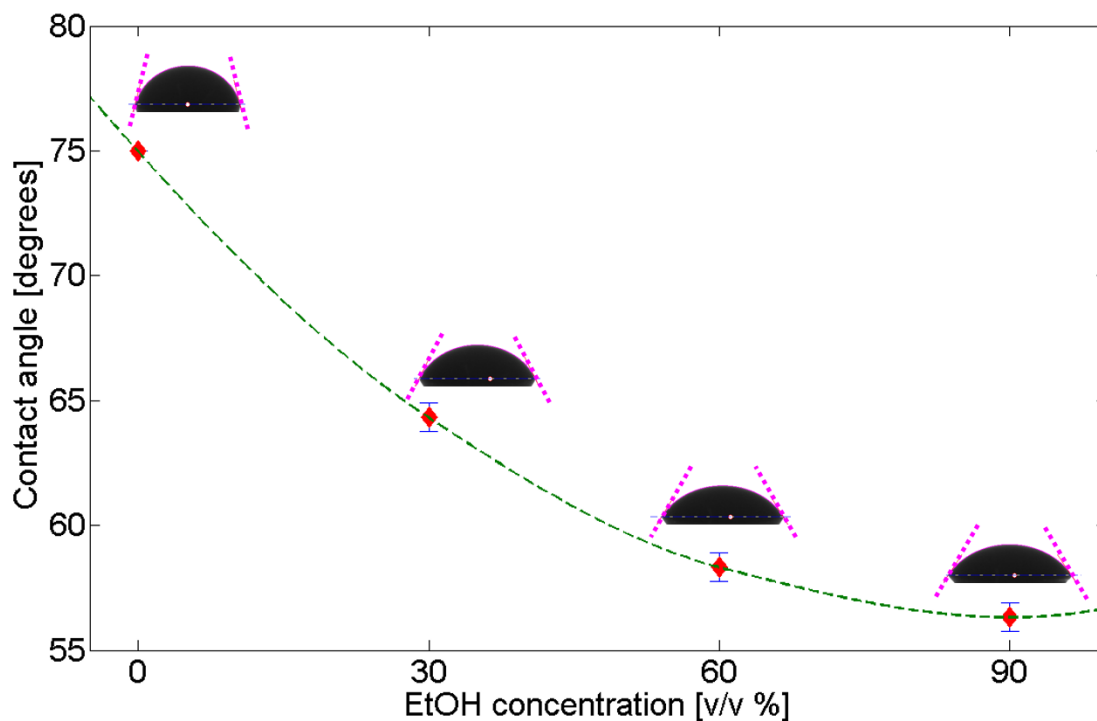
Figure 4.2: Contact angle of Tartrazine mixed in various EtOH concentrations. Images show the experimental droplet shape at the given concentrations

To study the contact angle formed when Tartrazine is mixed in EtOH, we took a 1 μl aliquot of various EtOH concentrations mixed with an equal volume of Tartrazine and measured its contact angle. As the EtOH concentration increases in the mixture, its contact angle decreases (see Figure 4.2). The measured contact angles ranged from 56° to 75° for Tartrazine mixed in EtOH concentrations of 0 to 90%.

Regardless of concentration, a 1 µl EtOH droplet pipetted onto a PE sheet resulted in a clear circular droplet. The use of 100% EtOH was omitted as the droplet formed was not stable due to rapid evaporation. Through a two-dimensional visual depiction (see Figure 4.3), our experiment can be categorized into four main stages:

(i)   Slight contact – the deposition of Tartrazine adjacent to the EtOH droplet to achieve a slight contact between the two droplets to induce coalescence

(ii)   Initial coalescence – the very instant Tartrazine enters the EtOH droplet

(iii)   Mixing regime – the subsequent traversal of Tartrazine in EtOH following initial coalescence

(iv)   Mixed state – the instant when Tartrazine reaches the entire boundary of the EtOH droplet
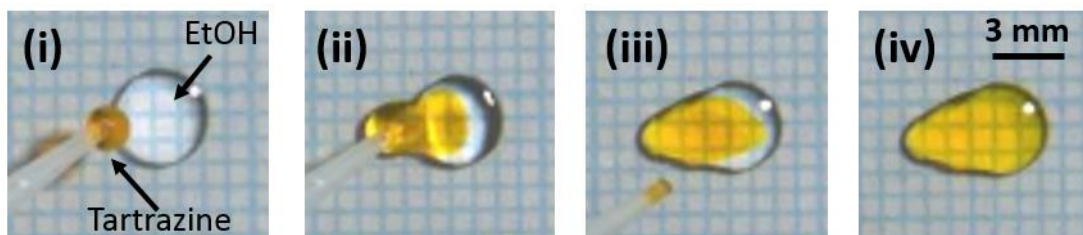
Figure 4.3: Visual depiction of the process stages: (i) slight contact, (ii) initial coalescence, (iii) mixing state, and (iv) mixed state

Our interpretation of the 'mixed-state' is analogous to the 'mixing length' definition used by Yeh et al. (2014) to describe the distance between the tip and the rear of the fingers formed during mixing. The mixed area is defined by the area traversed by Tartrazine following initial coalescence up to the mixed state. Visually, it is pictured as the clear area or pure EtOH region during initial coalescence (as in Figure 4.3(ii)). A graph paper placed underneath the PE sheet provided visual aid for quick assessment of the area. Analysis of the area mixed for all EtOH concentrations tested showed an increasing trend (Figure 4.4).
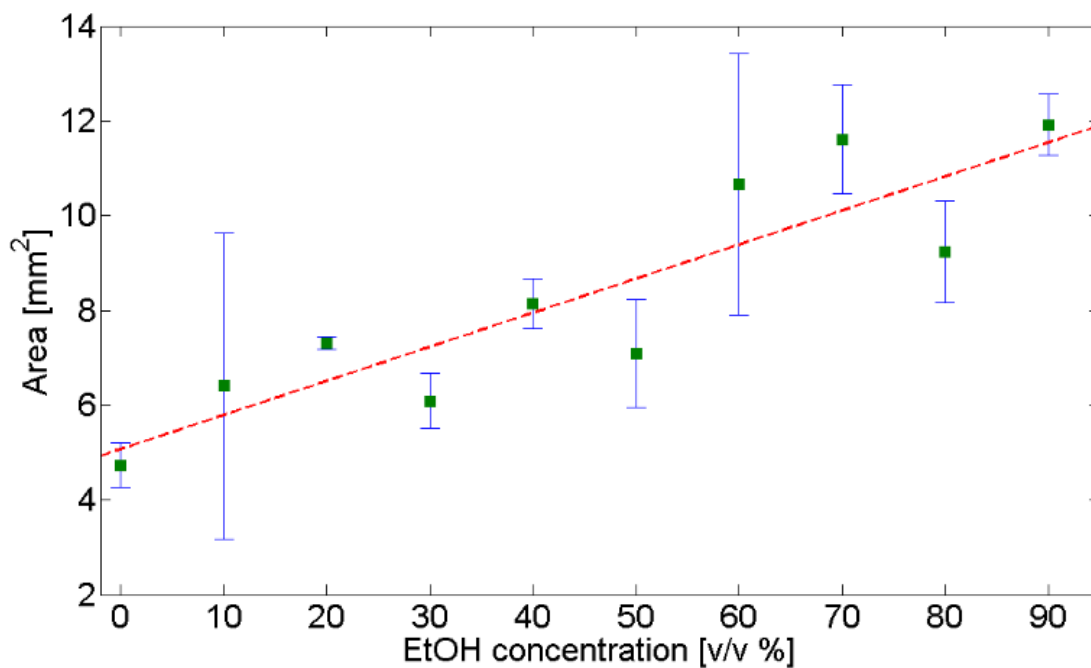
Figure 4.4: Area mixed by Tartrazine from the onset of coalescence to the mixed state, in various EtOH concentrations

The mixing time was then determined based on the time elapsed between the onset of coalescence to the onset of the mixed state. Shown in Figure 4.5, the Tartrazine droplet took a longer time to reach the mixed state with increasing EtOH concentration.
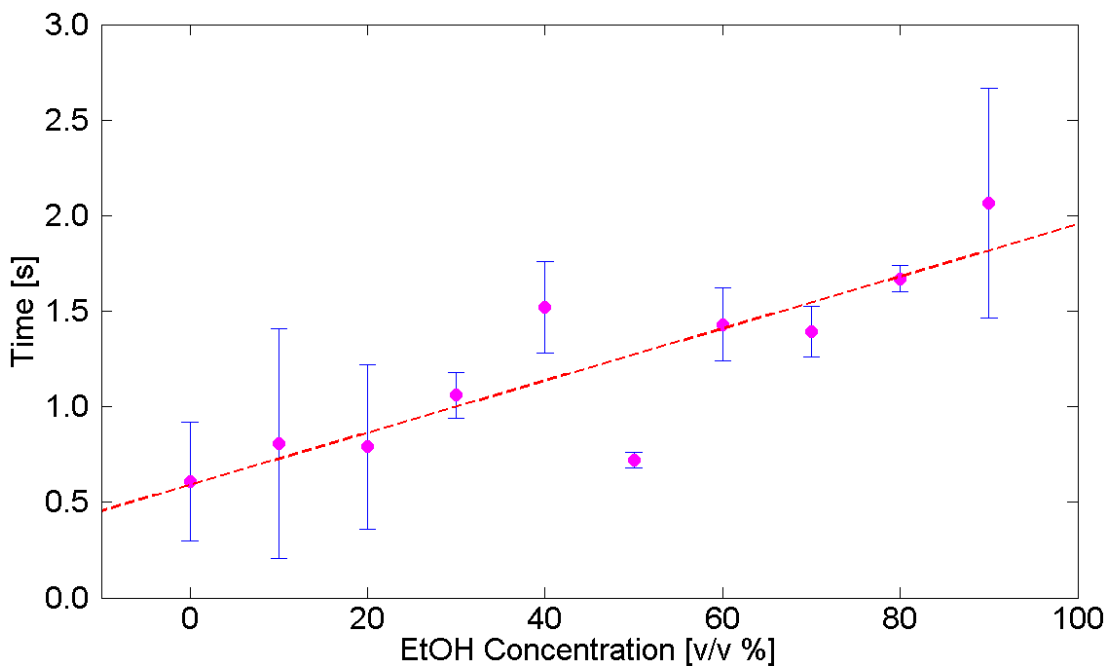
Figure 4.5: Mixing time of Tartrazine in various EtOH concentrations

The mixing rate was determined by taking the ratio of the area mixed to the mixing time. The mixing rate did not vary much with increasing EtOH concentration, and the average mixing rate obtained was 8.21×10^{-6} m^2/s. (Figure 4.6). The mixing rate of Tartrazine in only water, i.e. 0% EtOH, was calculated to be 9.22×10^{-6} m^2/s.

Previous works on the mixing of Tartrazine in water are scarce, and the closest comparison we were able to make was through the work of Werts et al. (2012), where a molecular diffusion of Tartrazine in a phosphate-buffered saline solution (PBS; 10 mM phosphate buffer at pH 7.4 with 137 mM NaCl and 2.7 mM KCl in water) was reported. The diffusion coefficient obtained was 4.9×10^{-10} m^2/s, measured using the ratiometric microfluidic H-filter method, which does not incorporate the effects of Marangoni since it was performed in an enclosed microchannel. Using the pendant droplet method, we measured the surface tension value of a Tartrazine droplet

70

(Goniometer, KSV Instruments) and found it to be ~137 mN/m, almost twice that of distilled water (γ_{water} ~72 mN/m). Clearly, the gradient in surface tension had played a role in the improvement of overall mixing rate.

We then analyzed our values obtained from mixing Tartrazine in aqueous EtOH solutions. Because none have reported the mixing of Tartrazine in EtOH, we compared our values with those reported by previous works pertaining to the molecular diffusion of EtOH in water, since the main ingredient in the Tartrazine solution is water. To date, all measurements reported values in the 10^{-9} m^2/s range, obtained using enclosed setups, i.e. without the effects of Marangoni. For instance, Hammond and Stokes (1953) and Easteal and Woolf (1985) used the diaphragm cell method; Pratt and Wakeham (1974), Tominaga and Matsumoto (1990) and Harris et al. (1993) used the Taylor dispersion method.
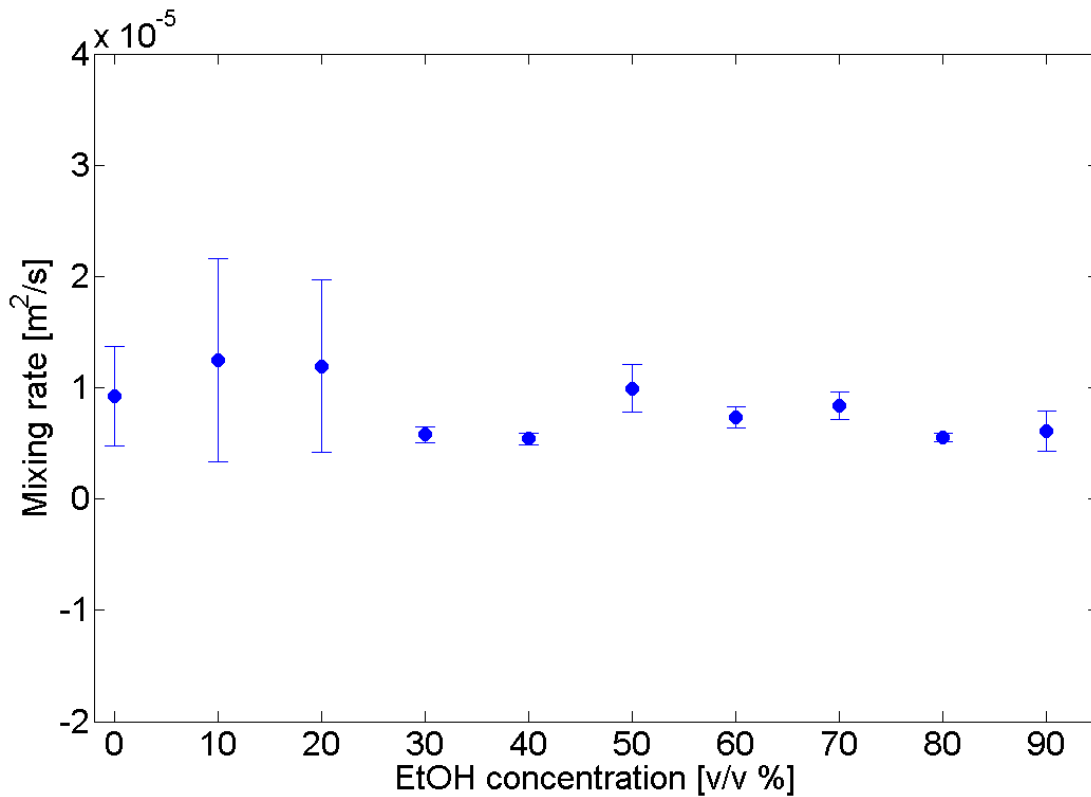
Figure 4.6: Mixing rate determined from the area mixed by Tartrazine in various EtOH concentrations

Our second method of determining the mixing rate involved extracting a line profile across the mixed region of the droplets. A similar method has been reported by Hessel et al. (2005) to show concentration profiling along a cross-section, presented as values of optical properties. As shown in Figure 4.7, we chose two consecutive frames, where Profile 1 precedes Profile 2, to visually depict the mixing of Tartrazine in EtOH. At the onset of coalescence shown in Profile 1, a line profile was extended to span the clear EtOH and part of the Tartrazine that has coalesced into the EtOH droplet. The unmixed region refers to the clear EtOH region. Following that, in Profile 2 where mixing has occurred, the same line profile spans the same location, only this time it covers the

mixed region, where the region formerly depicted as only EtOH (Profile 1) is now occupied by Tartrazine.
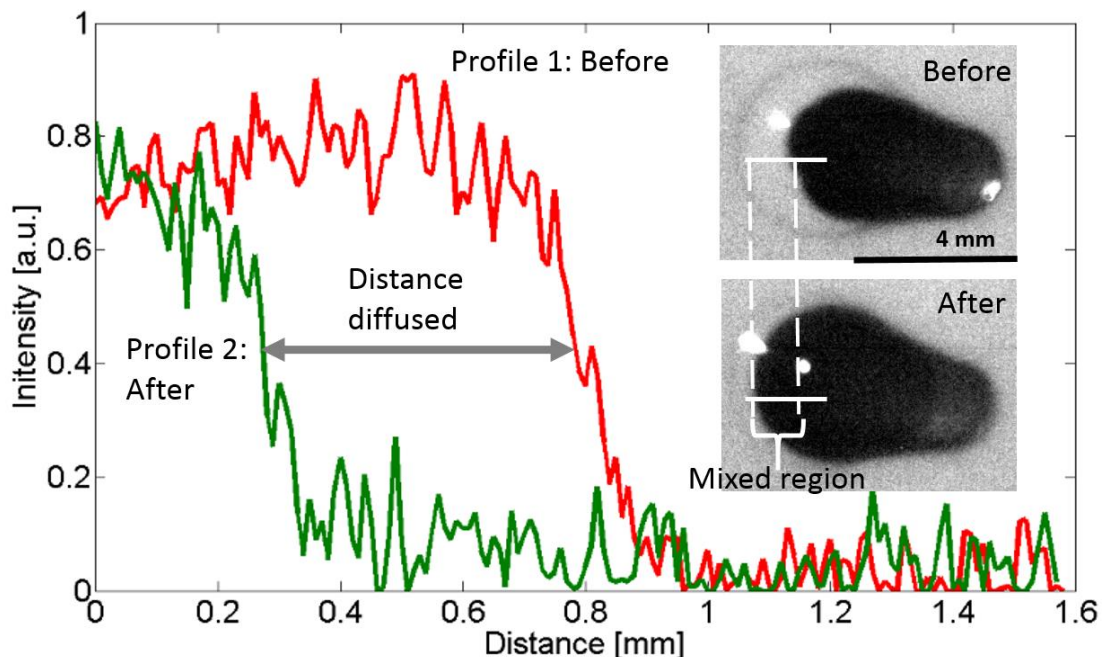
Figure 4.7: Intensity vs. distance mixed for a Tartrazine droplet in 70% EtOH

From the line profiles, the intensity values as a function of the line positions was obtained. Both profiles showed the same trend, where an abrupt dip in intensity was observed at the intersection between the clear and the dark regions. The distances corresponding to the middle points of the abrupt change in intensities were determined for both profiles. The difference between the two values gave the distance of the mixed region.

We then calculated the mixing rate by evaluating x^2/t, where x is the distance of the mixed region, and t is the elapsed time between the two profiles. Through a linear regression fit, the values obtained using this method was found comparable to the ones obtained using area measurement, as shown in Figure 4.8. The value of the slope was

-3.33 × 10^{-8}. This finding confirmed our initial results that the increase in EtOH concentration did very little in changing the mixing rate. The average mixing rate obtained from the line profile extraction method was 8.22 × 10^{-6} m^2/s. Our methods of determining mixing rate were analogous to the mixing quantification reported by Krasnopolskaya et al. (1999), in which both the elements of area and intensity were taken into account.
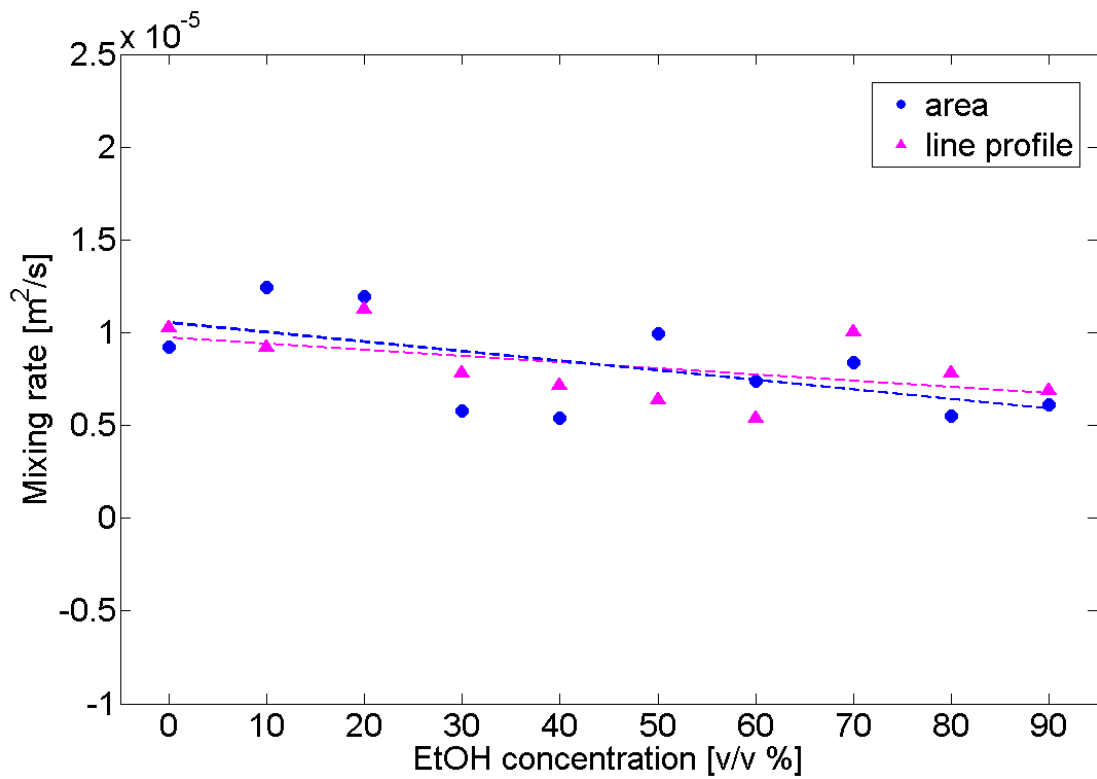
Figure 4.8: Comparison of the mixing rate values obtained using line profile extraction and area measurement of the mixed droplets

4.4 Numerical Model

To verify our results, we modeled our experiments by first constructing a spherical cap that represented the initial droplet. The formula for the volume of a spherical cap is given by

$$V_{cap} = \frac{1}{6}\pi h(3a^2 + h^2),$$

(4.1)

where a and h are the radius and the height of the spherical cap, respectively. Substituting the trigonometric relations

$$a^2 = 2Rh - h^2,$$

(4.2)

and

$$\alpha = \sin^{-1}\left(\frac{R - h}{h}\right),$$

(4.3)

we obtain

$$V_{cap} = \frac{1}{3}\pi R^3(2 - 3\sin\alpha + \sin^3\alpha),$$

(4.4)

where R is the radius of the hemisphere, and $\alpha = 90^{\circ} - $ *contact angle*. Using experimental values of $V_{cap} = 2$ μl and an intermediate measured contact angle value of 64° (see Figure 4.2), we obtained $a = 1.21$ mm and $h = 0.76$ mm. These dimensions were used to construct a spherical cap for our model. Using the *Laminar Two-Phase Flow, Moving Mesh Physics* in COMSOL, the effects of surface tension gradient were incorporated by specifying the surface tension coefficient, σ of the combined

Tartrazine and EtOH droplet, modeled as one coalesced droplet. The equation that models the air-liquid interface is

$$\mathbf{n} \cdot \mathbf{T} = -p_{ext}\mathbf{n} + \sigma(\nabla_t \cdot \mathbf{n})\mathbf{n} - \nabla_t \sigma, \tag{4.5}$$

where $\mathbf{n}$ is the normal to the interface, $\mathbf{T}$ is the stress tensor, ∇_t is the surface gradient, p_{ext} is the external pressure, and $\nabla_t \cdot \mathbf{n}$ is the surface divergence of the normal vector. The initial conditions include a spherical cap with zero internal velocity, zero external pressure, and a combined surface tension, σ expressed as $0.072 + (0.021 - 0.072) * c$, where c was set to 0 for $t < 0$ and 1 for $t > 0$. To incorporate the effects of gravity, $F = \rho g$ was specified, where $\rho = 999.97$ kg/m^3, to solve for the velocity field, $\mathbf{u}$ through the following Navier-Stokes equation modeled in COMSOL:

$$\rho \frac{D\mathbf{u}}{Dt} = \nabla \cdot [-p\mathbf{I} + \mu(\nabla\mathbf{u} + (\nabla\mathbf{u})^T) + F]. \tag{4.6}$$

To account for the frictional force between the liquid and the solid interface, the following equation

$$\boldsymbol{F}_{fr} = -\frac{\mu}{\beta}\mathbf{u}, \tag{4.7}$$

was included, with μ denoting the dynamic viscosity, and $\beta = 0.2 * h$ representing the slip length for a mesh element size of h (COMSOL Multiphysics, 2015). In addition, to incorporate molecular diffusion and convection within the droplets, the *Convection-Diffusion Equation Physics* was included in our model to solve

$$\frac{\partial c}{\partial x} + \nabla \cdot (-D\nabla c) + \boldsymbol{A} \cdot \nabla c = 0, \tag{4.8}$$

where c is the concentration, D the diffusion coefficient, and $\boldsymbol{A}$ the velocity. This feature allowed for the varying of the diffusion coefficient. The dynamic boundary condition is defined by zero flux at the solid surface and free surface:

$$\frac{\partial c}{\partial x} = \frac{\partial c}{\partial y} = \frac{\partial c}{\partial z} = 0. \tag{4.9}$$

The kinematic boundary condition at the free surface is given by

$$\frac{\partial h}{\partial t} + u\frac{\partial h}{\partial x} = w \qquad \text{on } z = h, \tag{4.10}$$

The efficacy of the model built was first verified by testing different diffusion coefficient values. We define how well mixing is by expressing the concentration deviation per volume as

$$\delta c = \frac{1}{2}\int (c - c_{eq})^2 d\Omega, \tag{4.11}$$

where c_{eq} represents the equilibrium concentration. Therefore, δc approaches 0 as the droplets reach the fully mixed state. This formula is analogous to the mixing index, M_i reported by Lai et al. (2010). From the combined surface tension equation, $\sigma = 0.072 + (0.021 - 0.072) * c$, we have defined c as a step function, i.e. $0 < c < 1$. Therefore, at concentration equilibrium, c_{eq} needs to be 0.5 to represent equal concentration of water and EtOH. As such, Eq. 4.11 can be computed as

$$\delta c = \frac{1}{2}\int (c - 0.5)^2 d\Omega, \tag{4.12}$$

Using molecular diffusion values of $D = 1 \times 10^{-6}, 1 \times 10^{-7}$ and 1×10^{-8} m²/s, the concentration deviation decayed exponentially with time before reaching the mixed state at concentration 0 (Figure 4.9). Also, our model verified that it took longer to reach the mixed state when the molecular diffusion coefficient is smaller, as one would expect.

4.5 Numerical Results and Discussion

Using diffusion values of $D = 1 \times 10^{-6}, 1 \times 10^{-7}$ and 1×10^{-8} m²/s, as well as a contact angle of 90° to run our simulations, the concentration deviation, δc decayed exponentially with time before reaching the mixed state at concentration 0 (Figure 4.9). Also, our model verified that it took longer to reach the mixed state when the diffusion coefficient is smaller, as one would expect.
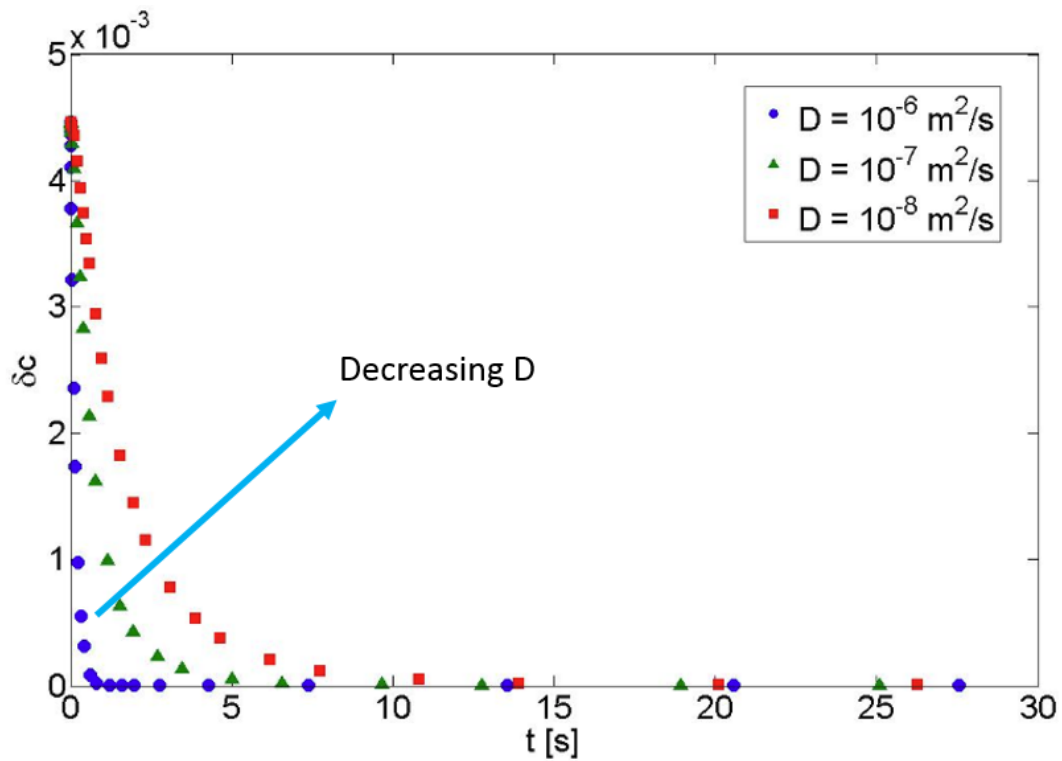
Figure 4.9: Simulated non-dimensional values of concentration deviation vs. mixing time for various diffusion coefficients, with Marangoni effects

We predicted a similar trend if surface tension effects were disregarded. To that end, we ran a simulation using only the *Convection-Diffusion* model with velocity field set to 0, to give us the molecular diffusion time. While the trend was similar to that when surface tension was incorporated, the time it took to reach the mixed state was higher by one order of magnitude, as shown in Figure 4.10.
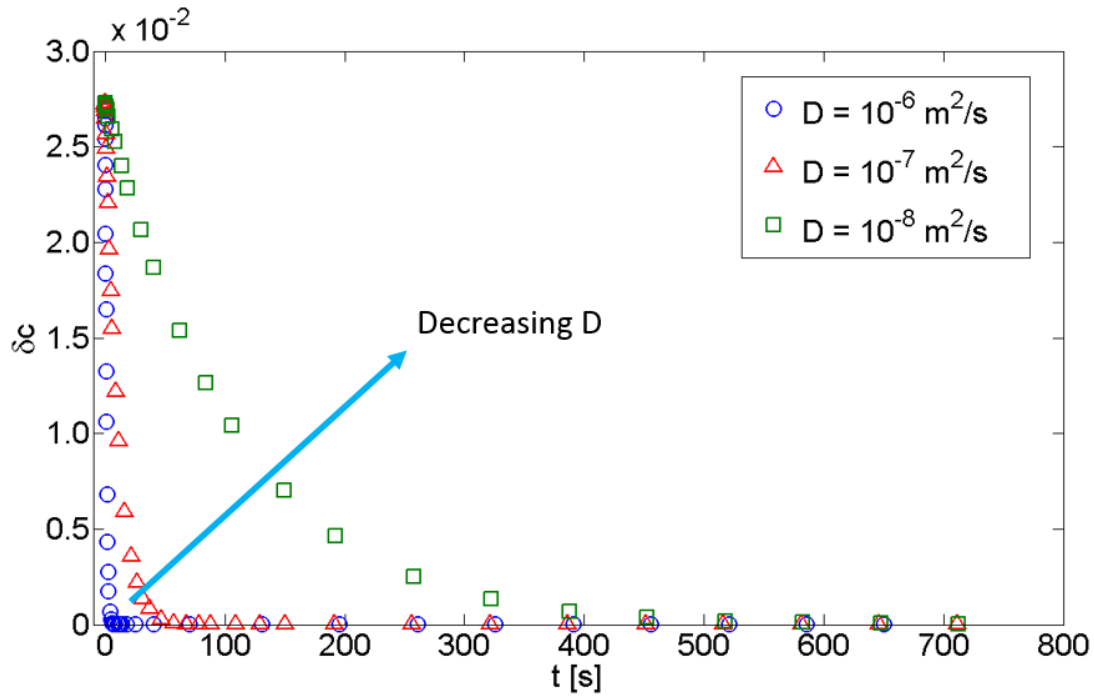
Figure 4.10: Simulated non-dimensional values of concentration deviation vs. mixing time for various diffusion coefficients, without Marangoni effects

To quantify the impact of surface tension gradient on mixing, the values for the time constant, τ obtained from fitting a semi-log plot from the individual exponential decay plots presented in Figure 4.9 and Figure 4.10 were compared. The values for τ were calculated as the inverse of the slopes. We found that with surface tension, or with Marangoni, the time it took to reach the mixed state was always lower, compared to only molecular diffusion, or without Marangoni. A 4% improvement in τ was observed $D = 1 \times 10^{-6}$ m^2/s, followed by a 42% improvement for $D = 1 \times 10^{-7}$ m^2/s and an 87% improvement for $D = 1 \times 10^{-8}$ m^2/s (see Figure 4.11). These results showed that surface tension gradient played a more significant role at smaller diffusion coefficient values, as one would expect. Similarly, Blanchette (2010) performed simulations that showed significant mixing induced by surface tension gradients.
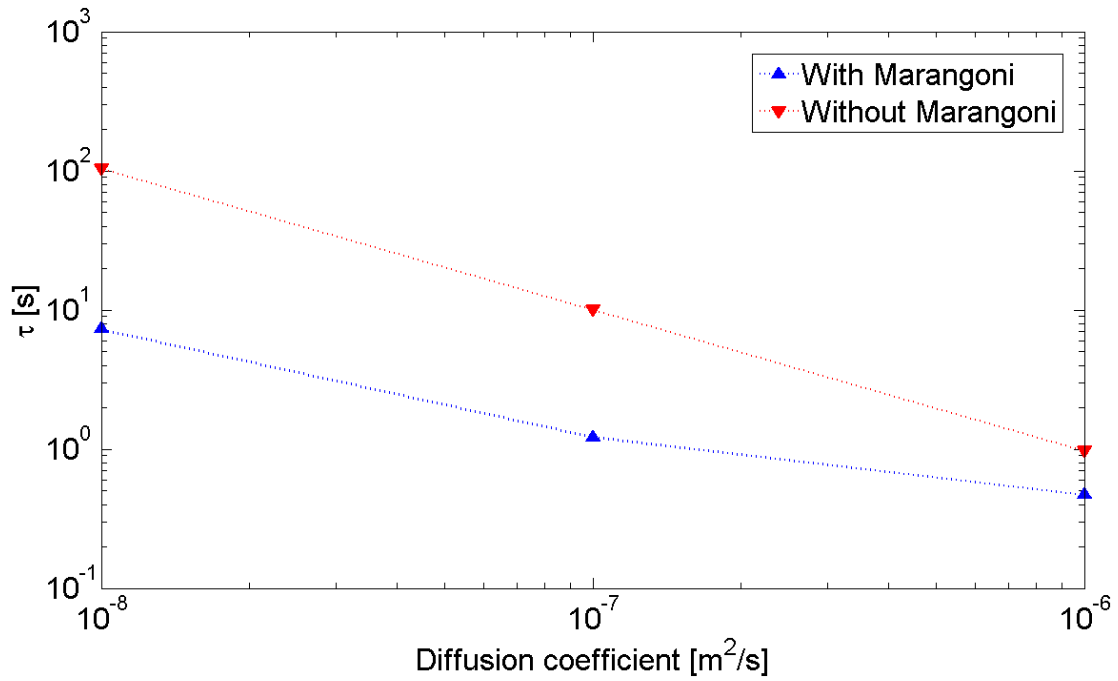
Figure 4.11: Time constant vs. diffusion coefficient for simulations with and without Marangoni effects

We then tested the impact of varying EtOH concentration, which was manifested as different surface tension values in the model. This was accomplished through the combined surface tension expression stated earlier in the form: $0.072 + (s - 0.072) *$ c, where s is now the surface tension of various aqueous EtOH solutions, obtained from Vazquez et al. (1995). The values of s used in our simulations are as shown in Table 4.1.

Table 4.1: Surface tension, *s* values corresponding to aqueous EtOH solutions

EtOH (v/v %)	*s*
0	0.072
20	0.038
40	0.030
60	0.026
80	0.024
100	0.022

Our simulation showed little to no variation in mixing time for the concentrations tested (Figure 4.12). This agrees with our experimental results (Figure 4.8), where the mixing rate of Tartrazine in various EtOH concentrations were almost constant.
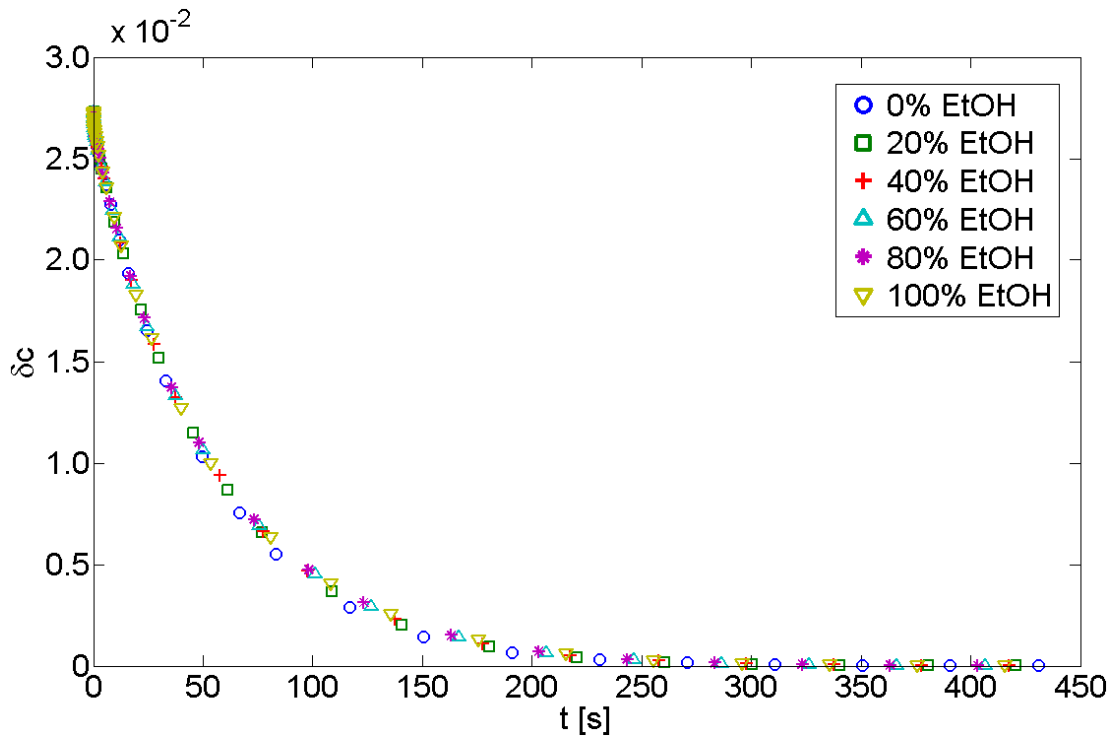
Figure 4.12: Simulated non-dimensional values of concentration deviation vs. mixing time for various EtOH concentrations

We then ran the simulation using our measured contact angle values (see Figure 4.2). As shown in Figure 4.13, the concentration deviation is slightly higher for lower contact angles. This could be due to the area being larger for a higher contact angle droplet, hence the higher likelihood for the stretching and folding of liquid. In spite of the deviations, a mixing time of $\sim 0.8 - 0.9$ s was found for all the contact angle values. Experimentally, we found that the mixing time ranges from 0.6 s to 2 s (see Figure 4.5) for the EtOH concentrations $(0-90\%)$ corresponding to the contact angle values tested. Although it was not an exact match, our simulation was able to predict a mixing time that was still within the values obtained experimentally.
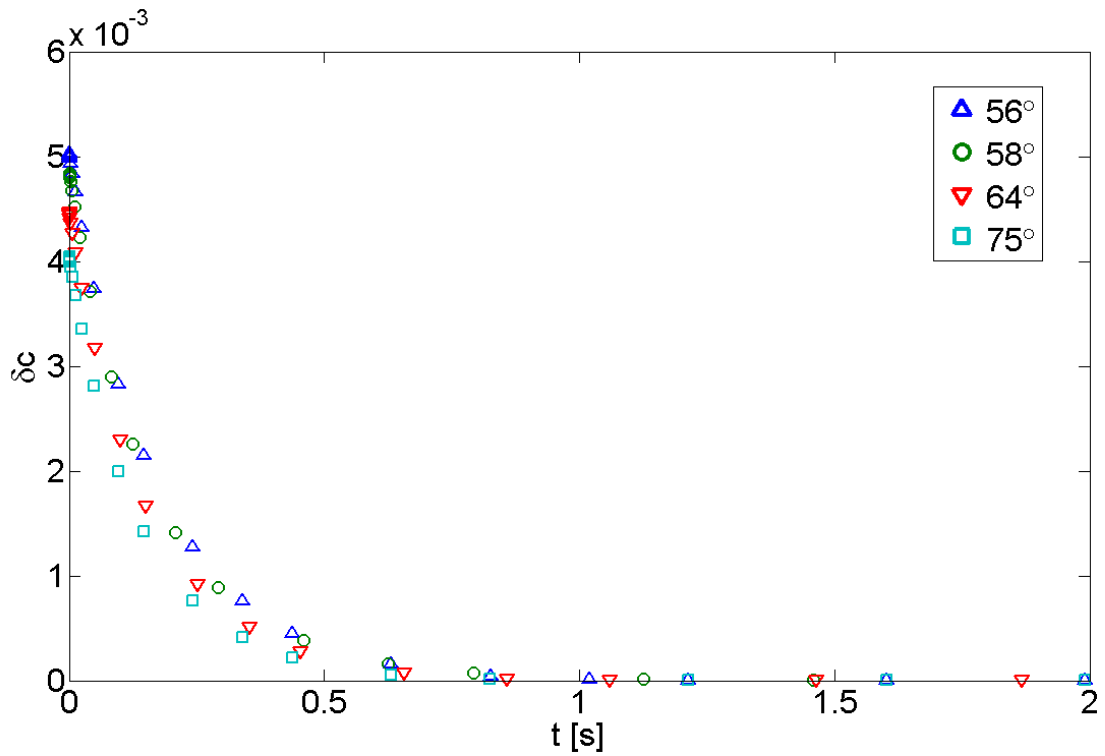
Figure 4.13: Simulated non-dimensional values of concentration deviation vs. mixing time using experimental values of contact angle

4.6 Additional Numerical Results

To better understand the impact of contact angle on mixing time, we widened the range of contact angle values used in our simulation. As shown in Figure 4.14, it takes longer to reach the mixed state at a smaller contact angle; for example, a 20° droplet takes almost twice as much time compared to a 90° droplet.
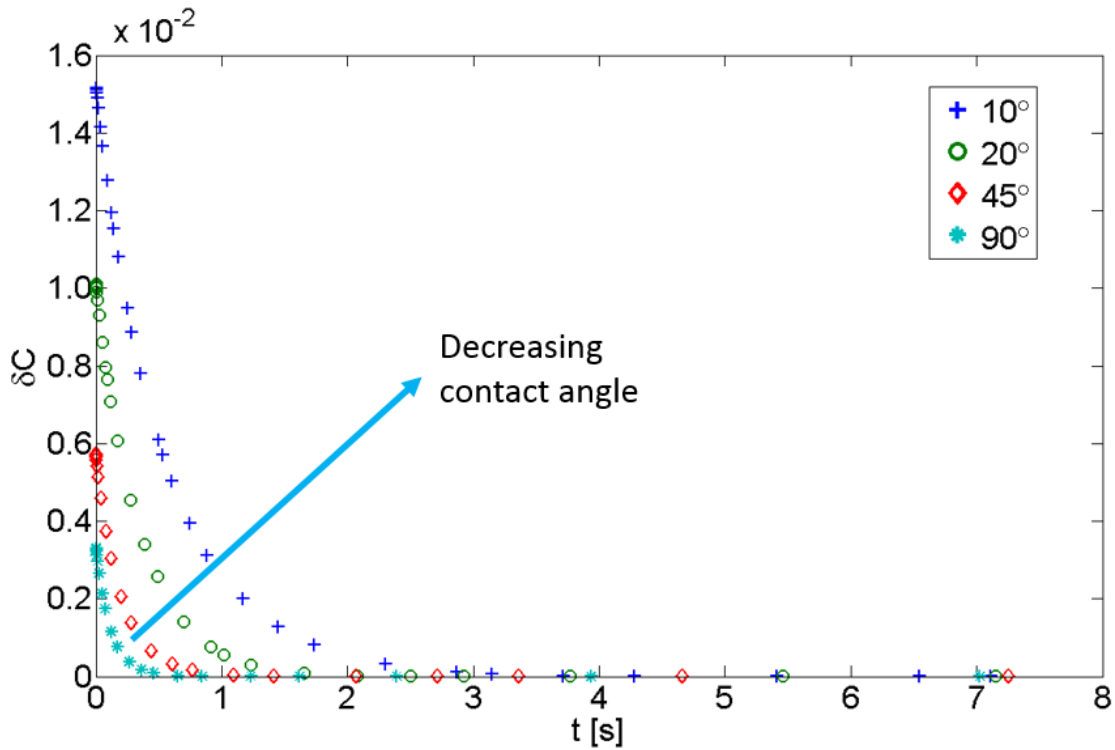
Figure 4.14: Simulated non-dimensional values of concentration deviation vs. mixing time for various contact angles ($D = 10^{-6}$ m^2/s)

Since volume is fixed in our simulations, a 20° droplet would occupy a larger footprint than a 90° droplet. According to Fick's law of diffusion, $J = -D\frac{dc}{dx}$, the amount of diffusing substance for a given time, J is smaller when the length that the substance has to travel, x is larger. This explains the results of our simulations, in addition to implying that a droplet on a hydrophobic surface mixes more efficiently than a droplet on a hydrophilic surface.

To understand the dynamics of the mixing droplets, we analyzed the velocity field and streamlines for various contact angles. The contact angle value is specified under the *Wall-Fluid Interface*, where necessary forces are applied by the software during

simulation to bring the contact angle towards its equilibrium value. The flow in a 20º droplet is unidirectional and lateral at the beginning of interaction, as shown in Figure 4.15(a). At $t = 3.5$ s, fluid flows from the bulk towards the air-liquid interface, where surface tension is higher. The streamlines show a symmetrical flow from the edge towards the peak of the droplet. From $t = 0.5$ s to $t = 3.5$ s, the velocity magnitude at the surface had decreased by two to three orders of magnitude.
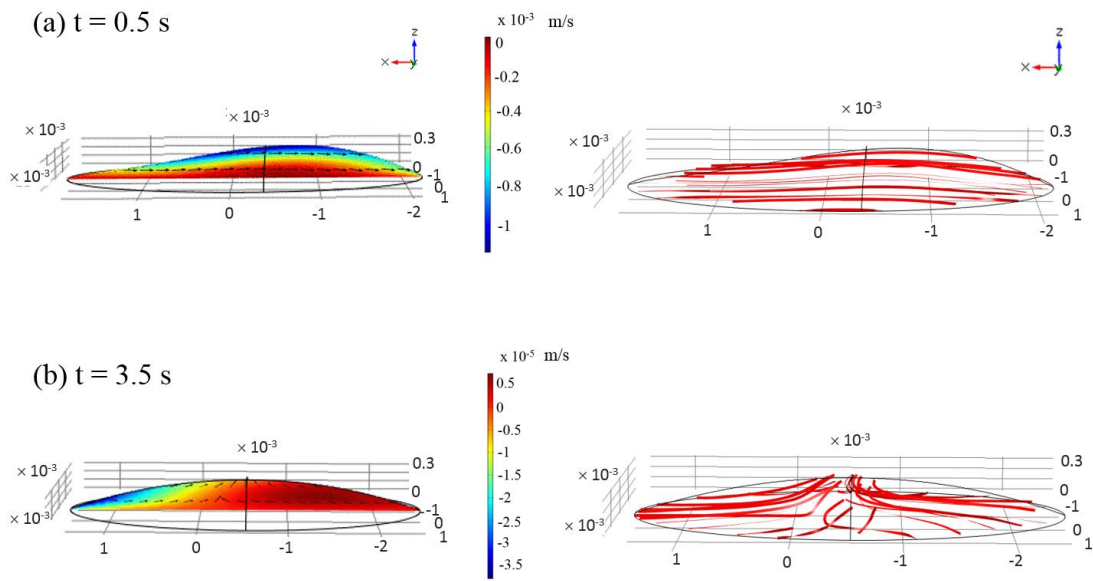
Figure 4.15: Velocity field (left) and streamlines (right) in a 20º contact angle droplet at (a) 0.5 s and (b) 3.5 s

For a 90º droplet, a recirculation from the middle of the droplet towards the surface where surface tension is higher, appears as soon as interaction began, as shown in Figure 4.16(a). The streamlines at $t = 0.1$ s show two symmetrical vortices that meet at the center of the droplet. At $t = 1$ s, a second recirculation in the reverse direction appeared, resulting in a stagnation point. From $t = 0.1$ s to $t = 1$ s, the velocity magnitude at the surface had decreased by two orders of magnitude. Our results imply

that a recirculating flow, rather than a lateral flow, improves the rate of mixing. Also, a 20° droplet tends to deform more compared to a 90° droplet upon mixing, as evident from Figure 4.15 and Figure 4.16.

(a) t = 0.1 s

(b) t = 1 s
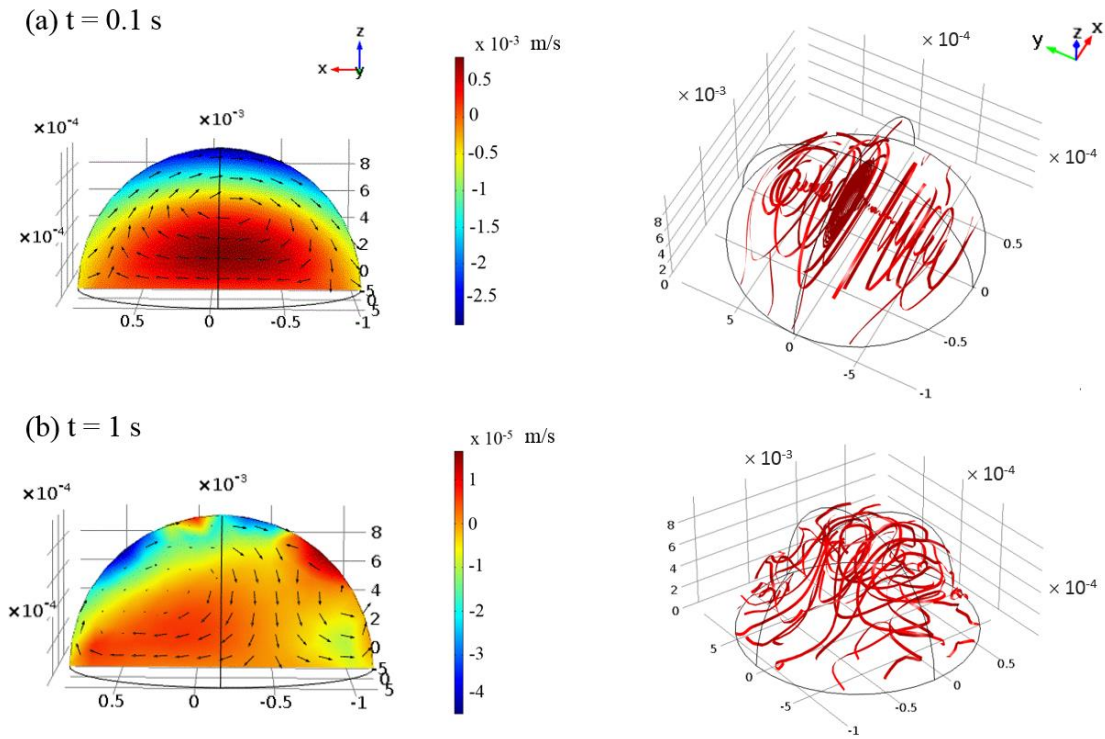
Figure 4.16: Velocity field (left) and streamlines (right) in a 90° contact angle droplet at (a) 0.1 s and (b) 1 s

Figure 4.15 and Figure 4.16 also show the displacement of the droplet, observed as the shift of the droplet centerline from the origin. Surface tension gradient is expected to induce motion of the droplet system in the absence of hysteresis (Sellier et al., 2011, 2013). We indeed observed in our simulations that the center of gravity of the system shifts in the direction of increasing surface tension. In addition, we observed that a droplet displaces sooner and further for a lower contact angle, as shown in Figure 4.17.

We have previously shown that a droplet with lower contact angle travels further (Ng et al., 2016).
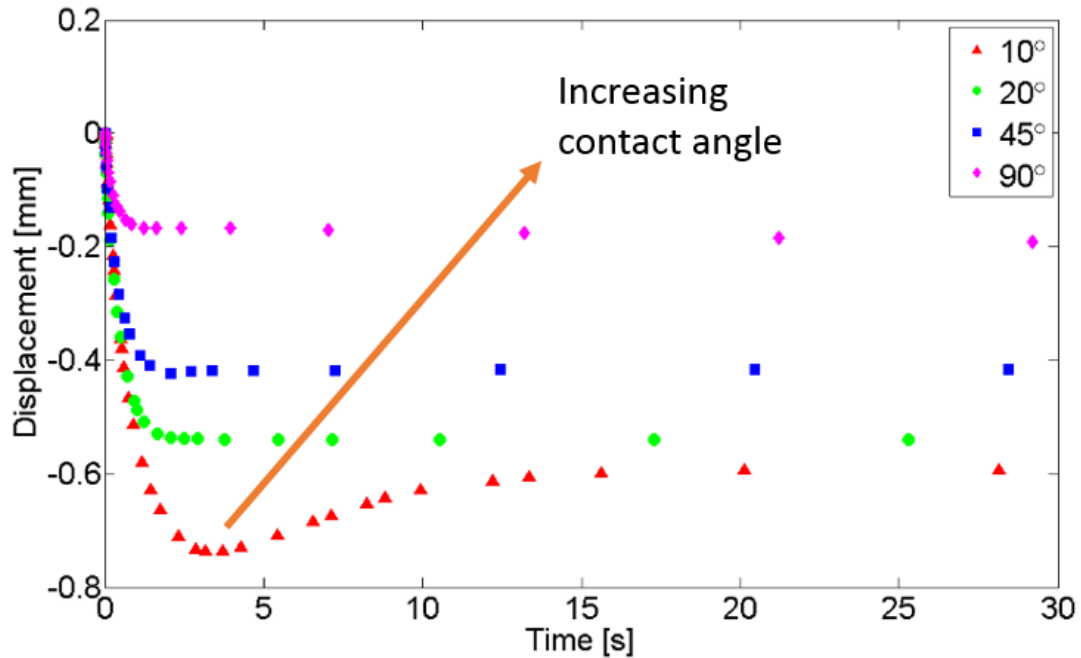
Figure 4.17: Droplet displacement for various contact angles

4.7   Conclusions

Our proposed two-droplet system, which incorporated surface tension gradients, shows significant improvement in the mixing of two miscible liquids. By mixing yellow food color (Tartrazine) in water, as well as aqueous EtOH solutions, an average mixing rate value that was higher by three to four orders of magnitude was obtained when compared to literature values of molecular diffusion alone. However, very little change was observed in the mixing rate of Tartrazine in various EtOH concentrations. This implies that the magnitude of surface tension gradients tested had insignificant impact on the mixing rate between the two liquids.

To better understand our results, we constructed a laminar two-phase flow model using COMSOL, which encompasses a free surface, a contact line, and the Marangoni effect. Our simulations indeed showed the same mixing time for all EtOH concentrations tested. Also, the model showed a significant improvement in mixing time when Marangoni effects were present. This agrees with the comparison made between our experimental values and molecular diffusion coefficients from previous works.

The model also predicts a stark improvement in the time constant at smaller diffusion coefficient values. By studying various contact angles, our simulations showed that a droplet with a higher contact angle requires less time to reach the mixed state. In conclusion, our experimental results, backed by numerical results, confirmed that the presence of Marangoni stress indeed improves the mixing rate of two miscible liquids. The mechanism presented in this work shows an alternative way of achieving an enhanced mixing rate, as compared to only molecular diffusion, without the need for external sources. Potentially, the system can be applied in microfluidics, where the mixing of small-volume droplets is key but remains a challenge.

5 Droplet Actuation in a Hele-Shaw Cell

"Trial often exhibits truly wonderful results." – Chinese proverb

This chapter presents the actuation of a microliter droplet within a Hele-Shaw cell by means of surface tension gradient or Marangoni effect. Compared to a droplet in a trace, as presented in "Chapter 3: Propulsion on an Incline," a droplet deposited within a Hele-Shaw cell is subjected to two contact lines: on the top and the bottom of the droplet.

In this work, a food color droplet is first injected within the gap formed by the parallel plates of the Hele-Shaw cell to produce a cylindrical droplet, followed by a lateral injection of a lower surface tension droplet. The experimental values of distance traveled and velocities arising from the actuation were later used in the analytical framework to estimate the Marangoni and dissipative forces. A numerical model using COMSOL was also built as an alternative approach to estimating the forces. The work presented in this chapter has been accepted for publication by *Acta Mechanica*.

5.1   Introduction

A Hele-Shaw cell is commonly used to model two-phase flow confined within a small gap. The device comprises of two parallel plates separated by a distance much smaller than the characteristic length of the plates, such that the liquid flow in between the plates is laminar. It has been used to model studies in a wide range of areas, namely oil recovery (Paterson, 1981), CO_2 geological storage (Faisal et al., 2015), transport in

capillary blood vessels (Wei et al., 2003), droplets in microfluidics (Shen et al., 2014), semiconductor chip packaging (Guo and Young, 2015), as well as photovoltaic cell production (Dhanabalan et al., 2001).

Experiments with vertical (Faisal et al., 2015; Shad et al., 2009; Sullivan et al., 2014) as well as tilted Hele-Shaw cells have been carried out where, in the latter case, bubbles of various shapes rising in a surrounding liquid were reported. Works pertaining to droplets in a Hele-Shaw cell, to date, typically involve a droplet suspended in an aqueous phase. Amselem et al. (2015) studied the behavior of oil droplets subjected to various flow rates of the surrounding glycerol-water solution. Huerre et al. (2015) correlated the motion of a droplet with the lubrication film between a droplet and a wall. Numerical studies on the morphology of these resulting pancake droplets have been reported by Brun et al. (2013) and Oswald and Poy (2015). Another mode of actuation that has been investigated includes thermocapillary-driven air bubbles or droplets in a Hele-Shaw cell (Bratukhin and Zuev, 1984; Lu et al., 2007).

When a microliter droplet is formed in between the parallel plates without an external flow, it takes on the shape of a cylinder. Though theoretical studies of a cylindrical droplet subjected to an external flow (Lee and Fung, 1969) and a surface tension gradient (Gallaire et al., 2014) have been published, none have reported its experimental observation to the best of our knowledge. Hence, the original contributions of our work are to:

  i.   Demonstrate droplet actuation in a Hele-Shaw cell by the solutal Marangoni effect which occurs when two miscible droplets are juxtaposed in the cell

 ii.   Present a new analytical and numerical methodology to quantify the resultant Marangoni and dissipative forces acting on the droplet

iii.   Estimate the mass transport between the two interacting droplets

The mechanism we present may be a potential alternative to the transport of reagent droplets in enclosed microfluidic devices (Abbyad et al., 2011; Huebner et al., 2009; Song and Ismagilov, 2003). It is important for the devices to be enclosed, particularly when the droplets under test might be hazardous to the user and environment (Yobas et al., 2009). This work is also motivated by the requirements for diagnostic devices for developing countries outlined by the World Health Organization under the acronym ASSURED: Affordable, Sensitive, Specific, User-friendly, Rapid and robust, Equipment-free, and Deliverable to end-users (Martinez et al., 2010). Our proposed method of droplet actuation, which does not rely on external sources of power, eliminates the risk of excessive pressure build up and can be suited for portable devices.

5.2   Experimental Methods

Pre-cleaned plain rectangular microscope glass slides (Thermo Fisher Scientific, Australia) measuring 75 x 25 x 1 mm was used as the parallel plates of our Hele-Shaw cell. A commercial double-sided foam tape of thickness 0.5 mm was used to create the spacing: four square pieces measuring ~ 5 x 5 mm were cut and attached at the four corners to separate the two glass plates. To ensure that the plates were parallel, the injected droplet was observed to confirm that it was stationary. A deviation from parallelism would induce motion, due possibly to contact angle hysteresis (Zhang and Han, 2007). Also, the cell was placed on a glass table that was leveled using a bubble level gauge each time prior to an experiment. Using a glass syringe (Hamilton, USA), a 3 µl droplet of commercial blue food color (Hansells, New Zealand), used as received, was injected perpendicular to the length of the Hele-Shaw cell. Following that, an equal volume of ethanol (EtOH) was injected from a lateral distance ~1.5 mm adjacent to the stationary blue droplet.

A video of the experiment can be viewed at https://youtu.be/HP8WhU1U05w. The experiment was performed in a controlled environment, in which also the cell was assembled: 21 °C +/- 1 °C and 50% humidity. Using a digital single-lens reflex (DSLR) camera (Canon EOS 760D), the experiment was recorded at 50 frames per second. By overlaying a frame chosen for a particular time of interest on top of the frame showing the initial position of the droplet, a measurement line was drawn from the center of one droplet to the other. Based on the pixel-to-actual length scale set on these measurements, the actual length of the line drawn was then obtained. All image processing was performed using Image J (Rasband, 1997).

5.3   Experimental Results and Discussion

For a 3 µl blue food color droplet injected into parallel rectangular plates of length, $l =$ 75 mm, width, $w = 25$ mm, separated by a height, $h = 0.5$ mm, the resulting droplet measured 3.33 mm in diameter, $2R_o$. The stationary droplet formed was circular with concave menisci due to surface tension (see Figure 5.1). The contact angle measured was ~ 45°.
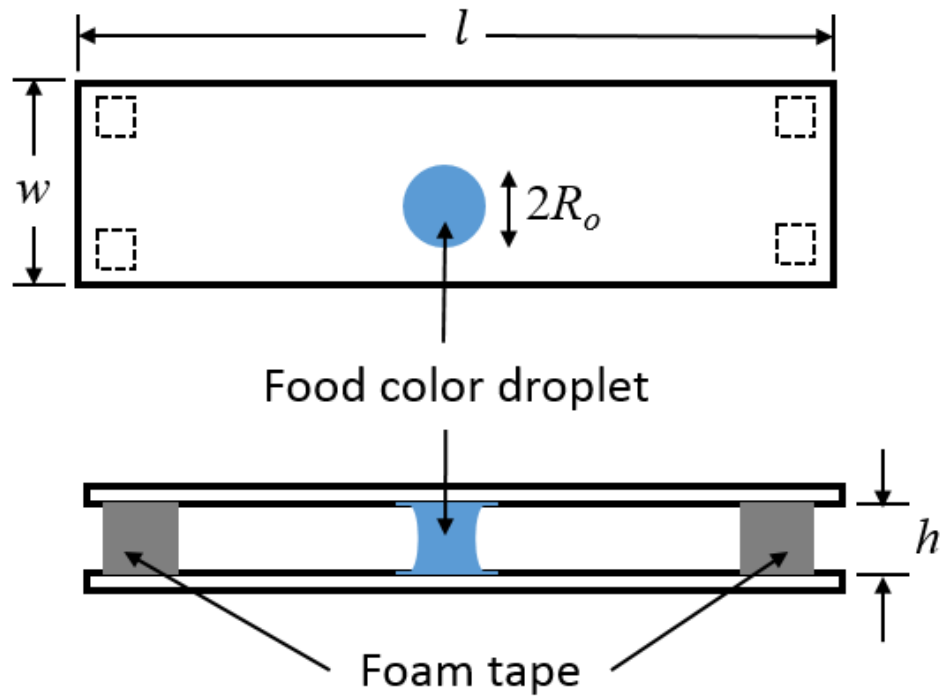
Figure 5.1: An illustration depicting the top view (top) and side view (bottom) of a food color droplet injected in a rectangular Hele-Shaw cell of length *l*, width *w*, and height *h*. Pictures are not drawn to scale

The shape of the blue droplet transitioned from a circle to an ellipse upon the injection of EtOH at $t = 1.8$ s (see Figure 5.2). As the injection of EtOH continued, the blue droplet started moving at an angle ~ 25° from its original position. We attributed the actuation to a decrease in surface tension arising from a limited amount of EtOH vapor dissolving in the blue droplet (Sellier et al., 2013).
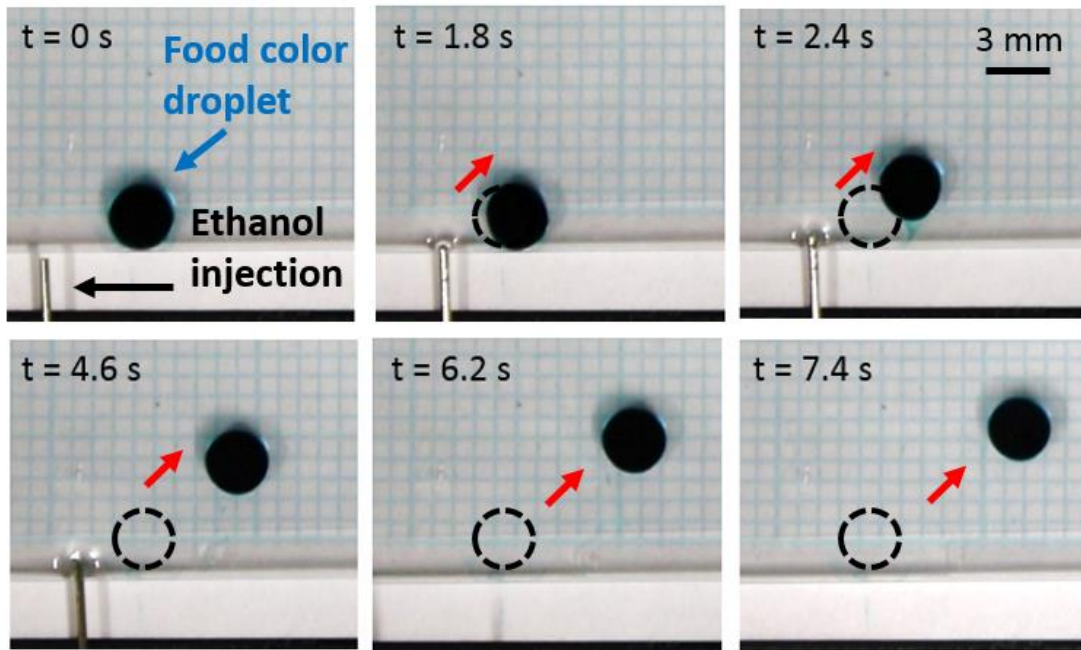
Figure 5.2: Top-down photographs of the trajectory and shape morphology of a blue food color droplet actuated by a droplet of EtOH in a Hele-Shaw cell. Dashed circle denote initial position of droplet, pre-actuation (see video: https://youtu.be/HP8WhU1U05w)

Using Image J, the distance traveled by the blue droplet was measured by taking the center-to-center distance relative to its original position. Figure 5.3 shows the distance traveled by the blue droplet from the beginning until the very instant it stopped moving. The measurements were based on three runs ($n = 3$). On average, the maximum distance traveled was ~18 mm in 36 s.
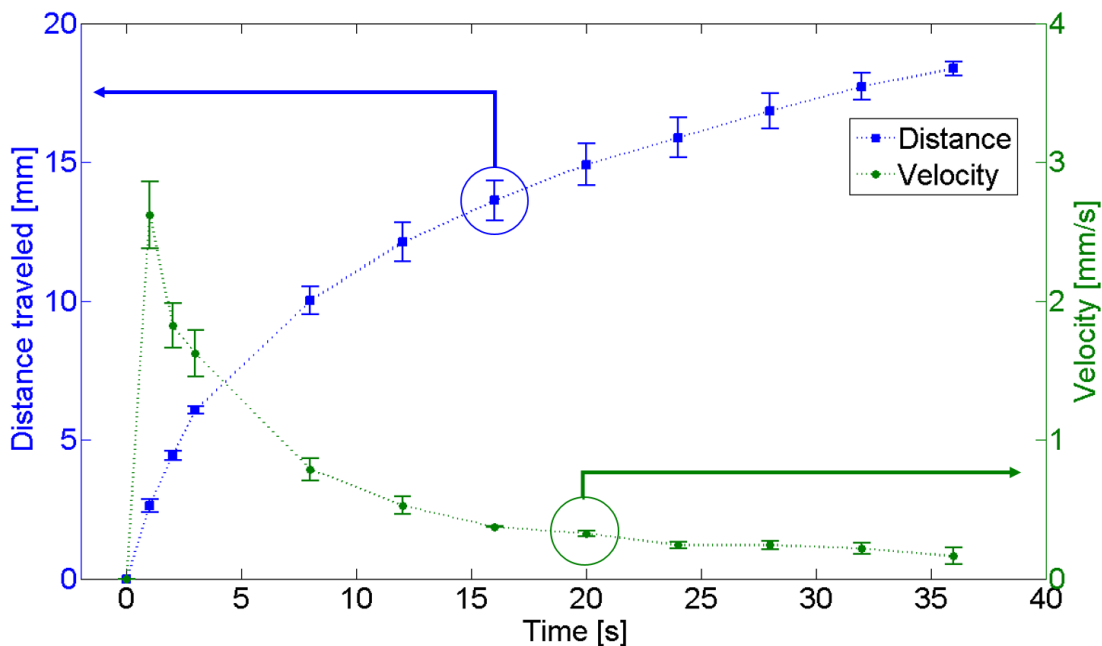
Figure 5.3: Distance traveled and velocity vs. time of a blue food color droplet actuated by an EtOH droplet in a Hele-Shaw cell. Error bars are based on three separate actuations

A similar actuation method has been shown in our previous work, where a 1 μl droplet deposited onto a bottom-only surface patterned with a 1 mm-wide hydrophilic stripe showed a maximum traveled distance of ~ 10 mm (Ng et al., 2016). With a larger volume, hence a larger footprint, in addition to two contact lines, one would expect the droplet in a Hele-Shaw cell to travel less due to higher viscous resistive force. However, our comparison showed that a droplet pinned at the sides travels less. This may suggest that its contact angle hysteresis is smaller compared to the interacting droplet in a Hele-Shaw cell.

Although EtOH was continually injected in the Hele-Shaw cell once the blue droplet had started moving, the velocity of the traveling droplet decreased (see Figure 5.3) as it moved further from the EtOH injection point. The velocity values were obtained

using the difference method. In addition, we found that the system was dominated by surface tension instead of viscous stresses. Using the viscosity of water, μ, velocity values of the traveling droplet, V, and the surface tension of water, σ, the capillary number, $Ca = \mu V/\sigma$ was calculated to be between 6.3 x 10^{-6} to 2.0 x 10^{-5}. It was also evident that the water droplet maintained its circular shape at final equilibrium.

Since the actuation of a droplet in a Hele-Shaw cell has been shown feasible, the next step was to investigate the guided actuation of the droplet along a channel within the cell, as an extension to our previous work of droplet actuation based on solutal Marangoni in an open configuration (Ng et al., 2016). Our first attempt at creating hydrophobic regions was by using a commercial product called Rain-X [®], which is marketed as a rain-repellant for wind shields. Multiple process steps, including oxygen-plasma etching and heat curing, was carried out in order to define the hydrophilic and hydrophobic regions on the microscope glass slides. Our testing showed non-propulsion on the intended hydrophilic stripe. This could imply that plasma-activation and heat curing had changed the surface chemistry of the glass, hence affecting the contact angle of a droplet deposited on the surface.

Our second attempt at creating hydrophobic barriers was much simpler; a channel was created by drawing two parallel lines using a permanent marker, on only one side of a plasma-treated microscope glass slide. This enables the water droplet to be contained within the channel. By placing the tip of a pipette containing EtOH close to the water droplet, without actually dispensing the EtOH droplet onto the glass slide, guided actuation was observed along the channel. This shows that EtOH vapor alone could cause a drop in surface tension gradient, thus resulting in actuation. However, if an EtOH droplet was deposited next to the water droplet, the permanent marker channel within the vicinity started to dissolve. Therefore, the use of a permanent marker to create a channel is only advantageous in creating hydrophobic barriers to contain a water droplet, but not so much in guiding a droplet with a volatile liquid (see video: https://www.youtube.com/watch?v=Tnr_rRopYWE&feature=youtu.be).

5.4 Analytical Model

The motion of a droplet in a Hele-Shaw cell is representative of the force balance between the force arising from surface tension gradient or Marangoni force, F_σ, as well as the viscous resistive force, F_r (see Figure 5.4). From Newton's second law,

$$m\frac{dV}{dt} = F_\sigma - F_r, \tag{5.1}$$

where V is the traveling velocity of the droplet in the x-direction.
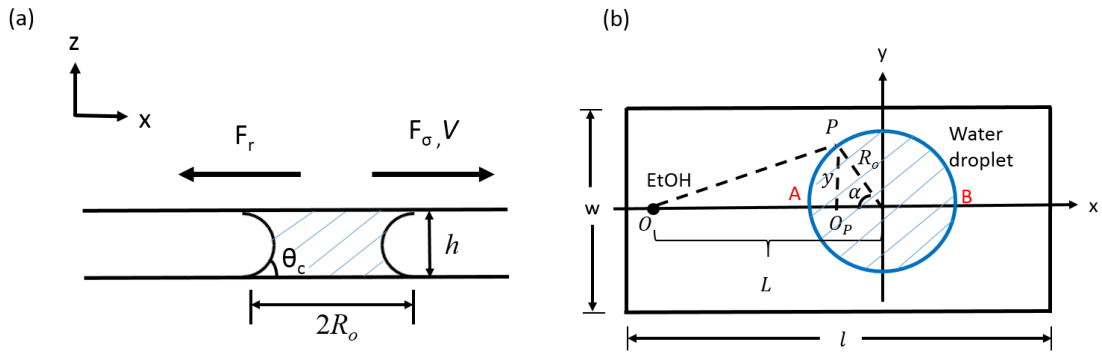
Figure 5.4: An illustration showing the model parameters from (a) the side view and (b) the top view of a food color droplet with diameter $2R_o$ and contact angle θ_c in a rectangular Hele-Shaw cell of length l, width w, and height h. L is the distance between the water droplet and the EtOH source, P is a point at an angle α from the center of the water droplet, and O_p is the vertical distance from P to the x-axis. F_r is the resistive force, F_σ is the Marangoni force, and V is the velocity. Pictures are not drawn to scale

Following the analogy from Ahmed et al. (2014), along with the inclusion of two circular footprints for our droplet in a Hele-Shaw cell, the viscous resistive force, F_r can be expressed as

$$F_r = 2 \int_0^{R_o} \tau_w (2\pi r) \, dr, \tag{5.2}$$

where τ_w is the wall shear stress, given by

$$\tau_w = \frac{6\mu V}{h}. \tag{5.3}$$

R_o represents the radius of the droplet and h the height of the Hele-Shaw gap. The Marangoni force, F_σ can be expressed as a function of angular surface tension, $\sigma(\alpha)$ as follows:

$$F_\sigma = 4R_o \cos\theta_c \int_0^{\pi} \cos\alpha \cdot \sigma(\alpha) \, d\alpha, \tag{5.4}$$

where θ_c represents the equilibrium/Young contact angle. For convenience, we shall assume a trigonometric distribution of the surface tension such that

$$\sigma(\alpha) = \sigma_A + (\sigma_B - \sigma_A) \sin\frac{\alpha}{2}, \tag{5.5}$$

where σ_A is the surface tension at $\alpha = 0°$, and σ_B is the surface tension at $\alpha = 180°$. Therefore, solving Eq. (5.4) by substitution of Eq. (5.5) yields

$$F_\sigma = \frac{8}{3} R_o \cos\theta_c \, (\sigma_B - \sigma_A). \tag{5.6}$$

In addition, the concentration of EtOH vapor in air can be modeled using the diffusion of an EtOH point source in two-dimension theory. The pertinent equation is given by

$$C(x, y, t) = \frac{M}{4\pi hDt} e^{-\frac{(x^2 + y^2)}{4Dt}},$$

(5.7)

where a uniform diffusion coefficient, D was assumed. M represents the mass of ethanol and h, the height of the cell gap is included to depict a three-dimensional case. A schematic of an EtOH point source relative to a water droplet in a Hele-Shaw cell is illustrated in Fig. 5.4(b). The distance from the EtOH point source, O to an angular position P, α degrees from the x-axis, is expressed as

$$\overrightarrow{OP} = \overrightarrow{OO_P} + \overrightarrow{O_P P}$$

(5.8)

which, upon further expansion becomes

$$\overrightarrow{OP} = (L - R_o \cos \alpha)\vec{x} + R_o \sin \alpha \vec{y},$$

(5.9)

where L is the center-to-center distance between the EtOH point source and the water droplet, and R_o the radius of the water droplet. Substituting the expression in Eq. (5.9) into Eq. (5.7), an expression for the angular EtOH vapor concentration is obtained:

$$C(L, R_o, \alpha, t) = \frac{M}{4\pi hDt} e^{-\frac{(L^2 + 2R_o^2 - 2LR_o \cos \alpha)}{4Dt}}.$$

(5.10)

5.5   Analytical Results and Discussion

Using experimental values in Eq. (5.1) to Eq. (5.3), the forces acting upon the droplet were calculated and depicted in the graphs shown in Figure 5.5. Again, the difference method was used to obtain the acceleration for Figure 5.5(a).
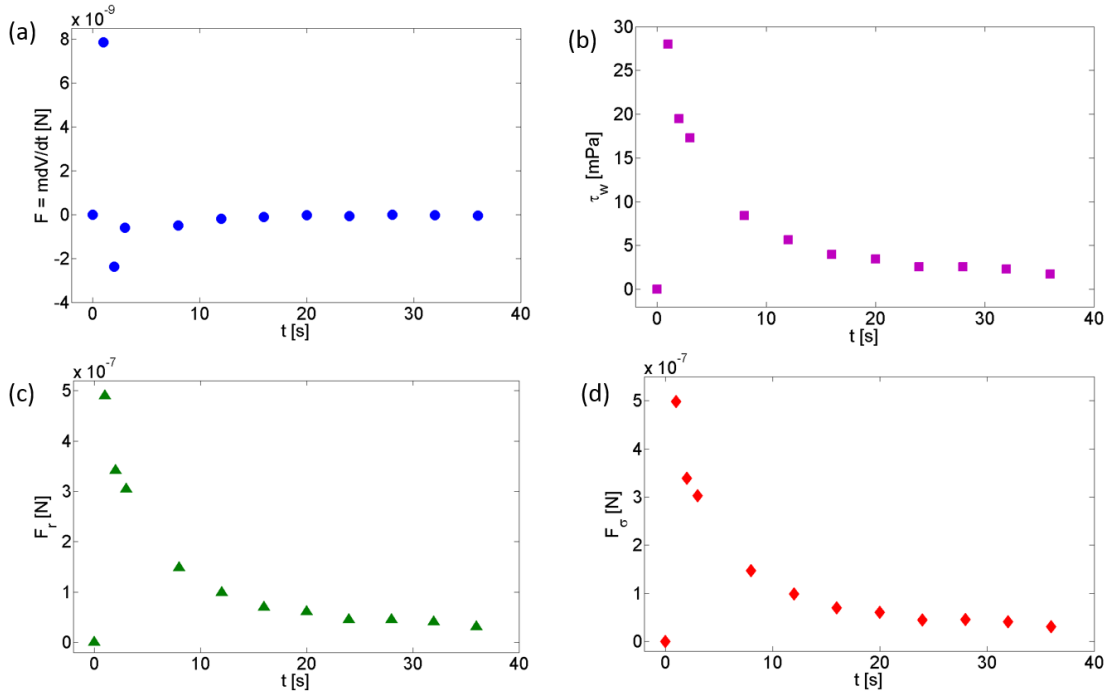
Figure 5.5: Analytical values of forces acting upon a droplet in a Hele-Shaw cell: (a) force as a result of traveling velocity, $F = mdV/dt$, (b) wall shear stress, τ_w, (c) viscous resistive force, F_r, and (d) Marangoni force, F_σ

As a result of decreasing velocity that eventually reaches zero when motion stops, the forces acting upon the droplet, as expected, tend to zero as time progresses. At $t = 1$ s, the Marangoni force, F_σ exceeds the viscous resistive force, F_r by only 8.0×10^{-9} N (see Figure 5.5). Nevertheless, this magnitude resulted in the actuation of the droplet, with a distance ~ 2.6 mm (see Figure 5.3). The concentration of EtOH at positions A

and B, as shown in Fig. 5.4(b), was then analyzed. Using $M = 2.37 \times 10^{-6}$ kg for the mass of a 3 μl EtOH, $D = 10^{-6}$ m²/s for the typical diffusion constant value for the vapor of a volatile liquid (Sultan et al., 2005) and L the experimental traveled distance, C_A and C_B were calculated by substituting $\alpha = 0$ and $\alpha = \pi$, respectively in Eq. (5.10). A distribution of EtOH vapor concentration on two opposing sides of the droplet as a function of time was obtained, as shown in Figure 5.6. C_A was the highest initially and decays over time. Closer analysis showed similar trends for C_B and C_A. Also, the range for C_B is only ~ 5.84×10^{-7} g/mm³, while the range for C_A is two orders of magnitude higher, ~ 1.68×10^{-5} g/mm³. The initial rate of change of C_A is much higher than that of C_B, but over time $(C_A - C_B)$ becomes smaller, suggesting a trend towards a uniform concentration.
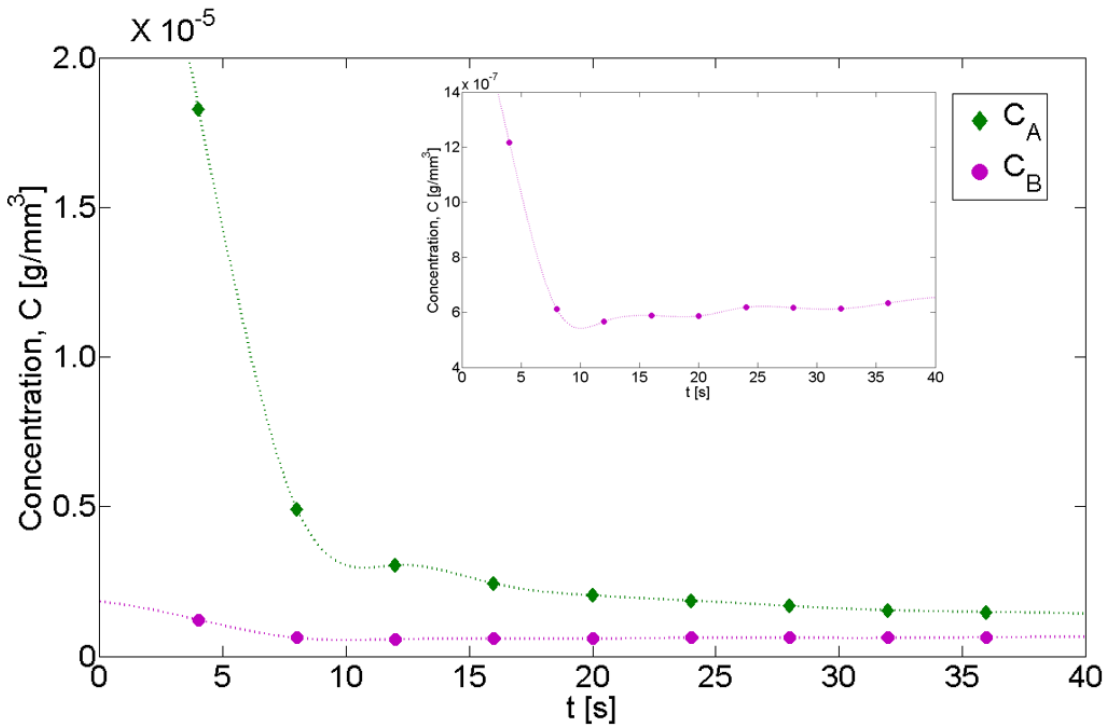
Figure 5.6: Distribution of EtOH concentration on two opposing sides of the droplet in a Hele-Shaw cell as a function of time. Inset shows a close-up of C_B to show its trend

5.6 Numerical Model

The objective of this numerical model is not to directly model the experiment, but rather, to obtain the viscous resistance force, F_r in order to estimate the Marangoni force, F_σ. First, a constant body force was imposed to obtain the terminal velocity. At the terminal velocity, the body force equals the viscous resistive force (Bico and Quéré, 2001), thus allowing for the calculation of the viscous resistive force. Using various body force values, a relationship between viscous resistive force and terminal velocity is obtained. Therefore, the viscous resistive forces corresponding to experimental velocities can be obtained and subsequently used to calculate the Marangoni force, F_σ. A similar methodology has been reported by Karpitschka et al. (2016), where the interaction force between two droplets sliding down a soft solid due to gravitational force was determined from their relative velocities.

To model a droplet in a Hele-Shaw cell, a half-cylinder was first constructed according to the dimensions of the droplet measured, detailed in sub-section 5.3. A half-cylinder with symmetry imposed on the center cross-section parallel to the xz-plane (see Figure 5.7) was modeled instead of a full cylinder to save computational time.
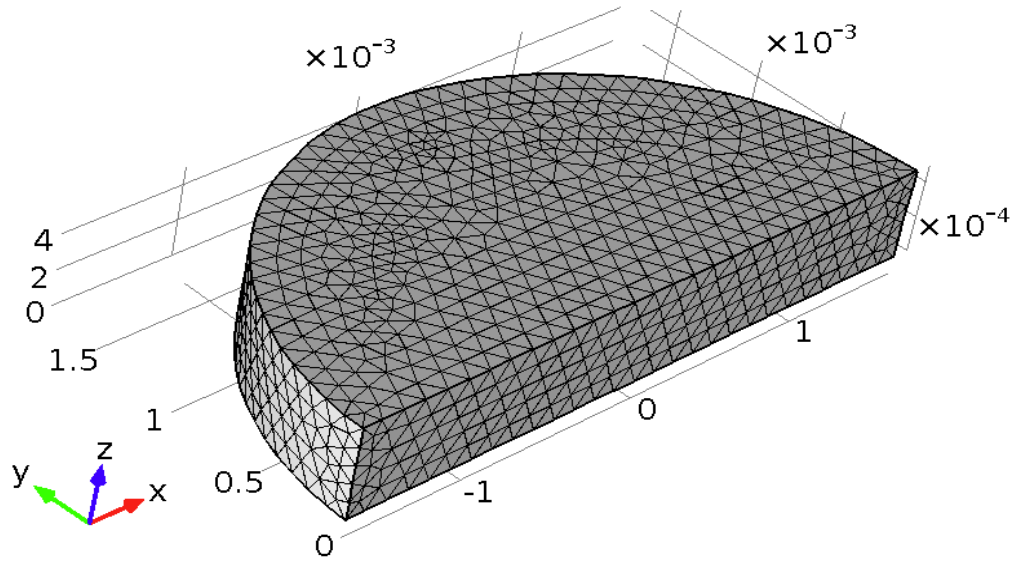
Figure 5.7: Half-cylinder model of a droplet in a Hele-Shaw cell

Using the *Laminar Two-Phase Flow Moving Mesh Physics* in COMSOL, the velocity field **u** is solved through the following Navier-Stokes equation:

$$\rho \frac{\partial \mathbf{u}}{\partial t} + \rho(\mathbf{u} \cdot \nabla)\mathbf{u} = \nabla \cdot [-p\mathbf{I} + \mu(\nabla \mathbf{u} + (\nabla \mathbf{u})^T)] + \mathbf{F}, \qquad (5.11)$$

and

$$\nabla \cdot \mathbf{u} = 0, \qquad (5.12)$$

where μ is the dynamic viscosity and $\mathbf{F}$ is a body force imposed in the *x*-direction. The momentum equation as shown in Eq. (5.11) is a non-linear convection-diffusion equation that would be unstable if discretized using the Galerkin finite element method. As such, streamline diffusion was included for stabilization, where diffusion is added only in the streamline direction and less numerical diffusion was given when the

104

numerical solution is closer to the exact solution. In addition, isotropic diffusion with a default tuning parameter, $\delta_{id} = 0.25$ was included to dampen the effects of oscillations. Boundary conditions include a contact angle at the wall-fluid interface, defined by a value of 45°, as well as a slip condition at the liquid-solid interface. To model the solid walls on the top and bottom of the droplet, a boundary condition that specifies frictional force between the liquid-solid interface was imposed:

$$\boldsymbol{F}_{fr} = -\frac{\mu}{\beta}\mathbf{u}, \tag{5.13}$$

where $\beta = 0.2 * m$ represents the Navier slip length for a mesh element size of m (COMSOL Multiphysics, 2015). The kinematic boundary condition at the free surface is given by

$$F(x, y, t) = h(x, t) - y. \tag{5.14}$$

The half-cylinder model built was discretized to 20,788 domain elements, 2404 boundary elements and 159 edge elements. Winslow smoothing was chosen such that the mesh was smoothly deformed given the boundary conditions. Linear P1 elements were chosen for both the velocity and pressure components. The air-liquid interface was modeled under the *External Fluid Interface* node through the following equation:

$$\mathbf{n}\cdot\mathbf{T} = -p_{ext}\mathbf{n} + \sigma(\nabla_t \cdot \mathbf{n})\mathbf{n} - \nabla_t\sigma, \tag{5.15}$$

where $\mathbf{n}$ is the normal to the interface, $\mathbf{T}$ is the stress tensor, ∇_t is the surface gradient, and $\nabla_t\cdot\mathbf{n}$ is the surface divergence of the normal vector. The external pressure, p_{ext} was set to 0. To represent the surface tension of water, σ was specified as 0.072 N/m.

5.7 Numerical Results and Discussion

In order to estimate the viscous resistive force, F_r, body force or $\boldsymbol{F}$ values of 1, 10, 100, 400, 1000, 3000, 5000, 8000 and 10000 N/m^3 imposed in the x-direction were used to solve Eq. (5.11). Our simulations showed that the velocity eventually saturates as a result of balanced viscous resistive force and body force in the drop and at the contact lines. Therefore, at the terminal velocity, the viscous resistive force equals the body force. A relationship between the viscous resistive force and velocity was then attained (see Figure 5.8).
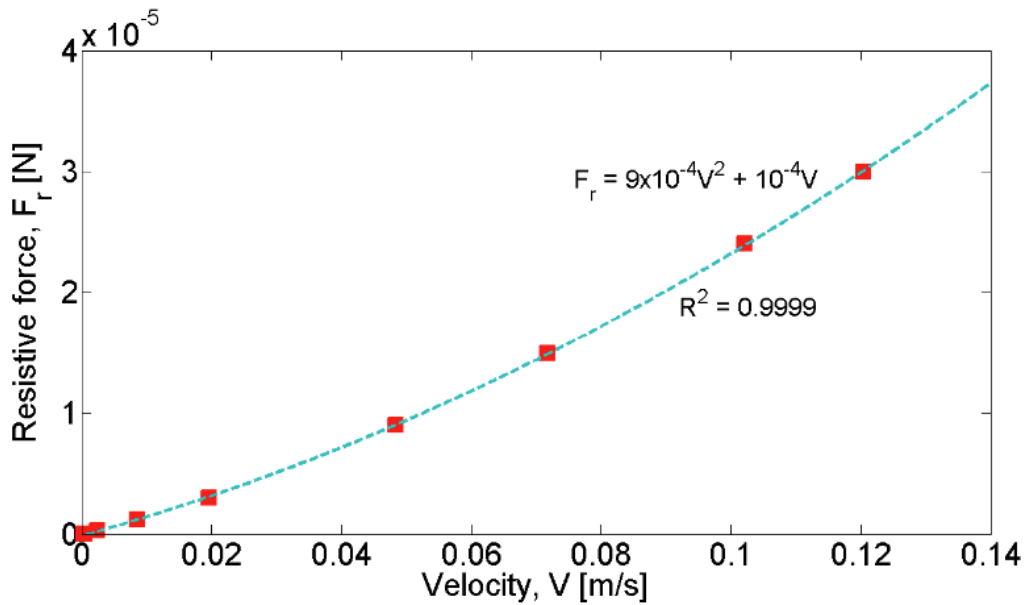
Figure 5.8: Relationship between viscous resistive force and velocity attained numerically

Through a quadratic fit, the viscous resistive force is approximated as

$$F_r = 9 \times 10^{-4}V^2 + 10^{-4}V. \tag{5.16}$$

106

The fact that it follows a quadratic relationship, rather than a linear relationship as given by Eq. (5.2), could be attributed to the dissipation at the meniscus and contact lines, which were accounted for numerically but not analytically. Using experimental values of velocity, F_r can now be calculated and substituted in Eq. (5.1) to obtain the Marangoni force, F_σ. The multipliers 9×10^{-4} and 10^{-4} in Eq. (5.16) contain units of kg/m and kg/s respectively. The trend for F_σ attained analytically and numerically are similar; however, the values at initial times do not match closely (see Figure 5.9). This could be attributed to the dissipation at the contact lines and menisci captured numerically, but was not accounted for analytically. Nevertheless, the discrepancy between numerical and analytical values is small, with an average delta of 6.97×10^{-8} N. This value corresponds to the dissipation at the menisci.
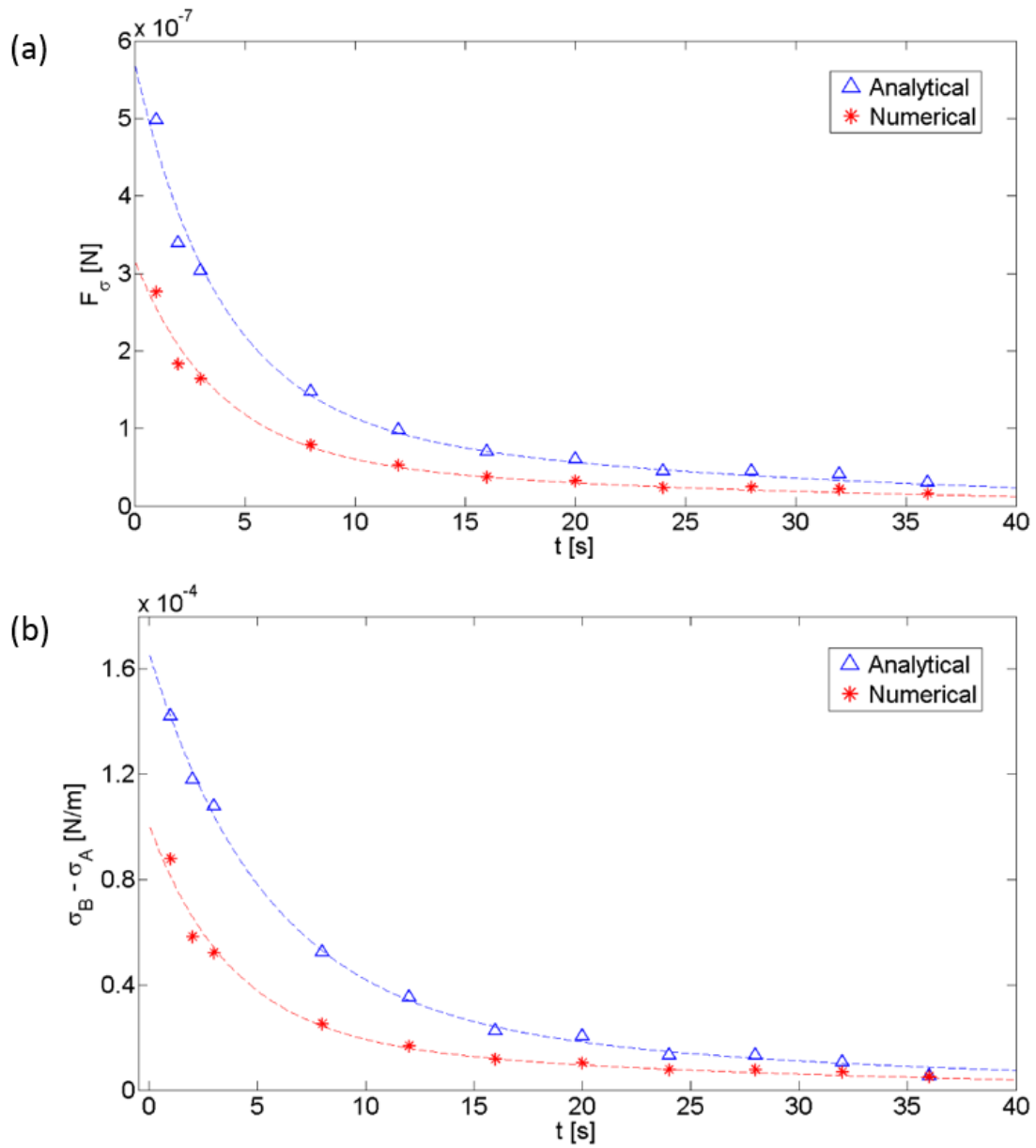
Figure 5.9: Comparison of analytical and numerical values of (a) Marangoni force, F_σ and (b) surface tension difference obtained based on F_σ

Another quantity of interest is the surface tension difference between point B and point A, as shown in Figure 5.4(b). Rearranging Eq. (5.6), we obtain:

$$(\sigma_B - \sigma_A) = \frac{3}{8} \frac{F_\sigma}{R_o \cos \theta_c}. \tag{5.17}$$

Using the analytical and numerical values of F_σ (see Figure 5.9 (a)) in Eq. (5.17), a surface tension difference profile, as shown in Figure 5.9(b), was obtained. The initial value at $t = 1$ s indicates that only a small surface tension difference, i.e. 1.4×10^{-4} N/m (numerical) or 8.8×10^{-5} N/m (analytical) is required to induce motion. In addition, the surface tension of a water-ethanol mixture can be calculated using the following correlation (Vazquez et al., 1995):

$$\frac{\sigma_w - \sigma(c)}{\sigma_w - \sigma_e} = \frac{1 + a(1 - c)}{1 - b(1 - c)} c, \tag{5.18}$$

where the surface tension of water, σ_w and of EtOH, σ_e are 0.072 N/m and 0.022 N/m, respectively, $(a,b) = (0.917, 0.956)$ are constants and c is the mole fraction of ethanol in the mixture. First, we assume that the droplet is purely water at point B, the point farthest from the EtOH source. As such, there is no EtOH at point B. At $t = 1$ s, the Marangoni force, F_σ is maximum with a value of 2.76×10^{-7} N/m attained numerically. By using the maximum F_σ and $\sigma_B = 0.072$ N/m. in Eq. (5.17), we obtain $\sigma_A = 0.071912$ N/m. Next, by substituting the calculated σ_A into $\sigma(c)$ of Eq. (5.18), we obtain an EtOH mole fraction value, c of 6.53×10^{-5}. This means that at $t = 1$ s, the mixture contains 0.0065% EtOH, a very small amount, but sufficient to cause an actuation distance of ~ 2.6 mm (see Figure 5.3) as a result of surface tension gradient.

From the surface tension difference values, $(\sigma_B - \sigma_A)$ in Figure 5.9(b), the angular surface tension values, $\sigma(\alpha)$ can now be obtained through Eq. (5.5). Again, by assuming that the droplet is purely water at point B ($\sigma_B = 0.072$ N/m), σ_A is calculated.

The distribution of angular surface tension attained numerically is as shown in Figure 5.10.
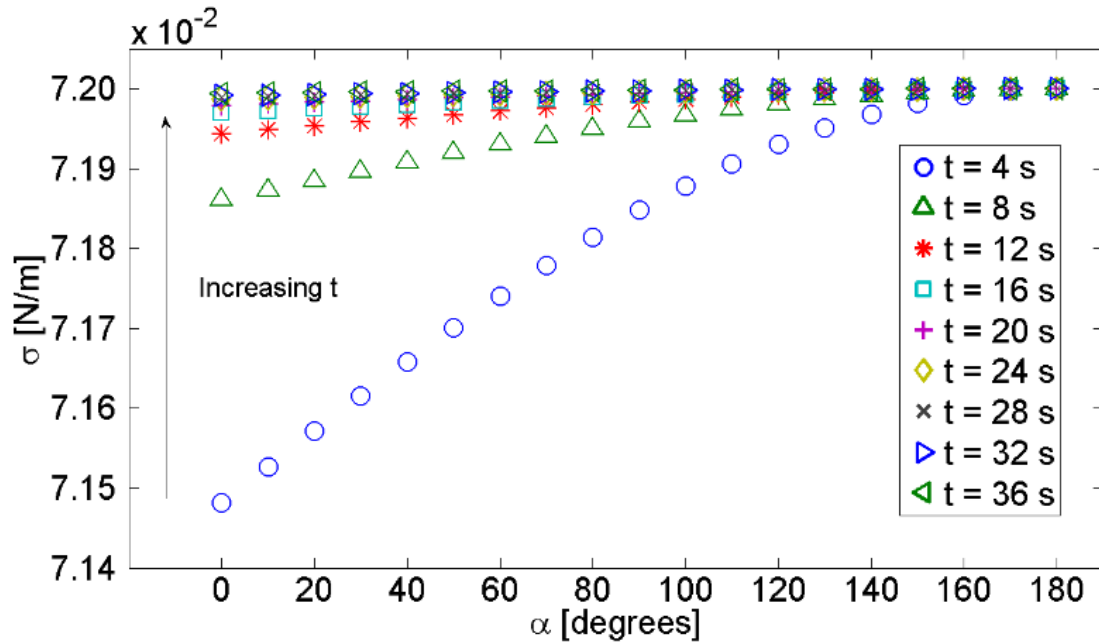
Figure 5.10: Angular surface tension distribution attained numerically

It is interesting to note that at $t = 4$ s, the point closest to the EtOH point source at $\alpha = 0$ is hardly affected by the EtOH vapor, as evident from the surface tension value that was closer to that of water. Nevertheless, propulsion had still occurred. Further analysis shows that the surface tension increases at a given angular position α, albeit very slightly, as the droplet moves further away from the EtOH point source over time (see Figure 5.10). Similarly, the surface tension increases with angular position, but less so beyond $t = 12$ s.

5.8   Conclusions

Through surface tension gradient, the actuation of a food color droplet with both top and bottom contact lines in a Hele-Shaw cell has been successfully demonstrated. By introducing an ethanol droplet next to the cylindrical food color droplet, a maximum traveled distance of ~ 18 mm in 36 s was observed. To the best of our knowledge, none have reported a mechanism for droplet actuation in a Hele-Shaw cell as described in this chapter.

Another contribution of this work is in the calculation of the Marangoni force, which could be identified by generating a curve relating the viscous dissipation force to the droplet velocity. Marangoni force values that compare well against values attained analytically were obtained, thus confirming the validity of the numerical approach. Mathematical analysis showed that only a small surface tension difference, between 8.8×10^{-5} N/m to 1.4×10^{-4} N/m, is required to trigger droplet motion. This may suggest that the actuation mechanism described in this work can be achieved using a wide range of volatile liquids. The results suggest that only a small amount of EtOH actually crosses the droplet free surface to lower its surface tension. Also, we showed that the surface tension of the droplet increases, both with time and angular position, upon interaction with EtOH vapor.

6 Liquid Slug in a Capillary Tube

"Things should be made as simple as possible - but no simpler." – Albert Einstein

This chapter is different from preceding chapters in that, instead of performing a new experiment, we only developed a slug model in COMSOL based on the experimental parameters previously reported by Sellier et al. (2017) in their work pertaining to the spontaneous motion of a slug of miscible liquids in a capillary tube. The numerical model was built not to model the experiment, but rather, to estimate the viscous forces of a slug subjected to different body force values, so that the Marangoni force values can be calculated. These values are then compared to the analytical approach through a formula previously derived for the viscous force relating to a slug in a capillary tube. A second dimensionless model is built to study the effects of the Reynolds and Peclet numbers on the mixing time when a concentration gradient is introduced in the slug.

6.1   Introduction

In a typical laboratory, one can often see a scientist handling tubes or vials for liquid samples preparation or analysis. Though appropriate in a research environment, a much robust system that can handle more tests in a shorter time is required for commercial diagnostic devices. As such, miniature medical devices have been tested and developed. These days, microtubes are used to conduct biological processes, such as reactions pertaining to reverse-transcription and amplification of RNAs and DNAs (Bontoux et al., 2008). Another example is the lab-in-a-tube (LIAT) device developed by Cobas (Cobas® Liat System), which accomplishes sample preparation, amplification and detection all in one integrated tube device. Often times, these devices rely on peristaltic pumps or internal actuators to displace liquid, which becomes an

issue when portability is important, since an external power source is required either to power or to charge the system.

Based on placing two miscible liquids of differing surface tensions adjacent to each other inside a capillary tube, Sellier et al. (2017) has shown the feasibility of a liquid slug moving within a tube until both liquids have mixed homogeneously, at which the motion eventually stops as a result of surface energy equilibrium. A similar work has been performed by Bico and Quéré (2000, 2002) both experimentally and mathematically, but using two immiscible liquids. Bretherton (1961) and Hodges et al. (2004) has shown the motion of a bubble and liquid, respectively, but in a capillary tube pre-filled with a liquid.

6.2   Experimental Methods

As in the experiment performed by Sellier et al. (2017), a slug of distilled water was drawn up into a glass tube of radius $R = 0.675$ mm through capillary action by dipping the tube into a container of distilled water. Using a micropipette, a slug of ethanol (EtOH) was then injected adjacent to the water slug on the side closest to the tube opening. A video of the experiment can be viewed at: http://youtu.be/KVr2dtvvAGU.

6.3   Experimental Results and Discussion

This sub-section re-iterates the results reported by Sellier et al. (2017). The lengths of the water and EtOH slugs, l_w and l_e, measured 18.5 mm and 1.0 mm respectively. Upon EtOH injection, the water slug moved to the right, in the direction of higher surface tension, away from EtOH. The left and right edges of the water slug, x_a and x_b were monitored throughout motion and recorded through the aid of a ruler placed underneath the horizontally-placed capillary tube.

Figure 6.1(a) shows the position of the edges of the traveling slug as a function of time. The corresponding velocities, obtained using the difference method, are as shown in Figure 6.1(b). The water slug traveled to a maximum distance of ~ 17 mm in 400 s. The highest velocity recorded was 1.0×10^{-3} m/s at $t = 7.5$ s, and gradually decreases thereafter.
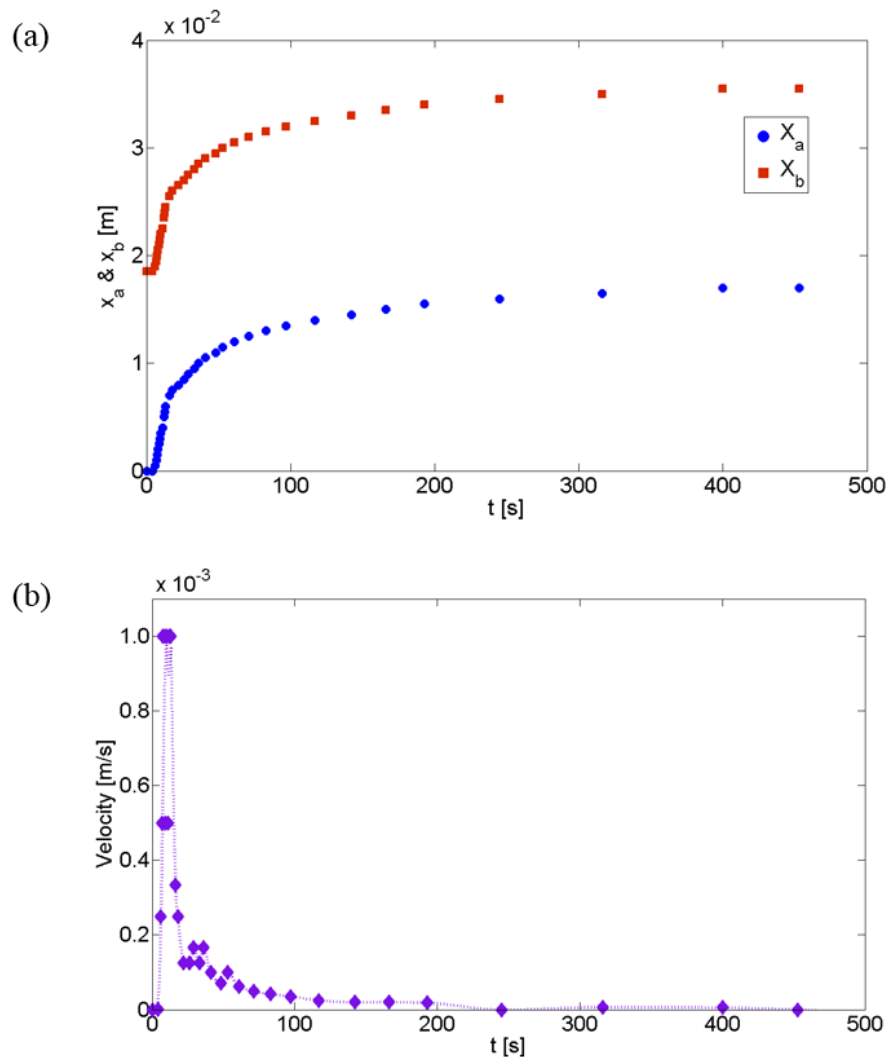
Figure 6.1: The traveling slug in terms of (a) edge positions, x_a and x_b, and (b) velocity [adapted from Sellier et al. (2017)]

6.4   Analytical Model

The balance of forces for a slug in a capillary tube has been well-documented by Sellier et al. (2017). With reference to Figure 6.2, their analysis resulted in expressions for

(a)   the net axial surface tension force applied on the perimeter of the capillary tube, $2\pi R(\sigma_a \cos \theta_a - \sigma_r \cos \theta_r)$, where σ_a and σ_r are the surface tensions corresponding to the advancing and receding contact angles, θ_a and θ_r,

(b)   the viscous force from the shear stress developed at the capillary tube walls, $8V(\mu_w l_w + \mu_e l_e)\pi$, with V the velocity, μ_w and μ_e the viscosities of water and EtOH, and l_w and l_e the lengths of the water and EtOH slugs, and

(c)   the net viscous dissipation term at the moving contact, $2\pi R\left(\frac{3\mu_e V\Gamma}{\theta_r} + \frac{3\mu_w V\Gamma}{\theta_a}\right)$, where Γ represents the natural logarithm of the macroscopic and molecular length scales.
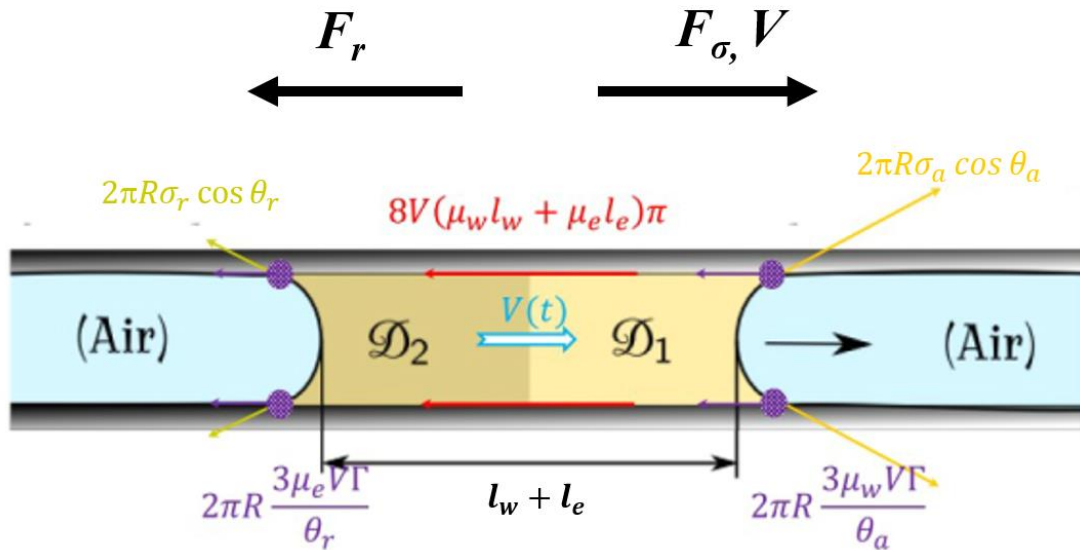
Figure 6.2: A schematic showing the forces acting on a slug in a capillary tube [adapted from Sellier et al. (2017)]

6.5 Analytical Results and Discussion

From Newton's second law of motion,

$$m\frac{dV}{dt} = F_\sigma - F_r, \tag{6.1}$$

where F_σ is the Marangoni force that arises from surface tension gradient, and F_r is the viscous resistive force. Since our aim is to calculate F_σ, we would need to first calculate F_r. From the derived expression for the viscous force from the shear stress developed at the capillary tube walls, $8V(\mu_w l_w + \mu_e l_e)\pi$, we used the experimental velocity values along with $\mu_w = 8.9 \times 10^{-4}$ Pa·s and $\mu_e = 1.095 \times 10^{-3}$ Pa·s to obtain the resistive force, F_r as a function of time.
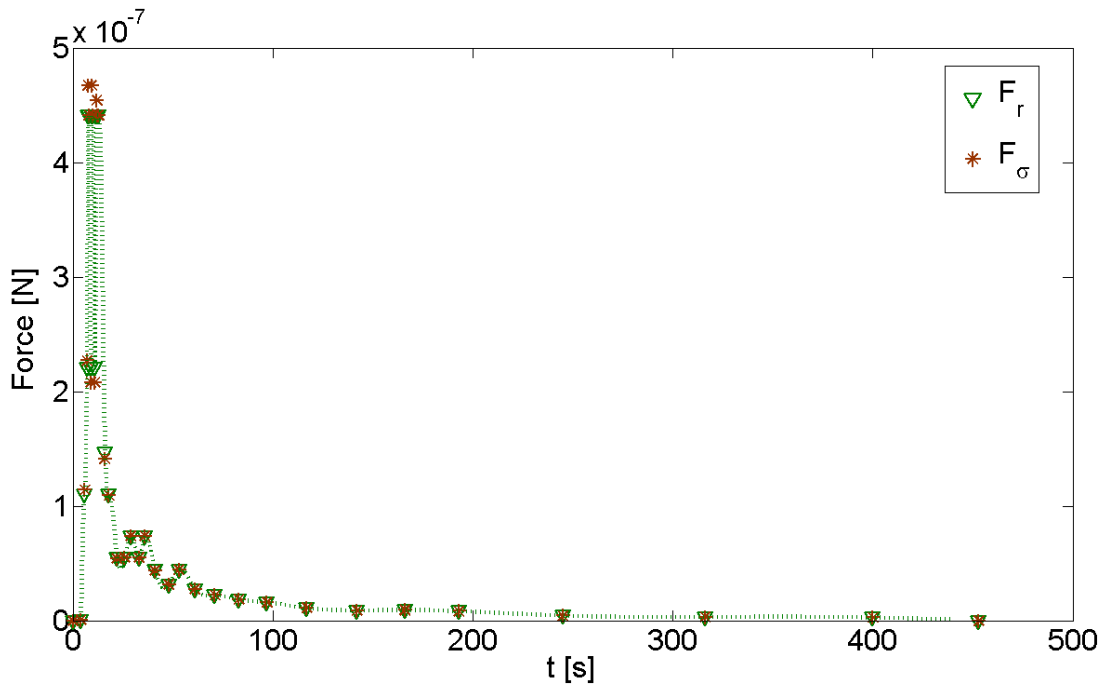
Figure 6.3: The resistive force, F_r and Marangoni force, F_σ obtained analytically

The Marangoni force, F_σ can now be calculated using Eq. (6.1), with $m = 2.58 \times 10^{-5}$ kg, determined from the density of water, 1000 kg/m^3 and the calculated volume of the water slug assuming a cylindrical geometry, 2.58×10^{-8} m^3. Our analysis shows that F_σ and F_r did not differ by much, and that at the start of motion, F_σ had only exceeded F_r by 3.21×10^{-9} N (see Figure 6.3).

The surface tension gradient between the right and left edges of the slug, denoted by $\sigma_a - \sigma_r$ is then analyzed. With the assumption of negligible difference between the advancing and receding contact angles, an equilibrium contact angle, θ_e is substituted in the expression derived for the net surface tension force applied on the perimeter of the capillary tube, to yield

$$F_\sigma = 2\pi R \cos\theta_e \, (\sigma_a - \sigma_r). \qquad (6.2)$$

Therefore, the surface tension gradient between the right and left edges of the slug, $\sigma_a - \sigma_r$ can now be calculated using the measured equilibrium contact angle value, θ_e of 30 degrees, and F_σ values (see Figure 6.3). The distribution of $\sigma_a - \sigma_r$ as a function of time is as shown in Figure 6.4. Our calculations show that only a small surface tension gradient, 3.5×10^{-5} N/m is required to trigger motion.
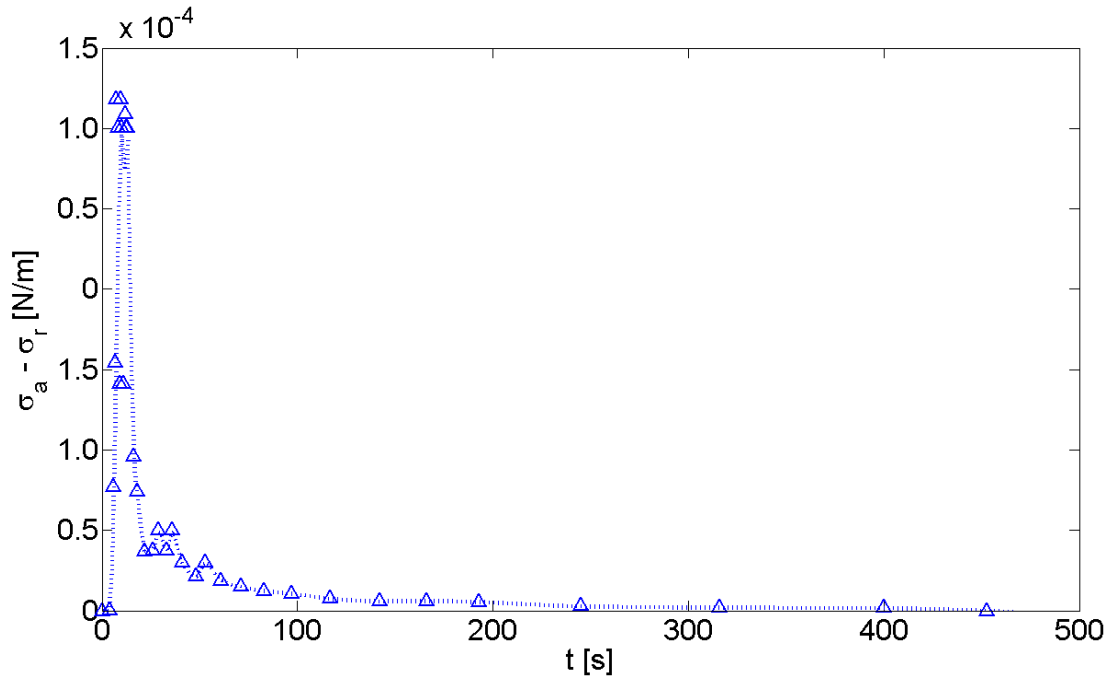
Figure 6.4: Surface tension gradient between the right and left edges of the slug

6.6 Numerical Model

Two numerical models were built in COMSOL: two-phase flow moving mesh model and single phase flow model. The former allowed for the study of terminal velocity as a result of various body forces while the latter enabled a moving wall velocity setting that allowed for the study of mixing time, given an initial concentration distribution.

6.6.1 Two-Phase Flow Moving Mesh Model

Using the 2-D axisymmetric component, only one section of the water slug was modeled, with symmetry imposed in the center cross-section along the z-axis (see Figure 6.5). Here, COMSOL models the volumetric slug by rotating the 2-D plane

118

around the symmetry axis. The dimensions used are slug length, $l_w = 18.5 \times 10^{-3}$ m and tube radius, $R = 0.675 \times 10^{-3}$ m.
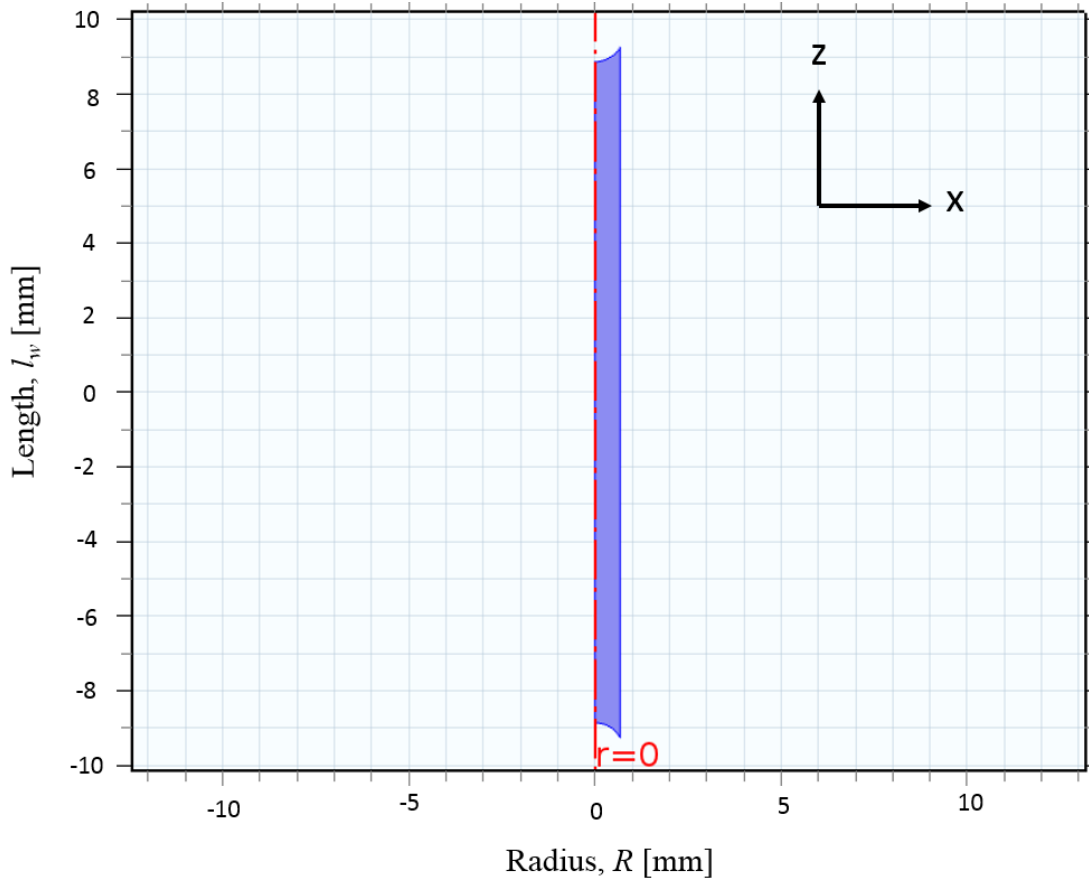
Figure 6.5: COMSOL model of the water slug with symmetry imposed along the z-axis

To model the meniscus at the ends of the slug, the middle rectangle was intersected with two circles at both the top and bottom ends, to yield the experimental contact angle, $\theta_e = 30°$. The calculations for the derivation of the meniscus is presented in Appendix C.

Since our aim is to estimate the resistive forces when the slug is subjected to various magnitudes of body force, the *Laminar Two-Phase Flow Moving Mesh Physics* was used to solve for the velocity field **u**, with the addition of axial body force values F imposed in the *z*-direction, in the following Navier-Stokes equation:

$$\frac{\partial \mathbf{u}}{\partial t} + \rho(\mathbf{u}\cdot\nabla)\mathbf{u} = \nabla\cdot[-p\mathbf{I} + \mu(\nabla\mathbf{u} + (\nabla\mathbf{u})^T)] + \boldsymbol{F},$$ (6.3)

and

$$\nabla\cdot\mathbf{u} = 0,$$ (6.4)

where μ is the dynamic viscosity. Streamline and crosswind diffusions were included for stabilization, since the momentum equation shown in Eq. (6.4) is a non-linear convection-diffusion equation that would be unstable if discretized using the Galerkin finite element method. Isotropic diffusion with a default tuning parameter, $\delta_{id} = 0.75$ was included to dampen the effects of oscillations. Linear P1 elements were chosen for both the velocity and pressure components. The kinematic boundary condition at the free surface is given by

$$F(x, z, t) = h(x, t) - z.$$ (6.5)

The slug model built was discretized to 9186 domain elements and 648 boundary elements. Winslow smoothing was chosen such that the mesh is smoothly deformed given the boundary conditions. The air-liquid interface was modeled under the *External Fluid Interface* node through the following equation:

$$\mathbf{n}\cdot\mathbf{T} = -p_{ext}\mathbf{n} + \sigma(\nabla_t\cdot\mathbf{n})\mathbf{n} - \nabla_t\sigma, \tag{6.6}$$

where $\mathbf{n}$ is the normal to the interface, $\mathbf{T}$ is the stress tensor, ∇_t is the surface gradient, and $\nabla_t\cdot\mathbf{n}$ is the surface divergence of the normal vector. For the initial conditions, the external pressure, p_{ext} was set to 0 and the surface tension, σ was specified as 0.072 N/m to represent the surface tension of water.

6.6.2 Single Phase Flow Model

To simplify the study of mixing time, the *Single Phase Flow Physics* was used in a 2-D axisymmetric slug model (geometry as shown in Figure 6.5), along with the definition of a concentration gradient. This model solves for the velocity and pressure fields based on the Navier-Stokes equation. To make the equation dimensionless, we first define the *x*-momentum Navier-Stokes equation for an incompressible Newtonian fluid as:

$$\rho\left(\frac{\partial u}{\partial t} + u\frac{\partial u}{\partial x} + w\frac{\partial u}{\partial z}\right) = -\frac{\partial p}{\partial x} + \mu\left(\frac{\partial^2 u}{\partial x^2} + \frac{\partial^2 u}{\partial z^2}\right). \tag{6.7}$$

This equation was made dimensionless using the following scalings

$$\tilde{x} = \frac{x}{R_0}, \tilde{z} = \frac{z}{R_0}, \tilde{u} = \frac{u}{V_0}, \tilde{w} = \frac{w}{V_0}, \tilde{t} = \frac{t}{T_0} \text{ and } \tilde{p} = \frac{p}{P_0}, \tag{6.8}$$

where R_o is the radius of the capillary tube, and V_o the wall velocity. Imposing a wall velocity allowed for the study of the droplet in a moving reference frame that moves with the droplet. The time and pressure scales are defined as $T_o = \frac{R_o}{V_o}$ and $P_o = \rho V_o^2$,

121

where ρ represents the density of water. Therefore, the dimensionless form of Eq. (6.7) can be written as:

$$\left(\frac{\partial \tilde{u}}{\partial \tilde{t}} + \tilde{u}\frac{\partial \tilde{u}}{\partial \tilde{x}} + \tilde{w}\frac{\partial \tilde{u}}{\partial \tilde{z}}\right) = -\frac{\partial \tilde{p}}{\partial \tilde{x}} + \frac{1}{Re}\left(\frac{\partial^2 \tilde{u}}{\partial \tilde{x}^2} + \frac{\partial^2 \tilde{u}}{\partial \tilde{z}^2}\right),$$ (6.9)

where the Reynolds number is represented as $Re = \frac{\rho V_o R_o}{\mu}$. As such, the density, ρ is 1, and the dynamic viscosity of water, μ is substituted with $1/Re$ in COMSOL. Boundary conditions include a moving wall along the z-axis with velocity V_o, and a slip condition for the menisci. The pressure was set to 0 at both end points of the slug.

In addition, the *Transport of Diluted Species Physics* was used to compute the concentration field according to the transport equation:

$$\frac{\partial c}{\partial t} + u\frac{\partial c}{\partial x} + w\frac{\partial c}{\partial z} = D\left(\frac{\partial^2 c}{\partial x^2} + \frac{\partial^2 c}{\partial z^2}\right),$$ (6.10)

where c is the concentration and D the diffusion coefficient. This equation was made dimensionless by the following substitutions:

$$\tilde{x} = \frac{x}{R_0}, \tilde{z} = \frac{z}{R_0}, \tilde{u} = \frac{u}{V_0}, \tilde{w} = \frac{w}{V_0}, \tilde{c} = \frac{c}{C_0} \text{ and } \tilde{t} = \frac{t}{T_0},$$ (6.11)

where the concentration scale is defined as $C_o = \frac{1}{R_o^3}$. Therefore, the dimensionless transport equation reads:

$$\frac{\partial \tilde{c}}{\partial \tilde{t}} + \tilde{u}\frac{\partial \tilde{c}}{\partial \tilde{x}} + \widetilde{w}\frac{\partial \tilde{c}}{\partial \tilde{z}} = \frac{1}{Pe}\left(\frac{\partial^2 \tilde{c}}{\partial \tilde{x}^2} + \frac{\partial^2 \tilde{c}}{\partial \tilde{z}^2}\right),$$

(6.12)

where the Peclet number is represented as $Pe = \frac{V_o R_o}{D}$. As such, D was substituted with $1/Pe$ in COMSOL. The initial condition for the concentration was defined as a step function that spans from 0 to 1 at the center of the slug, with a transition zone that is 4% of the slug length (see Figure 6.6). The boundary condition includes zero flux at all boundaries and free surfaces. The advantage of using the dimensionless form is that the effects of wall velocity, radius, and diffusion coefficient can be studied by altering only the Reynolds number or the Peclet number, or both.
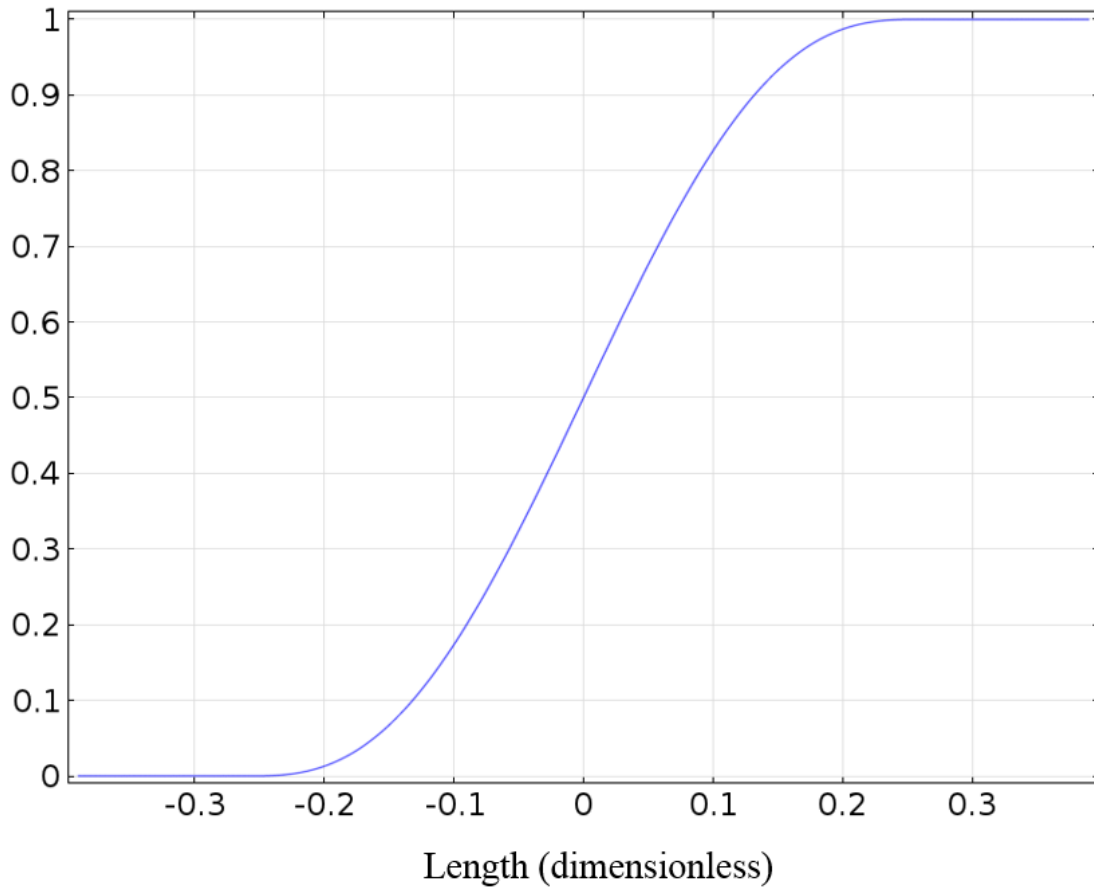
Figure 6.6: Step function profile with a transition zone across 4% the slug length (for a slug length-to-width ratio, $L/W = 13$)

6.7   Numerical Results and Discussion

6.7.1   Two-Phase Flow Moving Mesh Model

Body force or $\boldsymbol{F}$ values of 1, 10, 100, 400, 1000, 3000, 5000, 8000 and 10000 N/m^3 imposed in the z-direction were incorporated and solved for through Eq. (6.3) in our simulations in order to estimate the viscous resistive force, F_r. As a result of balanced body force and resistive force, the velocity of the slug eventually reaches a constant

124

value, in which the slug experiences no acceleration. As such, the resistive force is equivalent to the body force, which allows us to deduce the resistive force at the terminal velocity. The relationship between the viscous resistive force and terminal velocity was then obtained, as shown in Figure 6.7.
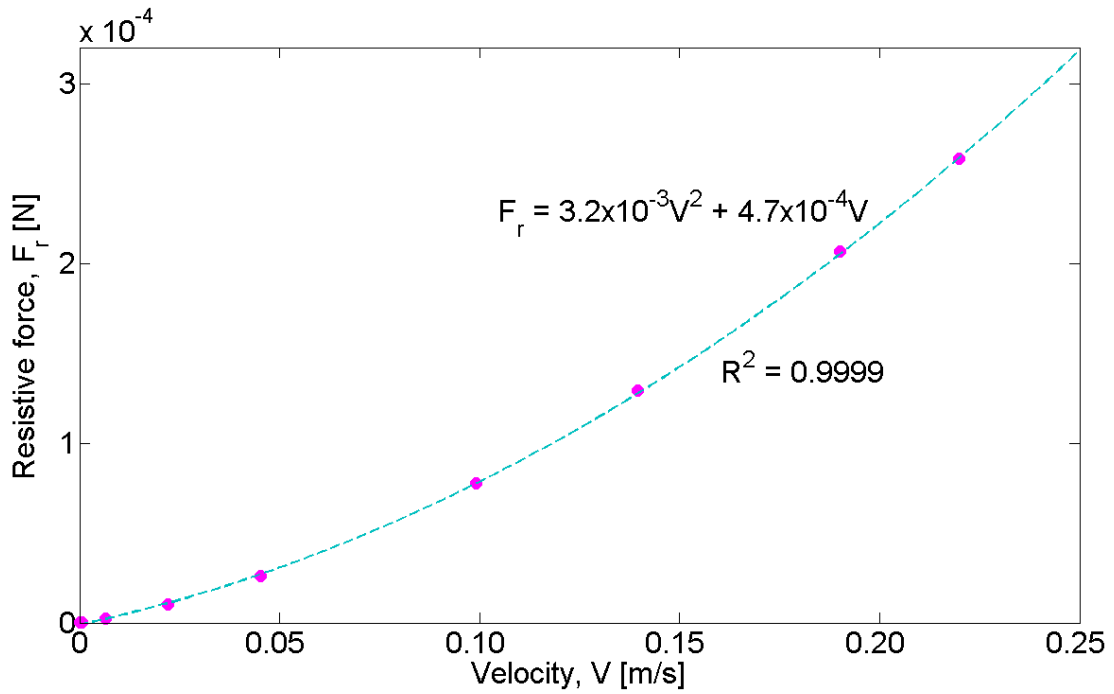
Figure 6.7: Relationship between viscous resistive force and velocity attained numerically

A quadratic fit showed the approximation of viscous resistive force as

$$F_r = 3.2 \times 10^{-3}V^2 + 4.7 \times 10^{-4}V, \tag{6.13}$$

where the multipliers 3.2×10^{-3} and 4.7×10^{-4} contain units of kg/m and kg/s respectively. The resistive force values obtained numerically compare well with values obtained analytically, as shown in Figure 6.8.
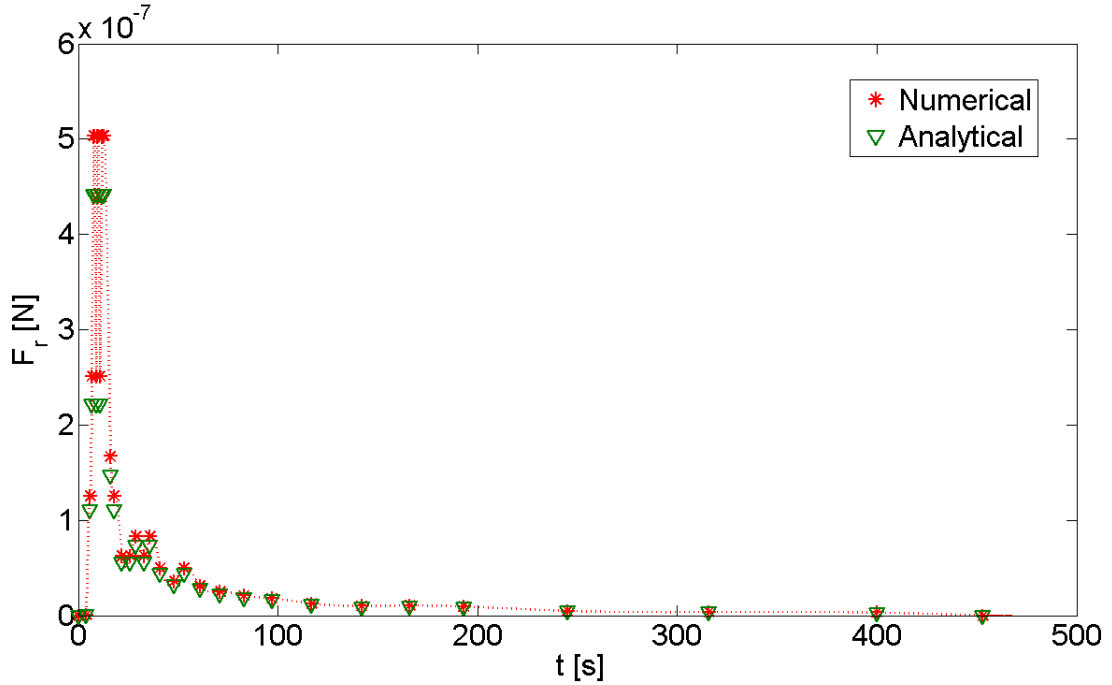
Figure 6.8: Comparison between numerical and analytical values of viscous resistive force, F_r

Using experimental values of velocity, F_r can now be calculated and substituted in Eq. (6.1) to yield the Marangoni force, F_σ. As shown in Figure 6.9(a) the numerical and analytical values of F_σ match very closely. The surface tension gradient between the right and left edges of the slug, $\sigma_a - \sigma_r$ can now be predicted by rearranging Eq. (6.2):

$$(\sigma_a - \sigma_r) = \frac{F_\sigma}{2\pi R \cos\theta_e}. \tag{6.14}$$

Our calculations show that the numerical and analytical values of $\sigma_a - \sigma_r$ also compare well since they are dependent on F_σ. Further analysis shows that only a small surface tension gradient, $\sim 3.5 \times 10^{-5}$ N/m is required to trigger slug motion.
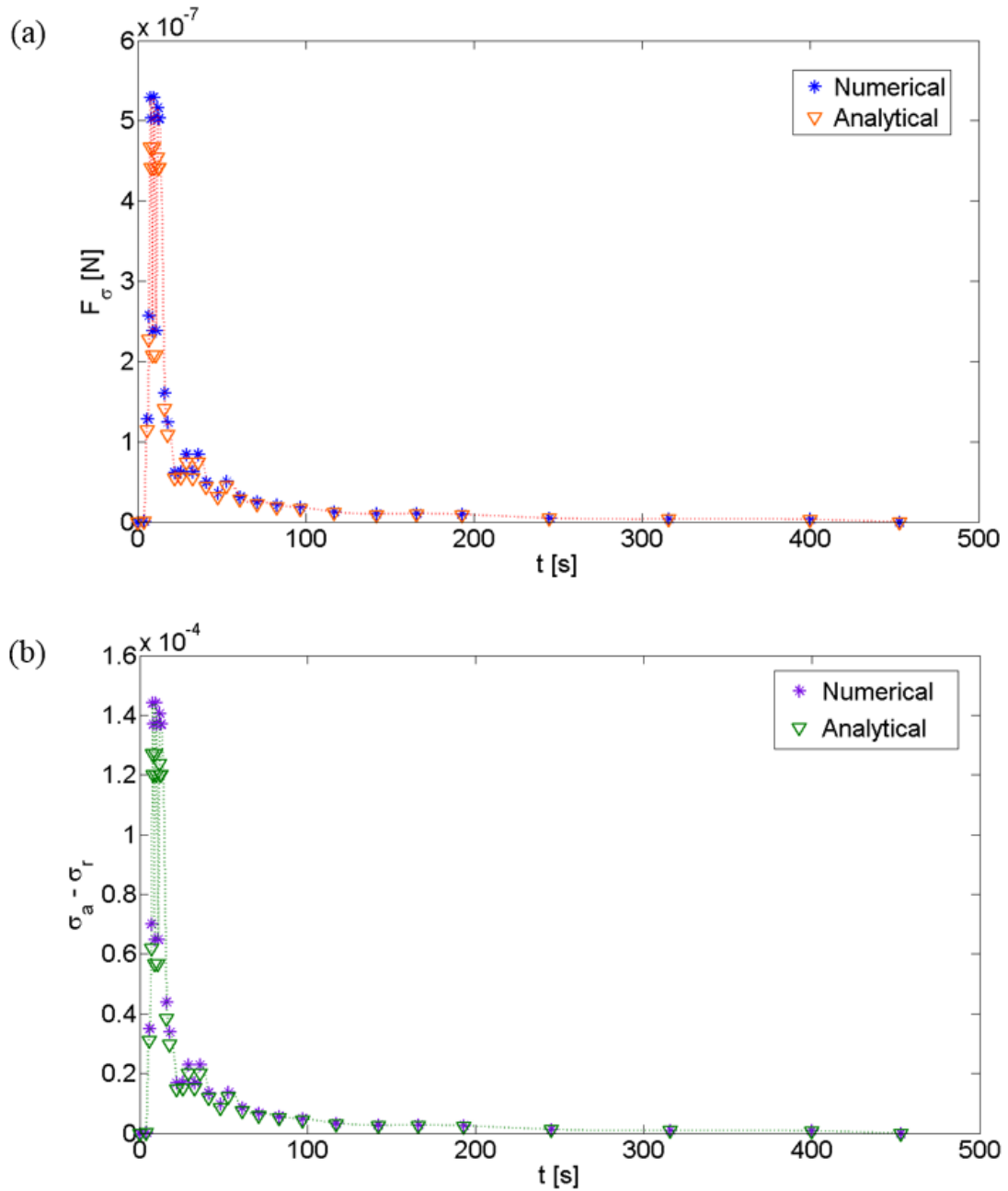
Figure 6.9: Comparison between analytical and numerical values of (a) Marangoni force, F_σ and (b) surface tension difference obtained based on F_σ

6.7.2 Single Phase Flow Model

We first define how well volumetric mixing is by defining the mixing index, M.I. as

$$M.I. = \frac{1}{2}\int (c - c_{eq})^2 d\Omega,$$

(6.15)

where c_{eq} represents the equilibrium concentration. Since we have defined the concentration as a step function located half-way through the slug and spans from 0 to 1, the concentration at equilibrium will be 0.5. As such, Eq. (6.16) is evaluated as

$$M.I. = \frac{1}{2}\int (c - 0.5)^2 d\Omega.$$

(6.16)

The effect of velocity can be studied by altering only the Reynolds and Peclet numbers. To calculate those numbers, we substituted water density, $\rho = 1000$ kg/m^3, water viscosity, $\mu = 10^{-3}$ Pa·s, tube radius, $R_o = 10^{-3}$ m, and diffusion coefficient, $D = 10^{-9}$ m^2/s. Using velocity values that ranged from $2.5 \times 10^{-4} - 3.0 \times 10^{-3}$ m^2/s, the corresponding Reynolds and Peclet numbers were inputted into our model, to obtain a distribution of mixing index as a function of time (see Figure 6.10). An increase in both the Reynolds and Peclet numbers resulted in a shorter time needed for complete mixing as a result of increasing velocity (see Figure 6.11). Here, we define 'complete mixing' by a mixing index of 2.67×10^{-3}, a number relatively close to 0. The mixing time is the time it takes to reach that mixing index, or as soon as the mixing index falls below that number.
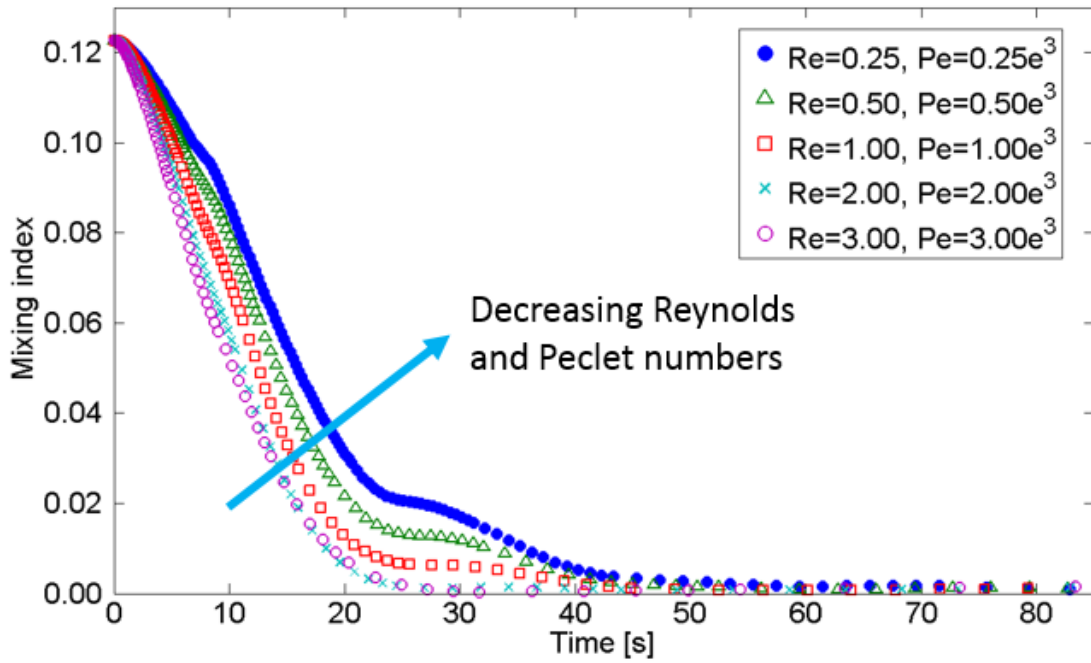
Figure 6.10: Mixing index as a function of time for various Reynolds and Peclet numbers
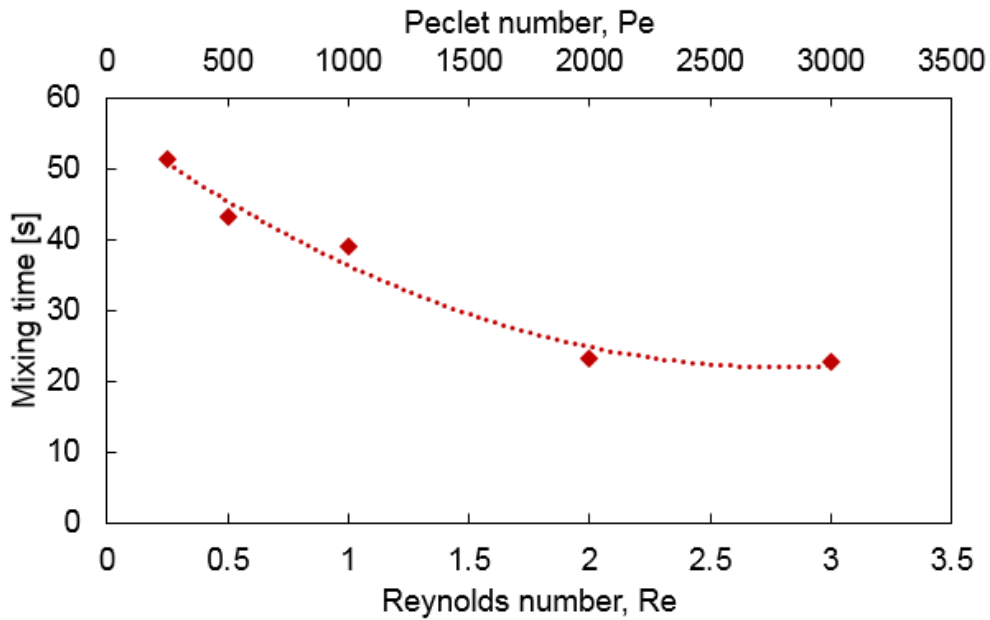
Figure 6.11: Mixing time as a function of Reynolds number and Peclet number

Compared to varying the velocity, varying the diffusivity alone affected only the Peclet number. A decrease in diffusivity corresponded to an increase in the Peclet number. As shown in Figure 6.12, the mixing time increases as the Peclet number increases, as a result of slower diffusivity.
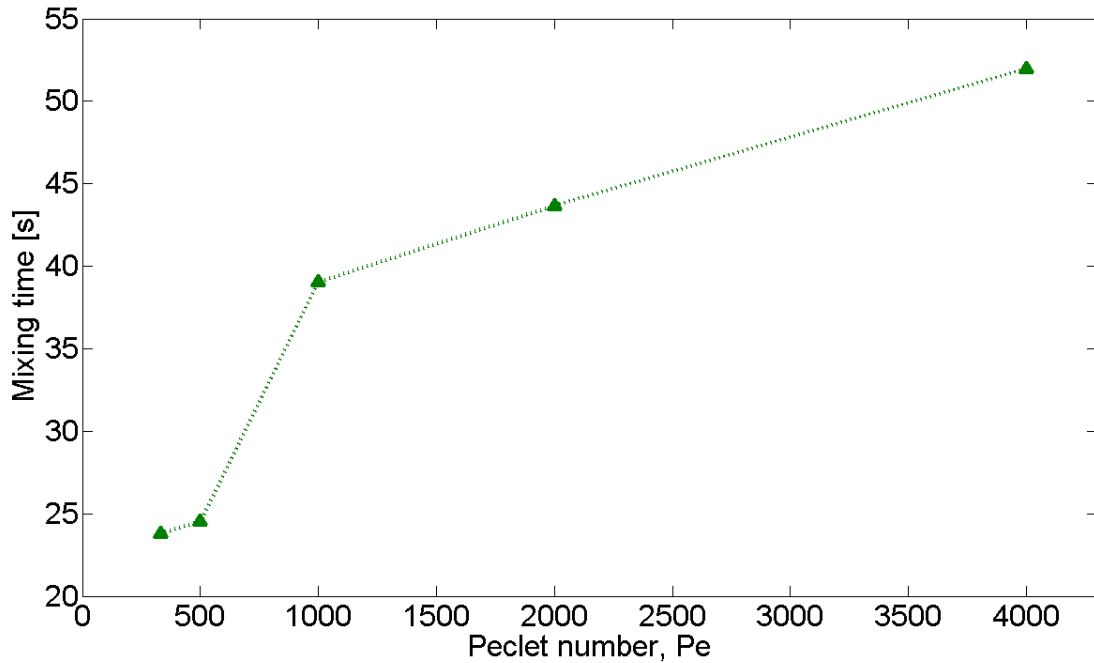
Figure 6.12: Mixing time as a function of Peclet number ($Re = 1$)

6.8   Conclusions

The validity of the numerical approach in estimating the viscous resistive forces of a slug in a capillary tube has been successfully shown, as evident from the good agreement between numerical and analytical values. The resistive force values, along with experimental velocity values, enable the calculation of the Marangoni force, F_σ. As such, the surface tension gradient between the right and left edges of the slug, $\sigma_a - \sigma_r$, was able to be predicted, whereby further analysis showed that only a

small gradient, ~ 3.5×10^{-5} N/m is required to trigger slug motion. This suggests that a wide range of liquids can be used to achieve slug motion. A dimensionless model, which allowed for the study of mixing time by adjusting only the Reynolds and Peclet numbers, has also been developed.

7 Conclusions

"Every new beginning comes from some other beginning's end." – Seneca

7.1 Propulsion on an Incline

The self-propulsion of a microliter food color droplet up an incline has been investigated. By patterning a hydrophilic trace on a PDMS substrate, we have shown that a food color droplet climbs uphill upon the introduction of an ethanol droplet adjacent to it - a phenomenon which shows self-propulsion due to surface tension gradient.

One of the challenges encountered was the short duration of the PDMS substrate hydrophilicity, which resulted in a limited time frame for self-propulsion. To overcome this issue, we treated the PDMS substrate with a PVP solution after a short exposure to oxygen-plasma. We found that the contact angle of a sessile water droplet measured on a PVP-treated surface remained at 27° for the first 10 days, while an untreated surface with only plasma-enhanced surface had an increase of 25° in contact angle. Not only that, the contact angle of an untreated surface was, on overage, 50° higher than a treated surface.

In addition to the optimization of surface hydrophilicity, we optimized the droplet volume for a 1 mm-wide trace. By assessing the distance traveled using various droplet volumes on a 1 mm-wide trace, we found 1 μl to be the optimum volume, based on the observable distance traveled, in addition to the droplet staying within the bounds of the

trace. Using the optimized hydrophilic trace and droplet volume, the food color droplet traveled at a maximum distance of ~ 10 mm at both 0º and 4º. Subsequent translations at 4º increments showed a linear downward trend, with zero translation at 24º.

To verify our experimental results, a mathematical model assuming a parabolic droplet profile was built using COMSOL. First, arduous derivations were carried out, beginning with the Navier-Stokes equation, to generate a set of governing equations to be used in COMSOL. The governing equations were converted to their dimensionless equivalents to render the model more robust where, the distance traveled at various angles of incline as well as the morphology of the droplet can be predicted by just inputting the width, volume, and contact angle. Our numerical solutions, which accounted for Marangoni, capillary and gravitational forces, validated our experimental observations, including the sliding of the droplet downhill at ~ 24º, which suggests the angle of incline at which gravitational pull and contact angle hysteresis overcomes Marangoni force. The model was also capable of predicting the morphology of the droplet, which is advantageous especially when it becomes a challenge to assess the droplets through image processing due to small volumes used. Depending upon the input parameters, the model was able to show lateral elongation as well as a decrease in droplet height as time progresses.

In summary, we have demonstrated a plausible mechanism for the self-propulsion of a droplet moving up an incline. This method increases the mixing of fluids since movement occurred in more than one direction. That the method does not rely on external sources such as power renders it a good choice for the development of portable devices.

7.2 Mixing Rate of Two Droplets

The mixing rate of two droplets with the presence of surface tension has been studied and compared with molecular diffusion. By pipetting two droplets of equal volume but differing surface tensions next to each other, we observed coalescence followed by the mixing of liquids.

The experiments were recorded to enable post-processing of frames to determine the time points at which the droplets start coalescing, and the instant when the droplets stop mixing. From the frames selected, mixing area was determined using two methods: (a) by measuring the mixed area, and (b) by extracting a line profile from the mixed region. We found that the values obtained using these two methods were comparable, which gave us the assurance that the values were representative.

We first assessed the mixing rate of a 1 μl Tartrazine (yellow food color) droplet in a 1 μl water droplet on a hydrophobic surface that is a polyethylene sheet. From goniometric measurements, we found that the surface tension of a Tartrazine droplet was almost twice that of a water droplet. Using the two methods mentioned above, we calculated the mixing rate to be in the 10^{-6} m^2/s range, which was four orders of magnitude higher than the value of molecular diffusion reported in a previous work pertaining to the diffusion of Tartrazine in a phosphate-buffered saline (PBS) solution.

Following that, we assessed the mixing rates of a 1 μl Tartrazine droplet in various 1 μl droplets of differing EtOH concentrations. Our results showed that the mixing rate did not vary by much with increasing EtOH concentration, and that the average mixing rate was $\sim 8.22 \times 10^{-6}$ m^2/s. Because none have reported the mixing of Tartrazine in EtOH, we compared our values with those reported by previous works pertaining to the

molecular diffusion of EtOH in water, since the main ingredient in the Tartrazine solution is water. To date, all measurements reported values in the 10^{-9} m^2/s range, obtained using enclosed setups, i.e. without the effects of surface tension or Marangoni.

To better understand our results, we constructed a laminar two-phase flow model on a spherical cap in COMSOL, which includes a free surface, a contact line, and the Marangoni effect. Our simulations agree with our experimental findings, in that mixing time is constant for all EtOH concentrations tested, and that mixing time improves significantly when Marangoni effects were present. In addition, the model showed an improvement in mixing rate at smaller diffusion coefficient values and at higher contact angle values.

Our experimental and numerical findings concluded that the presence of Marangoni stress, compared to molecular diffusion alone, indeed improves the mixing rate of two miscible liquids. This knowledge would be beneficial in applications that involve an air-liquid interface; for example, pulmonary drug delivery, ocular drug delivery and DNA analysis for open microfluidics.

7.3   Droplet Actuation in a Hele-Shaw Cell

We investigated the actuation of a microliter droplet subjected to both top and bottom contact lines. This was achieved by using a Hele-Shaw cell, which comprises of two parallel plates separated by a distance much smaller than the length of the plates such that fluid flow within the gap is laminar. Actuation of a food color droplet in the Hele-Shaw cell was observed upon lateral injection of an EtOH droplet. Based on the average of three separate actuations, the maximum distance traveled by the food color droplet

was ~ 18 mm in 36 s. The velocity of the traveling droplet decreases gradually as it travels further from the EtOH source.

In comparison to our work pertaining to horizontal droplet propulsion within a 1 mm-wide trace, as presented in this thesis, the distance traveled by a droplet held within a Hele-Shaw cell was longer. This may imply that the contact angle hysteresis of the interacting droplet in a Hele-Shaw cell was smaller than that in an open trace configuration.

In order to calculate the Marangoni force, F_σ of the traveling droplet, we first calculated the resistive force, F_r both analytically and numerically. Analytically, F_r was obtained by integrating the wall shear stress around the droplet. Numerically, we modeled a half-cylinder in COMSOL and used a range of values for the body force in the Navier-Stokes equation to obtain a relationship between the terminal velocity and the force from gravity. We deduced the resistive force, F_r from the body force values since at terminal velocity, F_r equals the force from gravity. The resulting Marangoni force, F_σ attained both analytically and numerically were in good agreement with each other.

Since we assumed that the actuation was of surface tension gradient arising from EtOH vapor dissolving in the food color droplet, we analyzed the EtOH concentration on the opposing ends of the food color droplet. Using the formula for the diffusion of point source in 2-D along with a few geometrical derivations of the interacting droplet setup, our results indeed showed a higher concentration of EtOH on the end closest to EtOH, which gradually decreases as the droplet travels further. Through mathematical analysis, we found that only a small surface tension difference between 8.8×10^{-5} N/m to 1.4×10^{-4} N/m is required to trigger droplet motion. Also, with further mathematical

analysis, we showed that the surface of the droplet increases, both with time and angular position, upon interaction with EtOH vapor.

In conclusion, we have not only demonstrated a feasible mechanism for droplet actuation in a Hele-Shaw cell, but also validated our numerical approach in estimating the Marangoni force, F_σ since the attained values compare well with analytical values. This mechanism of droplet actuation in an enclosed configuration may be beneficial in diagnostic devices especially when the reagents are hazardous, for example infectious samples and cancer-causing reagents.

7.4 Liquid Slug in Capillary Tube

We developed a COMSOL model based on the experimental parameters reported by Sellier et al. (2017) in their work pertaining to the spontaneous motion of a slug of miscible liquids in a capillary tube. Our aim was to use the numerical approach to estimate the viscous resistive forces associated with various body force values. As such, we did not incorporate any aspects of surface tension gradient in our model.

The water slug alone was modeled using the 2-D axisymmetric component in COMSOL, where a vertical symmetry axis was defined to enable a volumetric model of the slug. A frictional force in the liquid-solid interface was included to model the tube walls. By incorporating a range of body force values in the Navier-Stokes equation, our model showed a saturation in velocity as time progresses. At the terminal velocity, the body force is equivalent to the viscous resistive force. As such, we were able to obtain a relationship between the viscous resistive force, F_r and velocity. Using experimental velocity values as reported by Sellier et al. (2017), the corresponding resistive forces were found and subsequently used to calculate the Marangoni force, F_σ.

The latter enabled for the calculation of surface tension gradient between the right and left edges of the slug, $\sigma_a - \sigma_r$, in which we found that only a small gradient, $\sim 3.5 \times 10^{-5}$ N/m is required to trigger slug motion. This may suggest that slug motion in a capillary tube can be achieved using a wide range of liquids.

Analytically, viscous force values from the shear stress developed at the capillary tube walls were calculated by substituting experimental velocity values into a formula previously derived by Sellier et al. (2017). Our results showed good agreement between the numerical and analytical values, thus confirming the validity of our numerical approach. Further, subsequent calculations involving the resistive force, F_r also showed good agreement between values attained from both approaches. The quantities calculated include the Marangoni force, F_σ and the surface tension gradient, $\sigma_a - \sigma_r$. A dimensionless numerical model has also been developed to study the mixing time when a concentration gradient is introduced in the slug. By altering only the Reynolds and Peclet numbers, we show that mixing time increases as both numbers increase, as a result of increasing velocity. However, by altering only the Peclet number, through varying only the diffusion coefficient, mixing time increases as Peclet number increases, as a result of slower diffusivity.

In summary, a model that predicted resistive force well was developed, thereby enabling the calculation of Marangoni force and surface tension gradient for a slug in a capillary tube. A second dimensionless model built enabled the study of mixing time through varying only the Reynolds and Peclet numbers.

7.5   Advantages and Disadvantages

The propulsion method discussed in this thesis is based on the concept of surface tension gradient resulting from a volatile vapor dissolving into an adjacent water droplet, for which it has been shown feasible in the propulsion of (a) a droplet up an incline, (b) a droplet in a semi-enclosed setup, i.e. a Hele-Shaw cell, and (c) a droplet in a fully-enclosed setup, i.e. a capillary tube. Compared to other propulsion methods as mentioned in Section 2.3, the propulsion method investigated in this thesis does not require external power sources. Moreover, the device is easy and cost-effective to fabricate.

However, based on the use of an alcohol-based volatile liquid as fuel for propulsion, the mechanism investigated might not be suitable for biological applications, as alcohol kills cells. Nevertheless, we do not know for certain the quantifiable limit of alcohol percentage versus the rate of cell survival in a sample. Although alternative substances could be used to mitigate this issue, another method is to use EtOH vapor for droplet guiding, that is, the EtOH droplet is only held close to the water droplet, instead of being deposited onto the substrate where the water droplet sits. As such, the water droplet will not coalesce, or be in contact with a larger amount of EtOH at the end of motion.

8 Recommendations for Future Work

"Normal people... believe that if it ain't broke, don't fix it. Engineers believe that if it ain't broke, it doesn't have enough features yet." - Scott Adams, creator of Dilbert comic

This chapter presents a few ideas that could be further explored based on the work already carried out and reported in this thesis. According to Dr. Kaoru Ishikawa (1915-1989), a Japanese organizational theorist who is well-known for the Fishbone Diagram or the Ishikawa Diagram, an engineering problem can be tackled by looking at six aspects (6M): methods, machines, man, materials, measurement, and environment. In the same vein, the recommended ideas for future work are proposed based on assessing those areas. The details are presented in each of the following sub-sections, categorized according to the individual work presented in this thesis.

8.1   Propulsion on an Incline

The concept of propulsion on an incline can be further utilized to study the mixing of two droplets. A suggestion would be to create a small 3-D trench at the end of a planar trace. The purpose of the trench would be to hold a droplet in place, so that it gets mixed with a second droplet that is subjected to flow up an incline.

Similarly, one could also study the mixing behavior if the second droplet were to be directed downstream. Although, as observed experimentally, a droplet confined in a trace would naturally flow downstream when the substrate is tilted, the same cannot be

said for all tilt angles, especially when the tilt angle is small. As such, a fuel droplet such as ethanol would still need to be used to direct the droplet downstream. Through these experiments, one would be able to compare the mixing rate or mixing behavior for three configurations:

i.   Propulsion up an incline
ii.   Propulsion on a horizontal plane
iii. Propulsion down an incline

This idea stems from the analysis by Grigoriev et al. (2006)), where they reported increased mixing when a micro-droplet moves in more than one dimension. Following the hypothetical success of the above-mentioned ideas, one could then investigate the mixing rate of a droplet flowing in three directions: x, y, and z. The propulsion of a droplet up/down an incline only involves two directions: x and z. To include an additional y-direction, one would have to create a trace that is tilted (as viewed from the top), such as a Y-channel or an X-channel configuration. Similarly, a 3-D trench would also need to be fabricated at the end of the tilted trace in order to hold a droplet. As a result, one would then be able to analyze:

i.   The effect of trace tilt angle (top view) on mixing rate
ii.   The mixing rate of droplets subjected to flow in 2-dimension vs. 3-dimension

Finally, numerical simulations to confirm the experimental results from these proposed ideas can be carried out.

8.2   Mixing Rate of Two Droplets

In this thesis, the mixing rate of two droplets has been studied through a 2-D depiction of a yellow dye entering a clear ethanol liquid. However, only the top view has been taken into account in the study. In their study of droplets mixing in an EWOD configuration, Paik et al. (2003)) reported that rapid mixing may appear complete in the top view, but not in the side view. Therefore, to better understand the flow dynamics of the mixing droplets, examining the experiment from the side as well as from the top is recommended.

Further, by incorporating micro-sized polystyrene fluorescent particles in the droplets (Pradhan and Panigrahi, 2016), flow visualization and dynamics can be better profiled using optical methods, such as particle image velocimetry (PIV). By illuminating the particles using a laser source, the emission from the particles can then be captured by the photomultiplier tubes (PMT) in a confocal microscope. To further enhance the setup, the droplets could also be enclosed in a box to mitigate the effects of ambient air convection. In addition, errors that might have been caused by manual dispensing of the droplets can be minimized by using an automated micropipette dispensing system.

Also, since we have numerically shown the effects of contact angle on mixing rate, it would be useful to carry out experiments to validate that. As such, different substrates can be used in order to generate droplets of various contact angles using the same liquids.

8.3   Droplet Actuation in a Hele-Shaw Cell

We have briefly shown that a water droplet can be contained within a channel created from simply drawing two parallel lines using a permanent marker, on a plasma-treated glass. However, the channels started to dissolve upon interaction with EtOH. In order to make the channels non-dissolvable, one could try baking the entire plasma-treated glass that has channels already drawn. If this attempt does not solve the issue, one could also look into different types of liquids such as polyethylene glycol, which has a lower surface tension than water and is not alcohol-based, to achieve guided actuation along the channel. This mechanism for guided passive droplet transport in an enclosed system may be useful in diagnostic portable devices, especially when the reagents under test are hazardous (Yobas et al., 2009).

In addition to droplet actuation, the Hele-Shaw cell can potentially be used to study the mixing of droplets. A straightforward way would be to use two liquid dye droplets of different colors, so that mixing can be readily observed. For example, one first deposits a blue droplet in the cell, followed by a yellow droplet at a fixed distance away from the blue droplet. One can then deposit a fuel droplet, such as ethanol, adjacent to either one of the droplets so that it moves towards the other droplet and eventually coalesces. The formation of green color within the coalesced droplets signifies mixing and can be further studied through image processing. This experiment can also be performed using the setups for "mixing rate of two droplets" and "liquid slug in capillary tube". As a result, one would be able to make conclusions about the mixing rate for three different setups, categorized according to their air-liquid interface exposure:

   i.   Fully-exposed – as in "Mixing Rate of Two Droplets"
   ii.   Partially-enclosed – as in "Hele-Shaw Droplet"
   iii. Fully-enclosed – as in "Liquid Slug in Capillary Tube"

Since a droplet is held between two plates in a Hele-Shaw cell, a trench would not be necessary to keep a droplet in place to study mixing. Therefore, one could pattern only 2D traces within the cell to enable guided propulsion, as well as to study mixing. However, if one were to study the mixing rate in a tilted Hele-Shaw cell, one would have to incorporate a small trench on the bottom substrate. Our preliminary testing showed an immediate downstream flow of the droplet once the cell is tilted. Therefore, it would be rather challenging to study the uphill climb of a Hele-Shaw droplet. Nevertheless, one could still examine the mixing rate based on the coalescence of a droplet flowing downstream with a pre-deposited droplet in a trench.

Similarly, the mixing rate can be assessed through image processing as discussed under the "mixing rate of two droplets" work in this thesis. As a result, one could potentially study the effect of tilt angle on mixing rate, based on three different setups, categorized according to their air-liquid interface exposure:

  i.   Fully-exposed – as in "Propulsion on an Incline"
  ii.   Semi-enclosed – as in "Hele-Shaw Droplet"
  iii. Fully-enclosed – as in "Liquid Slug in Capillary Tube"

Lastly, numerical simulations to model a Hele-Shaw droplet coalescing with a droplet downhill would be recommended.

8.4   Liquid Slug in Capillary Tube

By systematically varying the length, L and radius, R of the capillary tube, physical experiments can be performed to assess the maximum velocity, V_{max} in order to verify the scaling law that was validated numerically by Sellier et al. (2017). Further, the

effect of contact angle on distance traveled and velocity can be investigated by using different liquids. As mentioned in the previous two sub-sections, the setup used for "liquid slug in a capillary tube" can be further utilized to study liquid mixing, for both the horizontal and inclined cases. Since the setup is fairly simple, PIV measurements can be incorporated for further study of flow dynamics.

Similarly, numerical simulations incorporating the effects of surface tension gradient can be carried out to validate the physical experiment results, as well as results reported by Sellier et al. (2017). Thus, one could potentially obtain a comparison between experimental, theoretical and numerical results for:

i. Scaling law from maximum velocity, V_{max}
ii. Effect of contact angle
iii. Mixing efficiency

Appendix A

Derivation of the governing equations for the droplet confined on a hydrophilic stripe

We begin with the following governing equations:

$$\frac{\partial h}{\partial t} = -\frac{\partial q_x}{\partial x},$$

(A.1)

$$q_x = -\frac{h^3}{3\mu}\left(\frac{\partial p}{\partial x} - \rho g \sin\alpha\right) + \frac{\tau h^2}{2\mu},$$

(A.2)

$$p = -\sigma\left(\frac{\partial^2 h}{\partial x^2} + \frac{\partial^2 h}{\partial y^2}\right) - \Pi,$$

(A.3)

$$\frac{\partial ch}{\partial t} = -\frac{\partial}{\partial x}(cq_x) + D\frac{\partial}{\partial x}\left(h\frac{\partial c}{\partial x}\right),$$

(A.4)

as well as the expressions for the dependent variables in the governing equations:

$$\Pi(h, h^*) = B\left[\left(\frac{h^*}{h}\right)^n - \left(\frac{h^*}{h}\right)^m\right],$$

(A.5)

$$h(x, y, t) = h_c(x, t)\left(1 - \frac{4y^2}{w^2}\right),$$

(A.6)

$$c = \frac{h_1}{h},$$

(A.7)

$$\tau = -\frac{\partial \sigma}{\partial c} \cdot \frac{\partial c}{\partial x}.$$

(A.8)

First, we integrate Eq. (A.1) across the width of the stripe:

$$\int_{\frac{-w}{2}}^{\frac{w}{2}} \frac{\partial h}{\partial t} dy = \int_{\frac{-w}{2}}^{\frac{w}{2}} -\frac{\partial q_x}{\partial x} dy,$$

(A.9)

$$\int_{\frac{-w}{2}}^{\frac{w}{2}} \frac{\partial h}{\partial t} dy = -\frac{\partial}{\partial x} Q_x,$$

(A.10)

where, with reference to Eq. (A.2),

$$Q_x = \int_{\frac{-w}{2}}^{\frac{w}{2}} q_x \, dy = \int_{\frac{-w}{2}}^{\frac{w}{2}} \left\{ -\frac{h^3}{3\mu} \left(\frac{\partial p}{\partial x} - \rho g \sin \alpha \right) + \frac{\tau h^2}{2\mu} \right\} dy.$$

(A.11)

We next evaluate Eq. (A.11) by assessing each of the three terms, from left to right. For the first term,

$$\int_{\frac{-w}{2}}^{\frac{w}{2}} -\frac{h^3}{3\mu} \frac{\partial p}{\partial x} dy = \int_{\frac{-w}{2}}^{\frac{w}{2}} -\frac{h^3}{3\mu} \frac{\partial}{\partial x} \left\{ -\sigma \left(\frac{\partial^2 h}{\partial x^2} + \frac{\partial^2 h}{\partial y^2} \right) - \Pi \right\} dy.$$

(A.12)

This equation can be re-written as

147

$$\int_{-\frac{w}{2}}^{\frac{w}{2}} -\frac{h^3}{3\mu}\frac{\partial}{\partial x}\left\{-\sigma\left(\frac{\partial^2 h}{\partial x^2}+\frac{\partial^2 h}{\partial y^2}\right)\right\}dy - \int_{-\frac{w}{2}}^{\frac{w}{2}} -\frac{h^3}{3\mu}\frac{\partial \Pi}{\partial x}dy. \tag{A.13}$$

By substituting Eq. (A.6) into the left-hand term of the equation above, we obtain

$$\int_{-\frac{w}{2}}^{\frac{w}{2}} -\frac{h^3}{3\mu}\left(1-\frac{4y^2}{w^2}\right)^3\frac{\partial}{\partial x}\left\{-\sigma\left(\left(1-\frac{4y^2}{w^2}\right)\frac{\partial^2 h_c}{\partial x^2}-\frac{8h_c}{w^2}\right)\right\}dy, \tag{A.14}$$

$$\int_{-\frac{w}{2}}^{\frac{w}{2}} -\frac{h^3}{3\mu}\left(1-\frac{4y^2}{w^2}\right)^4\frac{\partial}{\partial x}\left(-\sigma\frac{\partial^2 h_c}{\partial x^2}\right)dy + \int_{-\frac{w}{2}}^{\frac{w}{2}} -\frac{h^3}{3\mu}\left(1-\frac{4y^2}{w^2}\right)^3\frac{\partial}{\partial x}\left(\sigma\frac{8h_c}{w^2}\right)dy, \tag{A.15}$$

$$-\frac{h^3}{3\mu}\frac{\partial}{\partial x}\left(-\sigma\frac{\partial^2 h_c}{\partial x^2}\right)\int_{-\frac{w}{2}}^{\frac{w}{2}}\left(1-\frac{4y^2}{w^2}\right)^4 dy - \frac{h^3}{3\mu}\frac{\partial}{\partial x}\left(-\sigma\frac{8h_c}{w^2}\right)\int_{-\frac{w}{2}}^{\frac{w}{2}}\left(1-\frac{4y^2}{w^2}\right)^3 dy, \tag{A.16}$$

$$-\frac{h^3}{3\mu}\frac{\partial}{\partial x}\left(-\sigma\frac{\partial^2 h_c}{\partial x^2}\right)\frac{128w}{315} - \frac{h^3}{3\mu}\frac{\partial}{\partial x}\left(\sigma\frac{8h_c}{w^2}\right)\frac{16w}{35}. \tag{A.17}$$

Next, we evaluate the right-hand term of Eq. (A.13):

$$\int_{-\frac{w}{2}}^{\frac{w}{2}} -\frac{h^3}{3\mu}\frac{\partial \Pi}{\partial x}dy = \int_{-\frac{w}{2}}^{\frac{w}{2}} -\frac{h^3}{3\mu}\left(\frac{\partial \Pi}{\partial h}\right)\left(\frac{\partial h}{\partial x}\right)dy. \tag{A.18}$$

Taking the derivative of Eq. (A.5), we obtain

$$\frac{\partial \Pi}{\partial h} = -\frac{B}{h}\left[n\left(\frac{h^*}{h}\right)^n - m\left(\frac{h^*}{h}\right)^m\right]. \tag{A.19}$$

Therefore, with Eq. (A.6) and Eq. (A.19), we can now expand Eq. (A.18) as follows:

$$\int_{\frac{-w}{2}}^{\frac{w}{2}} -\frac{h_c{}^3}{3\mu}\left(1-\frac{4y^2}{w^2}\right)^3 \frac{B}{h_c\left(1-\frac{4y^2}{w^2}\right)}\left[n\left(\frac{h^*}{h_c\left(1-\frac{4y^2}{w^2}\right)}\right)^n\right.$$

$$\left.-m\left(\frac{h^*}{h_c\left(1-\frac{4y^2}{w^2}\right)}\right)^m\right]\frac{\partial}{\partial x}h_c\left(1-\frac{4y^2}{w^2}\right)dy, \tag{A.20}$$

$$-\frac{h_c{}^3}{3\mu}\frac{\partial h_c}{\partial x}B\left[\frac{nh^{*n}}{h_c^n}\int_{\frac{-w}{2}}^{\frac{w}{2}}\frac{\left(1-\frac{4y^2}{w^2}\right)^3}{\left(1-\frac{4y^2}{w^2}\right)^n}dy-\frac{mh^{*m}}{h_c^m}\int_{\frac{-w}{2}}^{\frac{w}{2}}\frac{\left(1-\frac{4y^2}{w^2}\right)^3}{\left(1-\frac{4y^2}{w^2}\right)^m}dy\right]. \tag{A.21}$$

By substituting $n = 3$ and $m = 2$, we obtain

$$\frac{h_c{}^3}{3\mu}\frac{\partial h_c}{\partial x}B\left[\frac{nh^{*n}w}{h_c^n}-\frac{mh^{*m}}{h_c^m}\int_{\frac{-w}{2}}^{\frac{w}{2}}\left(1-\frac{4y^2}{w^2}\right)dy\right], \tag{A.22}$$

$$\frac{h_c{}^3}{3\mu}Bw\frac{\partial}{\partial x}\left[\left(\frac{h^*}{h_c}\right)^n-\frac{2}{3}\left(\frac{h^*}{h_c}\right)^m\right]. \tag{A.23}$$

We next evaluate the second term in Eq. (A.11). By substitution of Eq. (A.6), we obtain the following:

$$\int_{\frac{-w}{2}}^{\frac{w}{2}} -\frac{h^3}{3\mu}(-\rho g\sin\alpha)\,dy = \rho g\sin\alpha\frac{h_c{}^3}{3\mu}\int_{\frac{-w}{2}}^{\frac{w}{2}}\left(1-\frac{4y^2}{w^2}\right)^3 dy, \tag{A.24}$$

149

$$\int_{\frac{-w}{2}}^{\frac{w}{2}} -\frac{h^3}{3\mu}(-\rho g \sin \alpha)\, dy = \rho g \sin \alpha \frac{h_c{}^3}{3\mu} \frac{16w}{35}.$$ (A.25)

Using Eq. (A.6), Eq. (A.7) and Eq. (A.8), the third term in Eq. (A.11) is evaluated as

$$\int_{\frac{-w}{2}}^{\frac{w}{2}} \frac{\tau h^2}{2\mu}\, dy = \frac{1}{2\mu}\frac{\partial \sigma}{\partial c} \int_{\frac{-w}{2}}^{\frac{w}{2}} \left(h\frac{\partial h_1}{\partial x} - h_1\frac{\partial h}{\partial x} \right) dy,$$ (A.26)

$$\int_{\frac{-w}{2}}^{\frac{w}{2}} \frac{\tau h^2}{2\mu}\, dy = \frac{1}{2\mu}\frac{\partial \sigma}{\partial c} \int_{\frac{-w}{2}}^{\frac{w}{2}} \left(1 - \frac{4y^2}{w^2} \right)^2 \left(h_c\frac{\partial h_1}{\partial x} - h_1\frac{\partial h_c}{\partial x} \right) dy,$$ (A.27)

$$\int_{\frac{-w}{2}}^{\frac{w}{2}} \frac{\tau h^2}{2\mu}\, dy = \frac{1}{2\mu}\frac{\partial \sigma}{\partial c} \left(h_c\frac{\partial h_1}{\partial x} - h_1\frac{\partial h_c}{\partial x} \right) \int_{\frac{-w}{2}}^{\frac{w}{2}} \left(1 - \frac{4y^2}{w^2} \right)^2 dy,$$ (A.28)

$$\int_{\frac{-w}{2}}^{\frac{w}{2}} \frac{\tau h^2}{2\mu}\, dy = \frac{1}{2\mu}\frac{\partial \sigma}{\partial c} \left(h_c\frac{\partial h_1}{\partial x} - h_1\frac{\partial h_c}{\partial x} \right) \frac{8w}{15}.$$ (A.29)

Therefore, combining Eq. (A.17), (A.23), (A.25) and (A.29), we obtain

$$
\begin{aligned}
Q_x = {} & -\frac{h_c{}^3}{3\mu}\frac{\partial}{\partial x}\left\{ -\sigma\left(\frac{128w}{315}\frac{\partial^2 h_c}{\partial x^2} - \frac{128h_c}{35w^2} \right) \right\} \\
& -\frac{h_c{}^3}{3\mu}\frac{\partial}{\partial x}\left\{ Bw\left[\left(\frac{h^*}{h_c}\right)^n - \frac{2}{3}\left(\frac{h^*}{h_c}\right)^m \right] \right\} + \frac{h_c{}^3}{3\mu}\left(\frac{16w}{35}\rho g \sin \alpha \right) \\
& + \frac{1}{2\mu}\frac{\partial \sigma}{\partial c}\frac{8w}{15}\left(h_c\frac{\partial h_1}{\partial x} - h_1\frac{\partial h_c}{\partial x} \right).
\end{aligned}
$$ (A.30)

Eq. (A.30) consists of four terms. The first two terms starting from the left are expressions for pressure, p. To equate these two terms to the form as stated in Eq. (A.3), we factor out $\frac{h_c{}^3}{3\mu}$ and multiply with $\frac{1}{w}$ to obtain

$$p = -\sigma \left(\frac{128w}{315} \frac{\partial^2 h_c}{\partial x^2} - \frac{128 h_c}{35 w^2} \right) + B \left[\left(\frac{h^*}{h_c} \right)^n - \frac{2}{3} \left(\frac{h^*}{h_c} \right)^m \right].$$

(A.31)

Therefore, using Eq. (A.31), we can now express Eq. (A.30) as

$$Q_x = -\frac{h_c^3}{3\mu} w \left(\frac{\partial p}{\partial x} - \rho g \sin \alpha \right) - \frac{1}{\mu} \frac{\partial \gamma}{\partial c} \frac{4w}{15} \left(h_c \frac{\partial h_1}{\partial x} - h_1 \frac{\partial h_c}{\partial x} \right).$$

(A.32)

We have thus shown the derivations for Eq. (3.9) and Eq. (3.10) of Chapter 3.

Next, to derive Eq. (3.11) of Chapter 3, we evaluate Eq. (A.4). By expressing Eq. (A.4) in terms of Eq. (A.7), we obtain

$$\frac{\partial h_1}{\partial t} = -\frac{\partial}{\partial x} (c q_x) + D \frac{\partial y}{\partial x} \left(h \frac{\partial c}{\partial x} \right).$$

(A.33)

Then, we integrate Eq. (A.33) over the width of the stripe:

$$\int_{\frac{-w}{2}}^{\frac{w}{2}} \frac{\partial h_1}{\partial t} dy = \int_{\frac{-w}{2}}^{\frac{w}{2}} -\frac{\partial}{\partial x} (c q_x) \, dy + \int_{\frac{-w}{2}}^{\frac{w}{2}} D \frac{\partial}{\partial x} \left(h \frac{\partial c}{\partial x} \right) dy.$$

(A.34)

By assuming a parabolic profile, the left-hand term of Eq. (A.34) is evaluated as

$$\int_{\frac{-w}{2}}^{\frac{w}{2}} \frac{\partial h_1}{\partial t} dy = \int_{\frac{-w}{2}}^{\frac{w}{2}} h_1 \left(1 - \frac{4y^2}{w^2} \right) dy,$$

(A.35)

151

$$\int_{-\frac{w}{2}}^{\frac{w}{2}} \frac{\partial h_1}{\partial t} dy = \int_{-\frac{w}{2}}^{\frac{w}{2}} \frac{\partial}{\partial t} h_1 \, dy - \int_{-\frac{w}{2}}^{\frac{w}{2}} \frac{\partial}{\partial t} h_1 \frac{4y^2}{w^2} dy, \tag{A.36}$$

$$\int_{-\frac{w}{2}}^{\frac{w}{2}} \frac{\partial h_1}{\partial t} dy = \frac{2w}{3} \frac{\partial h_1}{\partial t}. \tag{A.37}$$

The first term on the right-hand side of Eq. (A.34) is evaluated as

$$\int_{-\frac{w}{2}}^{\frac{w}{2}} -\frac{\partial}{\partial x}(cq_x) \, dy = -\frac{\partial}{\partial x} \left\{ c \int_{-\frac{w}{2}}^{\frac{w}{2}} q_x \, dy \right\}, \tag{A.38}$$

$$\int_{-\frac{w}{2}}^{\frac{w}{2}} -\frac{\partial}{\partial x}(cq_x) \, dy = -\frac{\partial}{\partial x} \{cQ_x\}. \tag{A.39}$$

By substituting Eq. (A.7), the expression above becomes

$$\int_{-\frac{w}{2}}^{\frac{w}{2}} -\frac{\partial}{\partial x}(cq_x) \, dy = -\frac{\partial}{\partial x} \left\{ \frac{h_1}{h_c} Q_x \right\}. \tag{A.40}$$

Next, using Eq. (A.6), the second term on the right-hand side of Eq. (A.34) is evaluated as

$$\int_{-\frac{w}{2}}^{\frac{w}{2}} D \frac{\partial}{\partial x}\left(h \frac{\partial c}{\partial x}\right) dy = D \frac{\partial}{\partial x} \int_{-\frac{w}{2}}^{\frac{w}{2}} h_c \left(1 - \frac{4y^2}{w^2}\right) dy \frac{\partial c}{\partial x}, \tag{A.41}$$

$$\int_{-\frac{w}{2}}^{\frac{w}{2}} D \frac{\partial}{\partial x}\left(h \frac{\partial c}{\partial x}\right) dy = D \frac{\partial}{\partial x}\left\{\frac{2wh_c}{3} \frac{\partial c}{\partial x}\right\}, \tag{A.42}$$

Using Eq. (A.7), the expression above becomes

$$\int_{-\frac{w}{2}}^{\frac{w}{2}} D \frac{\partial}{\partial x}\left(h \frac{\partial c}{\partial x}\right) dy = D \frac{\partial}{\partial x}\left\{\frac{2w}{3}\left(\frac{\partial h_1}{\partial x} - \frac{h_1}{h_c} \frac{\partial h_c}{\partial x}\right)\right\}. \tag{A.43}$$

Therefore, Eq. (A.4) can now be written by combining Eq. (A.37), (A.40) and (A.43):

$$\frac{2w}{3} \frac{\partial h_1}{\partial t} = -\frac{\partial}{\partial x}\left(\frac{h_1}{h_c} Q_x\right) + D \frac{2w}{3} \frac{\partial}{\partial x}\left(\frac{\partial h_1}{\partial x} - \frac{h_1}{h_c} \frac{\partial h_c}{\partial x}\right), \tag{A.44}$$

which is the expression for Eq. (3.11).

Appendix B

Derivation of droplet volume and equilibrium contact angle

The COMSOL model used for the work, "Propulsion on an Incline" had been set up in such a way that a user needs to input only the trace width, contact angle and droplet volume to obtain distance traveled. As such, mathematical derivations have been carried out to relate the parameters.

First, the centerline height of a droplet resting on a horizontal plane at equilibrium is defined as

$$h_c(x, t = 0) = h_o \left(1 - \left(\frac{x}{r_o} \right)^2 \right),$$

(B.1)

where h_o and r_o represent the characteristic height and radius of the droplet respectively. Assuming a parabolic droplet profile, the centerline height can be expanded as

$$h(x, y, t = 0) = h_o \left(1 - \left(\frac{x}{r_o} \right)^2 \right) \left(1 - \frac{4y^2}{w^2} \right),$$

(B.2)

where w is the width of the trace. By substituting

$$r_o = \frac{l_o}{2}, \tag{B.3}$$

where l_o represents the length of the droplet, the volume of the droplet is expressed as

$$V = \int_{-\frac{l_o}{2}}^{\frac{l_o}{2}} \int_{-\frac{w}{2}}^{\frac{w}{2}} h_o \left(1 - \left(\frac{2x}{l_o} \right)^2 \right) \left(1 - \frac{4y^2}{w^2} \right) dy \, dx. \tag{B.4}$$

As such, the final expression for the volume of the droplet in terms of the characteristic height and length of the droplet as well as the trace width is

$$V = \frac{4}{9} w h_o l_o. \tag{B.5}$$

The contact angle is evaluated as

$$\theta_{eq} = \frac{dh_c}{dx} \bigg|_{x=-r_o}. \tag{B.6}$$

Therefore,

$$\theta_{eq} = -2x \frac{h_o}{r_o^2}. \tag{B.7}$$

Evaluating the equation above at $x = -r_o$ and substituting the relation from Eq. (B.3), we obtain

$$\theta_{eq} = \frac{4h_o}{l_o}. \tag{B.8}$$

Eq. (B.5) and Eq. (B.8) enable the calculation of the characteristic height and length of a droplet, given the trace width, contact angle and volume.

Appendix C

Derivation of slug meniscus

To model the slug meniscus for the work "Liquid Slug in a Capillary Tube" in COMSOL, the radius of the capillary tube, R_o had been used as the common variable to relate the radius of a circle, R, and the height, $R - h$, of a right-triangle abc (see Figure C.1).
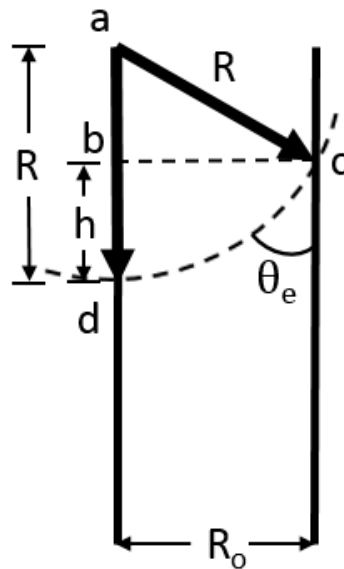
Figure C.1: An illustration showing the parameters that define the meniscus of a slug in a capillary tube. R_o is the tube radius, R is the radius a circle that forms the meniscus, $R - h$ is the height of a right triangle abc, and θ_e is the equilibrium contact angle

With the assumption of a right-triangle bcd, and an equilibrium contact angle θ_e of $\pi/3$, h is defined as

$$h = \tan\frac{\pi}{6}R_0. \tag{C.1}$$

By Pythagorean Theorem, triangle abc is expressed as

$$R^2 = R_o^2 + (R - h)^2. \tag{C.2}$$

By substituting Equation C.1 into Equation C.2, we arrive with the expression

$$R = \frac{R_o\left(1 + \tan^2\frac{\pi}{6}\right)}{2\tan\frac{\pi}{6}}. \tag{C.3}$$

Eq. (C.1) and Eq. (C.3) enable the COMSOL modeling of the meniscus formed by the slug in a capillary tube.

Bibliography

Abbyad, P., Dangla, R., Alexandrou, A., Baroud, C.N., 2011. Rails and anchors: guiding and trapping droplet microreactors in two dimensions. Lab Chip 11, 813–821.

Ahmed, G., Sellier, M., Jermy, M., Taylor, M., 2014. Modeling the effects of contact angle hysteresis on the sliding of droplets down inclined surfaces. Eur. J. Mech. - B Fluids 48, 218–230.

Amselem, G., Brun, P.T., Gallaire, F., Baroud, C.N., 2015. Breaking anchored droplets in a microfluidic Hele-Shaw cell. Phys. Rev. Appl. 3, 054006.

Andrieu, C., Beysens, D.A., Nikolayev, V.S., Pomeau, Y., 2002. Coalescence of sessile drops. J. Fluid Mech. 453, 427–438.

Arnold, J.H., 1930. Studies in Diffusion. Ind. Eng. Chem. 22, 1091–1095.

Bain, C.D., Burnett-Hall, G.D., Montgomerie, R.R., 1994. Rapid motion of liquid drops. Nature 372, 414–415.

Baldauf, W., Knapp, H., 1983. Measurements of diffusivities in liquids by the dispersion method. Chem. Eng. Sci. 38, 1031–1037.

Bansal, S., Sen, P., 2016. Mixing enhancement by degenerate modes in electrically actuated sessile droplets. Sens. Actuators B Chem. 232, 318–326.

Benilov, E.S., 2011. Thin three-dimensional drops on a slowly oscillating substrate. Phys. Rev. E 84, 066301.

Benilov, E.S., Billingham, J., 2011. Drops climbing uphill on an oscillating substrate. J. Fluid Mech. 674, 93–119.

Benilov, E.S., Cummins, C.P., 2013. Thick drops on a slowly oscillating substrate. Phys. Rev. E 88, 023013.

Berthier, J., 2008. Microdrops and Digital Microfluidics, First. ed. William Andrew, Norwich, NY.

Berthier, J., Silberzan, P., 2009. Microfluidics for Biotechnology, Second Edition, Artech House, Boston.

Bico, J., Quéré, D., 2002. Self-propelling slugs. J. Fluid Mech. 467, 101–127.

Bico, J., Quéré, D., 2001. Falling Slugs. J. Colloid Interface Sci. 243, 262–264.

Bico, J., Quéré, D., 2000. Liquid trains in a tube. EPL Europhys. Lett. 51, 546.

Blanchette, F., 2010. Simulation of Mixing within Drops due to Surface Tension Variations. Phys. Rev. Lett. 105, 074501.

Bontoux, N., Dauphinot, L., Vitalis, T., Studer, V., Chen, Y., Rossier, J., Potier, M.-C., 2008. Integrating whole transcriptome assays on a lab-on-a-chip for single cell gene profiling. Lab Chip 8, 443.

Borcia, R., Bestehorn, M., 2014. A phase field description of self-propulsion of twin sessile drops induced by surface tension gradients. Fluid Dyn. Res. 46, 041405.

Borcia, R., Bestehorn, M., 2013. Partial Coalescence of Sessile Drops with Different Miscible Liquids. Langmuir 29, 4426–4429.

Borcia, R., Menzel, S., Bestehorn, M., Karpitschka, S., Riegler, H., 2011. Delayed coalescence of droplets with miscible liquids: Lubrication and phase field theories. Eur. Phys. J. E Soft Matter 34, 1–9.

Bormashenko, E., Pogreb, R., Bormashenko, Y., Musin, A., Stein, T., 2008. New investigations on ferrofluidics: ferrofluidic marbles and magnetic-field-driven drops on superhydrophobic surfaces. Langmuir 24, 12119–12122.

Bratukhin, Y.K., Zuev, A.L., 1984. Thermocapillary drift of an air bubble in a horizontal Hele-Shaw cell. Fluid Dyn. 19, 393–398.

Bretherton, F.P., 1961. The motion of long bubbles in tubes. J. Fluid Mech. 10, 166–188.

Brochard, F., 1989. Motions of droplets on solid surfaces induced by chemical or thermal gradients. Langmuir 5, 432–438.

Brown, W., Rymden, R., Van Stam, J., Almgren, M., Svensk, G., 1989. Static and dynamic properties of nonionic amphiphile micelles: Triton X-100 in aqueous solution. J. Phys. Chem. 93, 2512–2519.

Brun, P.-T., Nagel, M., Gallaire, F., 2013. Generic path for droplet relaxation in microfluidic channels. Phys. Rev. E 88, 043009.

Brunet, P., Eggers, J., Deegan, R.D., 2009. Motion of a drop driven by substrate vibrations. Eur. Phys. J. Spec. Top. 166, 11–14

Brunet, P., Eggers, J., Deegan, R.D., 2007. Vibration-Induced Climbing of Drops. Phys. Rev. Lett. 99, 144501.

Buchegger, W., Wagner, C., Lendl, B., Kraft, M., Vellekoop, M.J., 2010. A highly uniform lamination micromixer with wedge shaped inlet channels for time resolved infrared spectroscopy. Microfluid. Nanofluidics 10, 889–897.

Carroll, B., Hidrovo, C., 2013. Experimental Investigation of Inertial Mixing in Colliding Droplets. Heat Transf. Eng. 34, 120–130.

Castillo-León, J., Svendsen, W.E. (Eds.), 2014. Lab-on-a-Chip Devices and Micro-Total Analysis Systems: A Practical Guide, 2015 edition. ed. Springer, New York.

Chandesris, B., Soupremanien, U., Dunoyer, N., 2013. Uphill motion of droplets on tilted and vertical grooved substrates induced by a wettability gradient. Colloids Surf. Physicochem. Eng. Asp. 434, 126–135.

Chapman, S., Cowling, T.G., 1939. The Mathematical Theory of Non-uniform Gases. Cambridge University Press, New York.

Chaudhury, M.K., Whitesides, G.M., 1992. How to make water run uphill. Science 256, 1539–1541.

Chiou, P.Y., Moon, H., Toshiyoshi, H., Kim, C.-J., Wu, M.C., 2003. Light actuation of liquid by optoelectrowetting. Sens. Actuators Phys. 104, 222–228.

Chiou, P.Y., Park, S.-Y., Wu, M.C., 2008. Continuous optoelectrowetting for picoliter droplet manipulation. Appl. Phys. Lett. 93, 221110.

Cho, S.K., Moon, H., Kim, C.-J., 2003. Creating, transporting, cutting, and merging liquid droplets by electrowetting-based actuation for digital microfluidic circuits. J. Microelectromechanical Syst. 12, 70–80.

Choi, K., Ng, A.H.C., Fobel, R., Wheeler, A.R., 2012. Digital Microfluidics. Annu. Rev. Anal. Chem. 5, 413–440.

Choudhury, M.D., Tarafdar, S., 2014. Fingering instability in non-Newtonian fluids during squeeze flow in a Hele-Shaw cell. Indian J. Phys. 89, 471–477.

Chuang, H.-S., Kumar, A., Wereley, S.T., 2008. Open optoelectrowetting droplet actuation. Appl. Phys. Lett. 93, 064104.

Cira, N.J., Benusiglio, A., Prakash, M., 2015. Vapour-mediated sensing and motility in two-component droplets. Nature 519, 446–450.

Cobas® Liat System. https://www.cobasliat.com/

COMSOL Multiphysics, 2015. COMSOL AB, Stockholm, Sweden.

Corti, M., Degiorgio, V., 1975. Light-scattering study on the micellar properties of a non-ionic surfactant. Opt. Commun. 14, 358–362.

Daniel, S., Chaudhury, M.K., 2002. Rectified motion of liquid drops on gradient surfaces induced by vibration. Langmuir 18, 3404–3407.

Darhuber, A.A., Davis, J.M., Troian, S.M., Reisner, W.W., 2003a. Thermocapillary actuation of liquid flow on chemically patterned surfaces. Phys. Fluids 1994-Present 15, 1295–1304.

Darhuber, A.A., Troian, S.M., 2005. Principles of Microfluidic Actuation by Modulation of Surface Stresses. Annu. Rev. Fluid Mech. 37, 425–455.

Darhuber, A.A., Valentino, J.P., Troian, S.M., 2010. Planar digital nanoliter dispensing system based on thermocapillary actuation. Lab Chip 10, 1061–1071.

Darhuber, A.A., Valentino, J.P., Troian, S.M., Wagner, S., 2003b. Thermocapillary actuation of droplets on chemically patterned surfaces by programmable microheater arrays. J. Microelectromechanical Syst. 12, 873–879.

Dhanabalan, A., van Duren, J.K.J., van Hal, P.A., van Dongen, J.L.J., Janssen, R. a. J., 2001. Synthesis and characterization of a low bandgap conjugated polymer for bulk heterojunction photovoltaic cells. Adv. Funct. Mater. 11, 255–262.

Ding, X., Li, P., Lin, S.-C.S., Stratton, Z.S., Nama, N., Guo, F., Slotcavage, D., Mao, X., Shi, J., Costanzo, F., Huang, T.J., 2013. Surface acoustic wave microfluidics. Lab Chip 13, 3626–3649.

Dos Santos, F.D., Ondarçuhu, T., 1995. Free-running droplets. Phys. Rev. Lett. 75, 2972–2975.

Dung Luong, T., Trung Nguyen, N., 2010. Surface acoustic wave driven microfluidics - a review. Micro Nanosyst. 2, 217–225.

Easteal, A.J., Woolf, L.A., 1985. Pressure and temperature dependence of tracer diffusion coefficients of methanol, ethanol, acetonitrile, and formamide in water. J. Phys. Chem. 89, 1066–1069.

Eddi, A., Winkels, K.G., Snoeijer, J.H., 2013. Influence of droplet geometry on the coalescence of low viscosity drops. Phys. Rev. Lett. 111, 144502.

Egatz-Gomez, A., Melle, S., Garcia, A.A., Lindsay, S.A., Marquez, M., Dominguez-Garcia, P., Rubio, M.A., Picraux, S.T., Taraci, J.L., Clement, T., Yang, D., Hayes, M.A., Gust, D., 2006. Discrete magnetic microfluidics. Appl. Phys. Lett. 89, 034106-034106-3.

ElSherbini, A.I., Jacobi, A.M., 2004. Liquid drops on vertical and inclined surfaces: I. An experimental study of drop geometry. J. Colloid Interface Sci. 273, 556–565.

Erickson, D., Li, D., 2004. Integrated microfluidic devices. Anal. Chim. Acta, Microfluidics and Lab - On - a - Chip 507, 11–26.

Extrand, C.W., Kumagai, Y., 1995. Liquid drops on an inclined plane: the relation between contact angles, drop shape, and retentive force. J. Colloid Interface Sci. 170, 515–521.

Faisal, T.F., Chevalier, S., Bernabe, Y., Juanes, R., Sassi, M., 2015. Quantitative and qualitative study of density driven CO_2 mass transfer in a vertical Hele-Shaw cell. Int. J. Heat Mass Transf. 81, 901–914.

Ford, M.L., Nadim, A., 1994. Thermocapillary migration of an attached drop on a solid surface. Phys. Fluids 6, 3183–3185.

Gallaire, F., Meliga, P., Laure, P., Baroud, C.N., 2014. Marangoni induced force on a drop in a Hele Shaw cell. Phys. Fluids 1994-Present 26, 062105.

Ghi, P.Y., Hill, D.J., Whittaker, A.K., 2002. PFG-NMR measurements of the self-diffusion coefficients of water in equilibrium poly (HEMA-co-THFMA) hydrogels. Biomacromolecules 3, 554–559.

Gilliland, E.R., 1934. Diffusion Coefficients in Gaseous Systems. Ind. Eng. Chem. 26, 681–685.

Gomba, J.M., Homsy, G.M., 2010. Regimes of thermocapillary migration of droplets under partial wetting conditions. J. Fluid Mech. 647, 125–142.

Gordon, A.R., 1945. The diaphragm cell method of measuring diffusion. Ann. N. Y. Acad. Sci. 46, 285–308.

Greenspan, H.P., 1978. On the motion of a small viscous droplet that wets a surface. J. Fluid Mech. 84, 125–143.

Grigoriev, R.O., Schatz, M.F., Sharma, V., 2006. Chaotic mixing in microdroplets. Lab Chip 6, 1369.

Grotberg, J.B., 1994. Pulmonary Flow and Transport Phenomena. Annu. Rev. Fluid Mech. 26, 529–571.

Guo, X.-R, Young, W.-B., 2015. A two-dimensional simulation model for the molded underfill process in flip chip packaging. J. Mech. Sci. Technol. 29, 2967–2974.

Guo, Z.-G., Zhou, F., Hao, J.-C., Liang, Y.-M., Liu, W.-M., Huck, W.T.S., 2006. "Stick and slide" ferrofluidic droplets on superhydrophobic surfaces. Appl. Phys. Lett. 89, 081911.

Gustafsson, B., Vasil'ev, A., 2006. Conformal and Potential Analysis in Hele-Shaw Cells. Springer Science & Business Media.

Guttenberg, Z., Müller, H., Habermüller, H., Geisbauer, A., Pipper, J., Felbel, J., Kielpinski, M., Scriba, J., Wixforth, A., 2005. Planar chip device for PCR and hybridization with surface acoustic wave pump. Lab Chip 5, 308–317.

Halverson, J.D., Maldarelli, C., Couzis, A., Koplik, J., 2008. A molecular dynamics study of the motion of a nanodroplet of pure liquid on a wetting gradient. J. Chem. Phys. 129, 164708.

Hammond, B.R., Stokes, R.H., 1953. Diffusion in binary liquid mixtures. Part 1.—Diffusion coefficients in the system ethanol + water at 25°. Trans. Faraday Soc. 49, 890–895.

Harris, K.R., Goscinska, T., Lam, H.N., 1993. Mutual diffusion coefficients for the systems water-ethanol and water-propan-1-ol at 25 deg C. J. Chem. Soc. Faraday Trans. 89, 1969.

Hemmilä, S., Cauich-Rodríguez, J.V., Kreutzer, J., Kallio, P., 2012. Rapid, simple, and cost-effective treatments to achieve long-term hydrophilic PDMS surfaces. Appl. Surf. Sci. 258, 9864–9875.

Hessel, V., Löwe, H., Schönfeld, F., 2005. Micromixers—a review on passive and active mixing principles. Chem. Eng. Sci., 5th International Symposium on Mixing in Industrial Processes (ISMIP5) 60, 2479–2501.

Hodges, S.R., Jensen, O.E., Rallison, J.M., 2004. The motion of a viscous drop through a cylindrical tube. J. Fluid Mech. 501, 279–301.

Holmes, D., Gawad, S., 2010. The Application of Microfluidics in Biology, in: Hughes, M.P., Hoettges, K.F. (Eds.), Microengineering in Biotechnology, Methods in Molecular Biology. Humana Press, pp. 55–80.

Holz, M., Heil, S.R., Sacco, A., 2000. Temperature-dependent self-diffusion coefficients of water and six selected molecular liquids for calibration in accurate 1H NMR PFG measurements. Phys. Chem. Chem. Phys. 2, 4740–4742.

Huebner, A., Bratton, D., Whyte, G., Yang, M., Abell, C., Hollfelder, F., others, 2009. Static microdroplet arrays: a microfluidic device for droplet trapping, incubation and release for enzymatic and cell-based assays. Lab Chip 9, 692–698.

Huerre, A., Theodoly, O., Leshansky, A.M., Valignat, M.-P., Cantat, I., Jullien, M.-C., 2015. Droplets in microchannels: dynamical properties of the lubrication film. Phys. Rev. Lett. 115, 064501.

Israelachvili, J.N., 2011. Intermolecular and Surface Forces, Third Edition: Revised Third Edition, 3 edition. ed. Academic Press, San Diego, Calif.

Jain, M., Nandakumar, K., 2010. Novel index for micromixing characterization and comparative analysis. Biomicrofluidics 4, 031101.

John, K., Thiele, U., 2010. Self-Ratcheting Stokes Drops Driven by Oblique Vibrations. Phys. Rev. Lett. 104, 107801.

Jones, T.B., 2002. On the relationship of dielectrophoresis and electrowetting. Langmuir 18, 4437–4443.

Kang, K.H., 2002. How electrostatic fields change contact angle in electrowetting. Langmuir 18, 10318–10322.

Karpitschka, S., Pandey, A., Lubbers, L.A., Weijs, J.H., Botto, L., Das, S., Andreotti, B., Snoeijer, J.H., 2016. Liquid drops attract or repel by the inverted Cheerios effect. Proc. Natl. Acad. Sci. 113, 7403–7407.

Karpitschka, S., Riegler, H., 2014. Sharp transition between coalescence and non-coalescence of sessile drops. J. Fluid Mech. 743.

Kim, S.H., Moon, J.-H., Kim, J.H., Jeong, S.M., Lee, S.-H., 2011. Flexible, stretchable and implantable PDMS encapsulated cable for implantable medical device. Biomed. Eng. Lett. 1, 199–203.

Krasnopolskaya, T.S., Meleshko, V.V., Peters, G.W.M., Meijer, H.E.H., 1999. Mixing in Stokes flow in an annular wedge cavity. Eur. J. Mech. - B Fluids 18, 793–822.

Krogmann, F., Qu, H., Mönch, W., Zappe, H., 2008. Push/pull actuation using opto-electrowetting. Sens. Actuators Phys. 141, 499–505.

Kwon, K.C., Park, Y., Simmons, C.M., Tibere, G.L., Ibrahim, T.H., 2003. Molecular diffusion of volatile-liquid vapors into air. Chem. Eng. Commun. 190, 1449–1467.

Lai, Y.-H., Hsu, M.-H., Yang, J.-T., 2010. Enhanced mixing of droplets during coalescence on a surface with a wettability gradient. Lab Chip 10, 3149–3156.

Lee, C.-Y., Chang, C.-L., Wang, Y.-N., Fu, L.-M., 2011. Microfluidic Mixing: A Review. Int. J. Mol. Sci. 12, 3263–3287.

Lee, C.Y., Wilke, C.R., 1954. Measurements of Vapor Diffusion Coefficient. Ind. Eng. Chem. 46, 2381–2387.

Lee, J.S., Fung, Y.C., 1969. Stokes flow around a circular cylindrical post confined between two parallel plates. J. Fluid Mech. 37, 657–670.

Lee, Y.E., Li, S.F.Y., 1991. Binary diffusion coefficients of the methanol/water system in the temperature range 30-40 degree C. J. Chem. Eng. Data 36, 240–243.

Lewis, D.J., 1950. The instability of liquid surfaces when accelerated in a direction perpendicular to their planes. ii. Proc. R. Soc. Lond. Math. Phys. Eng. Sci. 202, 81–96.

Li, Y.-H., Peng, T.-H., Broecker, W.S., Östlund, H.G., 1984. The average vertical mixing coefficient for the oceanic thermocline. Tellus B 36B, 212–217.

Liu, Z., Huang, Y., Jin, Y., Cheng, Y., 2010. Mixing intensification by chaotic advection inside droplets for controlled nanoparticle preparation. Microfluid. Nanofluidics 9, 773–786.

Lu, H.-W., Glasner, K., Bertozzi, A.L., Kim, C.-J., 2007. A diffuse-interface model for electrowetting drops in a Hele-Shaw cell. J. Fluid Mech. 590, 411–435.

Lugg, G.A., 1968. Diffusion coefficients of some organic and other vapors in air. Anal. Chem. 40, 1072–1077.

Manz, A., Graber, N., Widmer, H.M., 1990. Miniaturized total chemical analysis systems: A novel concept for chemical sensing. Sens. Actuators B Chem. 1, 244–248.

Mao, W., Oron, A., Alexeev, A., 2013. Fluid transport in thin liquid films using traveling thermal waves. Phys. Fluids 25, 072101.

Martinez, A.W., Phillips, S.T., Whitesides, G.M., Carrilho, E., 2010. Diagnostics for the Developing World: Microfluidic Paper-Based Analytical Devices. Anal. Chem. 82, 3–10.

Matar, O.K., Craster, R.V., 2001. Models for Marangoni drying. Phys. Fluids 1994-Present 13, 1869–1883.

Matthews, M.A., Akgerman, A., 1987. Diffusion coefficients for binary alkane mixtures to 573 K and 3.5 MPa. AIChE J. 33, 881–885.

Maxwell, J.C., 1868. On the Dynamical Theory of Gases. Phiosophical Transacations R. Soc. Lond. 35.

McLean, J.W., Saffman, P.G., 1981. The effect of surface tension on the shape of fingers in a Hele-Shaw cell. J. Fluid Mech. 102, 455–469.

McMurtrie, R.L., Keyes, F.G., 1948. A Measurement of the Diffusion Coefficient of Hydrogen Peroxide Vapor into Air. J. Am. Chem. Soc. 70, 3755–3758.

Mengeaud, V., Josserand, J., Girault, H.H., 2002. Mixing Processes in a Zigzag Microchannel: Finite Element Simulations and Optical Study. Anal. Chem. 74, 4279–4286.

Moon, H., Cho, S.K., Garrell, R.L., Kim, C.-J. "CJ," 2002. Low voltage electrowetting-on-dielectric. J. Appl. Phys. 92, 4080–4087.

Muradoglu, M., Stone, H.A., 2005. Mixing in a drop moving through a serpentine channel: A computational study. Phys. Fluids 17, 073305.

Nečas, D., Klapetek, P., 2012. Gwyddion: an open-source software for SPM data analysis. Open Phys. 10, 181–188.

Neerincx, P.E., Denteneer, R.P., Peelen, S., Meijer, H.E., 2011. Compact mixing using multiple splitting, stretching, and recombining flows. Macromol. Mater. Eng. 296, 349–361.

Ng, V.-V., Sellier, M., Nock, V., 2016. Marangoni-induced actuation of miscible liquid droplets on an incline. Int. J. Multiph. Flow 82, 27–34.

Nock, V., Muller, Y., Sellier, M., Verdier, C., 2013. Biochemical sensing assays based on coalescence-induced self-propulsion digital microfluidics, in: 2013 Seventh International Conference on Sensing Technology (ICST). Presented at the 2013 Seventh International Conference on Sensing Technology (ICST), pp. 67–70.

O'Connell, J.P., Gillespie, M.D., Krostek, W.D., Prausnitz, J.M., 1969. Diffusivities of water in nonpolar gases. J. Phys. Chem. 73, 2000–2004.

Ondarcuhu, T., Veyssie, M., 1991. Dynamics of spreading of a liquid drop across a surface chemical discontinuity. J. Phys. II 1, 75–85.

Oswald, P., Poy, G., 2015. Droplet relaxation in Hele-Shaw geometry: Application to the measurement of the nematic-isotropic surface tension. Phys. Rev. E 92, 062512.

Ottino, J.M., 1989. The Mixing of Fluids. Sci. Am. 56–67.

Paik, P., Pamula, V.K., Pollack, M.G., Fair, R.B., 2003. Electrowetting-based droplet mixers for microfluidic systems. Lab Chip 3, 28–33.

Paradies, H.H., 1980. Shape and size of a nonionic surfactant micelle. Triton X-100 in aqueous solution. J. Phys. Chem. 84, 599–607.

Park, J.-H., Derfus, A.M., Segal, E., Vecchio, K.S., Bhatia, S.N., Sailor, M.J., 2006. Local heating of discrete droplets using magnetic porous silicon-based photonic crystals. J. Am. Chem. Soc. 128, 7938–7946.

Park, S.-Y., A. Teitell, M., Y. Chiou, E.P., 2010. Single-sided continuous optoelectrowetting (SCOEW) for droplet manipulation with light patterns. Lab Chip 10, 1655–1661.

Paterson, L., 1981. Radial fingering in a Hele Shaw cell. J. Fluid Mech. 113, 513–529.

Pei, S.N., Valley, J.K., Neale, S.L., Jamshidi, A., Hsu, H.-Y., Wu, M.C., 2010. Light-actuated digital microfluidics for large-scale, parallel manipulation of arbitrarily sized droplets, in: 2010 IEEE 23rd International Conference on Micro Electro Mechanical Systems (MEMS). Presented at the 2010 IEEE 23rd International Conference on Micro Electro Mechanical Systems (MEMS), pp. 252–255.

Petersen, K.E., 1979. Fabrication of an integrated, planar silicon ink-jet structure. IEEE Trans. Electron Devices 26, 1918–1920.

Piruska, A., Nikcevic, I., Lee, S.H., Ahn, C., Heineman, W.R., Limbach, P.A., Seliskar, C.J., 2005. The autofluorescence of plastic materials and chips measured under laser irradiation. Lab Chip 5, 1348–1354.

Plouffe, B.D., Njoka, D.N., Harris, J., Liao, J., Horick, N.K., Radisic, M., Murthy, S.K., 2007. Peptide-mediated selective adhesion of smooth muscle and endothelial cells in microfluidic shear flow. Langmuir 23, 5050–5055.

Pollack, M.G., Fair, R.B., Shenderov, A.D., 2000. Electrowetting-based actuation of liquid droplets for microfluidic applications. Appl. Phys. Lett. 77, 1725–1726.

Pradhan, T.K., Panigrahi, P.K., 2016. Influence of an adjacent droplet on fluid convection inside an evaporating droplet of binary mixture. Colloids Surf. Physicochem. Eng. Asp. 500, 154–165.

Pratt, K.C., Wakeham, W.A., 1974. The mutual diffusion coefficient of ethanol-water mixtures: determination by a rapid, new method, in: Proceedings of the Royal Society of London A: Mathematical, Physical and Engineering Sciences. The Royal Society, pp. 393–406.

Rasband, W.S., 1997. Image J. U Natl. Inst. Health Bethesda Md. USA. http://www.imagej.nih.gov/ij/

Savina, T.V., Nepomnyashchy, A.A., 2015. On a Hele-Shaw flow with a time-dependent gap in the presence of surface tension. J. Phys. Math. Theor. 48, 125501.

Seemann, R., Brinkmann, M., Kramer, E.J., Lange, F.F., Lipowsky, R., 2005. Wetting morphologies at microstructured surfaces. Proc. Natl. Acad. Sci. U. S. A. 102, 1848–1852.

Sellier, M., Nock, V., Gaubert, C., Verdier, C., 2013. Droplet actuation induced by coalescence: Experimental evidences and phenomenological modeling. Eur. Phys. J. Spec. Top. 219, 131–141.

Sellier, M., Nock, V., Verdier, C., 2011. Self-propelling, coalescing droplets. Int. J. Multiph. Flow 37, 462–468.

Sellier, M., Trelluyer, E., 2009. Modeling the coalescence of sessile droplets. Biomicrofluidics 3, 022412.

Sellier, M., Verdier, C., Nock, V., 2017. The spontaneous motion of a slug of miscible liquids in a capillary tube. Int. J. Nanotechnol. 14, 530.

Shad, S., Gates, I.D., Maini, B.B., 2009. Investigation and visualization of liquid–liquid flow in a vertically mounted Hele-Shaw cell: flow regimes, velocity and shape of droplets. Meas. Sci. Technol. 20, 114005.

Shen, B., Leman, M., Reyssat, M., Tabeling, P., 2014. Dynamics of a small number of droplets in microfluidic Hele–Shaw cells. Exp. Fluids 55, 1–10.

Slattery, J.C., Bird, R.B., 1958. Calculation of the diffusion coefficient of dilute gases and of the self-diffusion coefficient of dense gases. AIChE J. 4, 137–142.

Smith, M.K., 1995. Thermocapillary migration of a two-dimensional liquid droplet on a solid surface. J. Fluid Mech. 294, 209–230.

Snijder, E.D., te Riele, M.J.M., Versteeg, G.F., van Swaaij, W.P.M., 1993. Diffusion coefficients of several aqueous alkanolamine solutions. J. Chem. Eng. Data 38, 475–480.

Song, H., Ismagilov, R.F., 2003. Millisecond kinetics on a microfluidic chip using nanoliters of reagents. J. Am. Chem. Soc. 125, 14613–14619.

Stefan, J., 1890. Ueber die Verdampfung und die Auflösung als Vorgänge der Diffusion. Ann. Phys. 277, 725–747.

Stone, H.A., Stroock, A.D., Ajdari, A., 2004. Engineering Flows in Small Devices. Annu. Rev. Fluid Mech. 36, 381–411.

Streletzky, K., Phillies, G.D.J., 1995. Temperature Dependence of Triton X-100 Micelle Size and Hydration. Langmuir 11, 42–47.

Stroock, A.D., Dertinger, S.K.W., Ajdari, A., Mezić, I., Stone, H.A., Whitesides, G.M., 2002. Chaotic Mixer for Microchannels. Science 295, 647–651.

Subramanian, R.S., Moumen, N., McLaughlin, J.B., 2005. Motion of a drop on a solid surface due to a wettability gradient. Langmuir 21, 11844–11849.

Sullivan, M.T., Wilkins, D., Finley, E.S., Ward, T., 2014. Gravity and capillary pressure-driven drainage in a vertical Hele-Shaw cell: Thin film deposition. Chem. Eng. Sci. 109, 147–157.

Sultan, E., Boudaoud, A., Amar, M.B., 2005. Evaporation of a thin film: diffusion of the vapour and Marangoni instabilities. J. Fluid Mech. 543, 183–202.

Tan, M.K., Friend, J.R., Yeo, L.Y., 2007. Microparticle collection and concentration via a miniature surface acoustic wave device. Lab Chip 7, 618–625.

Tanthapanichakoon, W., Aoki, N., Matsuyama, K., Mae, K., 2006. Design of mixing in microfluidic liquid slugs based on a new dimensionless number for precise reaction and mixing operations. Chem. Eng. Sci. 61, 4220–4232.

Taylor, G., 1953. Dispersion of Soluble Matter in Solvent Flowing Slowly through a Tube. Proc. R. Soc. Lond. Math. Phys. Eng. Sci. 219, 186–203.

Terry, S.C., Jerman, J.H., Angell, J.B., 1979. A gas chromatographic air analyzer fabricated on a silicon wafer. IEEE Trans. Electron Devices 26, 1880–1886.

Thallhammer, S., Wixforth, A., 2013. Surface acoustic wave actuated lab-on-chip system for single cell analysis. J. Biosens. Bioelectron. 4, 134.

Thiele, U., John, K., 2010. Transport of free surface liquid films and drops by external ratchets and self-ratcheting mechanisms. Chem. Phys., Stochastic processes in Physics and Chemistry (in honor of Peter Hänggi) 375, 578–586.

Tofteberg, T., Skolimowski, M., Andreassen, E., Geschke, O., 2009. A novel passive micromixer: lamination in a planar channel system. Microfluid. Nanofluidics 8, 209–215.

Tominaga, T., Matsumoto, S., 1990. Limiting interdiffusion coefficients of some hydroxylic compounds in water from 265 to 433 K. J. Chem. Eng. Data 35, 45–47.

Usami, S., Chen, H.-H., Zhao, Y., Chien, S., Skalak, R., 1993. Design and construction of a linear shear stress flow chamber. Ann. Biomed. Eng. 21, 77–83.

Vazquez, G., Alvarez, E., Navaza, J.M., 1995. Surface Tension of Alcohol Water + Water from 20 to 50 degree C. J. Chem. Eng. Data 40, 611–614.

Vorobyev, A.Y., Guo, C., 2010. Water sprints uphill on glass. J. Appl. Phys. 108, 123512.

Wei, H.H., Waters, S.L., Liu, S.Q., Grotberg, J.B., 2003. Flow in a wavy-walled channel lined with a poroelastic layer. J. Fluid Mech. 492, 23–45.

Werts, M.H.V., Raimbault, V., Texier-Picard, R., Poizat, R., Français, O., Griscom, L., Navarro, J.R.G., 2012. Quantitative full-colour transmitted light microscopy and dyes for concentration mapping and measurement of diffusion coefficients in microfluidic architectures. Lab Chip 12, 808.

Wiggins, S., Ottino, J.M., 2004. Foundations of chaotic mixing. Philos. Trans. R. Soc. Lond. Math. Phys. Eng. Sci. 362, 937–970.

Wu, Y., Saito, N., Nae, F.A., Inoue, Y., Takai, O., 2006. Water droplets interaction with super-hydrophobic surfaces. Surf. Sci., Berlin, Germany: 4–9 September 2005 Proceedings of the 23th European Conference on Surface Science 600, 3710–3714.

Xia, H.M., Wan, S.Y.M., Shu, C., Chew, Y.T., 2005. Chaotic micromixers using two-layer crossing channels to exhibit fast mixing at low Reynolds numbers. Lab Chip 5, 748–755.

Yao, X., Bai, H., Ju, J., Zhou, D., Li, J., Zhang, H., Yang, B., Jiang, L., 2012. Running droplet of interfacial chemical reaction flow. Soft Matter 8, 5988–5991.

Yarin, A.L., Liu, W., Reneker, D.H., 2002. Motion of droplets along thin fibers with temperature gradient. J. Appl. Phys. 91, 4751–4760.

Yeh, S.-I., Sheen, H.-J., Yang, J.-T., 2014. Chemical reaction and mixing inside a coalesced droplet after a head-on collision. Microfluid. Nanofluidics 18, 1355–1363.

Yeo, L.Y., Chang, H.-C., 2005. Static and spontaneous electrowetting. Mod. Phys. Lett. B 19, 549–569.

Yeo, L.Y., Friend, J.R., 2014. Surface Acoustic Wave Microfluidics. Annu. Rev. Fluid Mech. 46, 379–406.

Yi, U.-C., Kim, C.-J., 2006. Characterization of electrowetting actuation on addressable single-side coplanar electrodes. J. Micromechanics Microengineering 16, 2053.

Yobas, L., Cheow, L.F., Tang, K.-C., Yong, S.-E., Ong, E.K.-Z., Wong, L., Teo, W.C.-Y., Ji, H., Rafeah, S., Yu, C., 2009. A self-contained fully-enclosed microfluidic cartridge for lab on a chip. Biomed. Microdevices 11, 1279–1288.

Yoon, J.-Y., 2008. Open-surface digital microfluidics. Open Biotechnol. J. 2, 94–100.

Zeiger, A.S., Hinton, B., Van Vliet, K.J., 2013. Why the dish makes a difference: Quantitative comparison of polystyrene culture surfaces. Acta Biomater. 9, 7354–7361.

Zeng, X., Zhang, K., Pan, J., Chen, G., Liu, A.-Q., Fan, S.-K., Zhou, J., 2013. Chemiluminescence detector based on a single planar transparent digital microfluidic device. Lab Chip 13, 2714–2720.

Zeng, Y., Weinbaum, S., 1994. Stokes flow through periodic orifices in a channel. J. Fluid Mech. 263, 207–226.

Zhang, J., Han, Y., 2007. Shape-gradient composite surfaces: water droplets move uphill. Langmuir 23, 6136–6141.

Zouache, M.A., Eames, I., Luthert, P.J., 2015. Blood flow in the choriocapillaris. J. Fluid Mech. 774, 37–66.